Development of tunable optical filter for photonic application

Li, Songyang

2005

Li, S. (2005). Development of tunable optical filter for photonic application. Doctoral thesis, Nanyang Technological University, Singapore.

https://hdl.handle.net/10356/4719

https://doi.org/10.32657/10356/4719

Development of Tunable Optical Filters for Photonic Applications

Li Songyang

SCHOOL OF ELECTRICAL & ELECTRONIC ENGINEERING

A thesis submitted to the Nanyang Technological University
in fulfillment of the requirement for the degree of
Doctor of Philosophy

2005

Statement of Originality

I hereby certify that the work embodied in this thesis is the result of original research and has not been submitted for a higher degree to any other University or Institution.

9th Nov 2005
Date

Li Songyang
Li Songyang

Acknowledgement

This thesis is built on the shoulders of more people than I could ever name in this space, for I feel as I should thank all the people who have had a hand in shaping my intellectual and personal growth to the point. However, I would be remiss if I did not single out a few people for special thanks.

I would like to express my deepest gratitude to my supervisor and first reader, Asst/Prof. Ngo Quoc Nam (John), for his guidance and encouragement throughout the whole period of my PhD study. I always feel inspired by his boundless enthusiasm, dedication to excellence, and careful attention to details. I feel very proud to be given this opportunity to study under him. I would also like to thanks Assoc/Prof. Tjin Swee Chuan and Assoc/Prof. Shum Ping for valuable discussion and strong support on my PhD study. I would also like to express my gratitude to Prof. Le Nguyen Binh of Monash University, Australia, for his encouragement and fruitful discussion.

I want to express my sincere thanks to Dr. Seriampalayam Ramaswamy Natarajan for his guidance and encouragement to the initial stage of my study. I wish to thank Dr. Zhou Kejiang for his assistance in the fiber ring laser development. I am gratefule to Dr. Liu Yunqi, Dr. Yang Jiangliang, Dr. Dong Xinyong, Mr. Zheng Ruitao, and Ms Zhang Jing for useful discussions and cooperation in the experiment. I would also like to thank Mr. Huang Jixing for assistance in the simulation of the phase-shifted FBG. I am also grateful of the assistance of Mr. Ang Hwee Khai and Mr. Ong Chen Wui in the all-fiber

acousto-optic tunable filter experiment. My thanks go to all staffs and students in Photonics Research Center and Network Technology Research Center for providing a very friendly and entertaining working environment.

On a personal level, I am forever indebted to my parents, Mr. Li Zhenhua and Mrs. Su Ciying, for their continual understanding and encouragement throughout all my years of study. I am grateful for the support of my brothers, Dr. Li Haizheng and Dr. Li Jiangyu. Very special thanks must go to my girlfriend, Yu Jun. Her support and assistance helps me go through any hard time.

Summary

A tunable optical filter (TOF), which can dynamically select a particular optical signal wavelength, is an important device in such applications as optical communication systems, optical sensing systems, and tunable laser systems. In wavelength division multiplexing (WDM) systems, one requirement is the selection of the wavelength channel that must be carried out in the wavelength domain. Thus, the TOF is highly desirable in such systems. The next generation of reconfigurable optical networks raises the request for TOFs with large tuning range, simple tuning mechanism, low insertion loss, narrow bandwidth, high rejection ratio, high tuning speed and cost effectiveness.

This thesis documents the investigation of several type of novel TOFs based on different technologies, which include all-fiber acousto-optical technique, fiber Bragg gratings (FBGs), and phase-shifted FBGs. Several tuning methods and mechanisms of TOFs are proposed. To demonstrate the effectiveness of the proposed tuning methods, several types of TOFs for various applications have been developed and tested, which include an electrically tunable dispersion compensating filter, a widely tunable narrow bandpass filter, a widely tunable broad bandpass filter, an optical bandpass filter with adjustable bandwidth, and an all-fiber acousto-optical tunable filter. Furthermore, the unique application of the newly developed tunable narrow bandpass filter in an erbium-doped fiber ring laser has also been studied.

Table of Contents

List of Abbreviations

AO	Acousto-optic
AOTF	acousto-optical tunable filter
AWG	array waveguide grating
CFBG	Chirped fiber Bragg grating
DBF	distributed feedback
DWDM	dense wavelength-division multiplexing
EDF	erbium-doped fiber
EDFA	erbium-doped fiber amplifier
EDFL	Erbium-doped fiber laser
EDFRL	erbium-doped fiber ring laser
EOTF	electrooptical tunable filter
FBG	fiber Bragg grating
F-P	Fabry-Perot
FSK	frequency-shift keying
FSR	free spectral range
FWHM	full width half-maximum
HF	hydrofluoric
LCFBG	linearly chirped fiber Bragg grating
LD	laser diode
M-Z	Mach-Zehnder
NRZ	non-return-to-zero
NTEC	negative thermal expansion coefficient ceramic
OBF	optical bandpass filter
OSA	optical spectrum analyzer
PC	polarization controller
PS-LCFBG	phase-shifted linearly chirped fiber Bragg grating
PZT	piezo-electric transducer
RIN	relative intensity noise
RF	radio frequency
SAW	surface acoustic wave
SMF	single-mode fiber
SPM	self-phase modulation
TLS	tunable laser source
TOF	tunable optical bandpass filer
TOF	tunable optical filter
UV	ultraviolet
WDM	wavelength-division multiplexing
WDR	wavelength-dependent reflector
XPM	cross-phase modulation

List of Figures

List of Tables

1 Introduction

1.1 Background

Since the development of low-loss optical fibers in the 1970 s, optical fibers are gradually becoming a dominant communication medium nowadays. The rapid development of fiber optical communications benefits from the unbeatable advantages of optical fiber, such as (i), light weight and small size, the weight and size of silica fiber is much smaller than the electrical cable to operate the same function; (ii), low material cost, the copper cable cost much more than the silica fiber for the same transmission capacity; (iii), large information capacity, the information capacity of silica fiber is thousands of times of that of coaxial cable; (iv), long distance between regenerators, the repeater spacing is typically 40 km in the current long-line optical transmission cables, which is much longer than the 12 km repeater spacing of traditional coaxial cable technology; (v), better security, the transmitted information is well confined in the fiber core, and to tap the information from the fiber is very difficult.

The emergence of wavelength-division multiplexing (WDM) offers a further boost into optical fiber transmission capacity. The basic idea of WDM is to transmit several independent information streams over the same optical fiber by modulating each information stream into a particular lightwave with a number of discrete individual optical wavelengths [1]. The application of WDM can upgrade the transmission capacity of existing point-to-point fiber link. In the WDM systems, using different wavelengths, information with different formats (for example, asynchronous and synchronous, or digital and analog) can be transmitted in the same fiber link simultaneously and independently. Using the wavelength-sensitive optical routing or switching devices, the wavelength-routed networks can be developed, which can increase the flexibility of networks.

To implement the WDM networks, a variety of devices are necessary to combine, distribute, and isolate the optical signal power at different wavelengths. As a result, the research and development of tunable optical devices, which include tunable bandpass filters, tunable dispersion compensation filters, dynamic gain equalization filters and tunable lasers, are increasingly important to meet the demand of the next generation of dynamic networks.

1.2 Motivation

A tunable optical filter (TOF), which can be used to dynamically select a particular optical wavelength, is an important device in optical communication

systems, optical sensing systems, and tunable laser systems. In WDM systems, the functionalities such as channel selection should be carried out in the wavelength domain. And hence, a TOF is highly desirable in such systems. The next generation of reconfigurable optical networks raises the request for TOFs with large tuning range, simple tuning mechanism, low insertion loss, narrow bandwidth, high rejection ratio, high tuning speed and cost effectiveness [2]. In optical sensing systems, a TOF is required in the development of an interrogator. Due to the wavelength-encoded nature of fiber Bragg gratings (FBGs), arrays of FBG sensors, each of which operates at a different wavelength, can be interrogated with a single TOF and a broadband optical source [3]. In the tunable laser systems, a TOF can be used to select the resonance wavelength in the cavity to extract the output lasing wavelength [4].

The optical structures used for filtering applications are typically based on the interference phenomena, which include two beams interference as in Mach-Zehnder (M-Z) interferometers [5], a multiple number of beams as in Fabry-Perot (F-P) interferometers [6], and diffracted beams as in the grating structure [7]. However, most of these structures are based on plane waveguides, which need to be carefully aligned with optical fiber for use in optical fiber networks. As a result, these filtering structures based on plane waveguides suffer from the disadvantages of large insertion loss and tricky alignment process. The accumulated insertion loss will greatly impair the performance of networks, and the complex and tricky alignment process in the fabrication will largely increase the cost of the device. Hence, the traditional tunable M-Z

interferometers and tunable F-P interferometers cannot satisfy the requirement of low insertion loss, narrow bandwidth, and cost effectiveness.

Optical filters can also fulfill some more important functions other than filtering of signal wavelengths. These functions of optical filters include chromatic dispersion compensation, dispersion slope compensation and gain equalization. Overcoming the dispersion of the fiber link is a main challenge in the high-speed long-haul optical systems. The TOFs, which can be used to compensate for the dispersion of a long fiber link, is also highly desirable in the reconfigurable optical networks.

1.3 Objectives

The main objective of this thesis is to investigate new techniques for the development of TOFs for optical communication applications. To minimize the insertion loss of the TOFs and eliminate the fiber alignment process, this thesis will focus on all-fiber devices, such as FBGs [8], long period gratings (LPGs) [9], and all-fiber acousto-optical tunable filters (AOTFs) [10]. The other advantages offered by all-fiber devices include compact size, low cost, low polarization sensitivity.

Novel techniques for tuning the transmission wavelength or dispersion of the fiber gratings will be investigated in this thesis. To evaluate the performance of the developed TOFs, the TOFs will be used in real application

environments, such as in a tunable fiber ring laser. The development and application of all-fiber AOTF will also be studied in this thesis.

1.4 Original Contributions

The original contributions of this thesis are as follows:

- Theoretical design and experimental development of a tunable dispersion compensating filter based on FBG with almost-fixed center wavelength. See chapter 3.
- Analysis and demonstration of an all-fiber acousto-optical tunable filter (AOTF). See chapter 4.
- Design and development of a tunable and switchable narrow optical bandpass filter (OBF) using a linearly chirped FBG for application in a tunable laser. See chapter 5.
- Design and development of a tunable and switchable broad OBF based on a linearly chirped FBG for WDM applications. See chapter 5.
- Design and development of a tunable and switchable OBF with adjustable bandwidth. See chapter 5.
- Design and development of a tunable fiber ring laser. The developed narrow bandpass tunable filter (as presented in Chapter 5) is used in the laser application, and the performances of the filter and laser are analyzed. See chapter 6.

1.5 Thesis Outline

Chapter 2 includes a description of the basic principles and theories of TOFs and FBGs. The existing techniques used to build TOFs are reviewed. The advantages and disadvantages of each method are discussed. The history of FBGs is briefly discussed. The basic principles of FBG are discussed. The theories used to analysis FBG are introduced and the applications of FBG in optical communication and sensing systems are briefly discussed.

A novel tunable dispersion compensating filter based on FBG is proposed and demonstrated as presented in Chapter 3. The design principles and the fabrication processes are described. The developed tunable dispersion compensating filter is evaluated with numerical simulations. The phase-shift method to measure the chromatic dispersion of the filter is described.

Chapter 4 presents the principle and development of an all-fiber AOTF. The basic theories of all-fiber AOTF are described. The design and fabrication details of the AOTF are given. The characteristics of the AOTF are analyzed and discussed.

In Chapter 5, several types of tunable and switchable OBFs are presented, which include a narrow tunable OBF, a broad tunable OBF and a tunable OBF with adjustable bandwidth. The design principles are given and the performances of the developed tunable OBFs are evaluated by comparing experimental results with the numerical simulation results.

Chapter 6 presents a tunable fiber ring laser using the developed narrow tunable OBF as described in Chapter 5. The effect of the performance of the tunable OBF on the fiber ring laser is analyzed. The delayed self-heterodyne method used to measure the narrow lasing linewidth is described.

Chapter 7, as a final chapter, gives a summary of the main contributions and conclusions of this thesis. Recommendations for future works are also included in this chapter. An appendix containing the author's publications is included at the end.

1.6 References

[1] Gerd Keiser, *Optical Fiber Communications* (*Third edition*), McGraw-Hill International Editions, 2002.

[2] D. Sadot and E. Boimovich, "Tunable optical filter for dense WDM networks," *IEEE Comm. Magaz.*, vol. 36, pp. 50–55, 1998.

[3] M. G. Xu, H. Geiger and J. P. Dakin, "Interrogation of fibre-optic interferometric sensors using acousto-optic tunable filter," *Electron. Lett.*, vol. 31, pp. 1487–1488, 1995.

[4] S. H. Yun, D. J. Richardson, D. O. Culverhouse and B. Y. Kim, "Wavelength-swept fiber laser with frequency shifted feedback and resonantly swept intra-cavity acoustooptic tunable filter," *IEEE J. Selected Topics in Quantum Electron.*, vol. 3, pp. 1087–1096, 1997.

[5] L. Wooten *et al.*, "Rapidly tunable narrowband wavelength filter using $LiNbO_3$ unbalanced Mach-Zehnder interferometers," *IEEE J. Lightwave Technol.*, vol. 6, pp. 1011–1015, 1988.

[6] J. Stone and L. W. Stulz, "Pigtailed high finesse tunable FP interferometer with large, medium, and small FSR," *Electron. Lett.*, vol. 23, pp. 781–783, 1987.

[7] R. Jambunathan and J. Singh, "Design studies for distributed Bragg reflectors for short cavity edge emitting lasers," *IEEE J. Quantum Electron.*, vol. 33, pp. 1180–1189, 1997.

[8] G. Meltz, W. Morey and W. H. Glenn, "Formation of Bragg gratings in optical fibers by a transverse holographic method," *Opt. Lett.*, vol. 14, pp. 823–825, 1989.

[9] J. Zhang, P. Shum, S. Y. Li, N. Q. Ngo, X. P. Cheng and J. H. Ng, "Design and fabrication of flat-band long-period grating," *IEEE Photon. Technol. Lett.*, vol. 15, pp. 1558–1560, 2003.

[10] H. S. Kim, S. H. Yun, I. K. Kwang and B. Y. Kim, "All-fiber Acousto-Optic Tunable Notch Filter With Electronically Controllable Spectral Profile," *Opt. Lett.*, vol. 22, pp. 1476 1478, 1997.

2 Principle of Fiber Bragg Gratings and Tunable Optical Filters

2.1 Introduction

In this chapter, the theory, characteristics, and fabrication of fiber Bragg gratings (FBGs) are presented. Existing technologies of tunable optical filters (TOFs) are briefly discussed. Tuning techniques of FBGs are also briefly discussed.

Silica fibers doped with germanium can change their optical properties permanently when they are exposed to intense radiation from a laser operating in the blue or ultraviolet spectral region. This photosensitive effect can be used to induce periodic changes in the refractive index along the fiber length, resulting in the formation of an intracore Bragg grating (see Fig. 2.1).

Fiber gratings can be designed to operate over a wide range of wavelengths from the ultraviolet to the infrared region. The wavelength region near 1.5 μm is of particular interest because of its importance to fiber-optic communications. Fiber Bragg grating (FBG) is a well-developed and

promising technology used in the development of optical filters for application in telecommunication systems. Furthermore, due to their temperature and strain sensitivities, FBGs can be used to develop tunable optical filters (TOFs) for application in the next generation of reconfigurable networks.

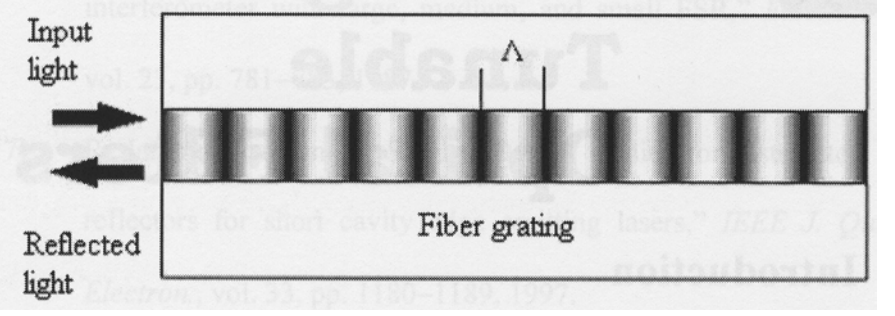

Figure 2.1 Schematic illustration of a fiber grating. Dark and light shaded regions within the fiber core correspond to periodic variations of the refractive index, Λ=grating period.

2.2 Fabrication of Fiber Bragg Gratings

Due to the photosensitivity of germanium-doped fiber, the refractive index of a fiber core changes under irradiation by ultraviolet (UV) light from a laser. Photosensitivity in optical fiber refers to a permanent change in the refractive index of the fiber core when exposed to light with characteristic wavelength and intensity that depends on the material of the fiber core. Photosensitivity was first observed in an optical fiber that was exposed to 488-nm laser light launched into its core [1]. A transverse inscription method was later used to fabricate Bragg gratings at a direct excitation wavelength of 240 nm [2]. It was then discovered that photosensitivity could be improved by up to two orders of

magnitude through hydrogenation of the optical fiber core before grating inscription [3]. The current consensus explains photosensitivity as being initiated through the formation of color centers [4] that gives way to compaction of the UV-irradiated glass [5].

FBGs can be distinguished into three types depending on the types of fibers used, on the UV radiation bands, and on the UV radiation power. FBGs formed at low UV radiation intensities are generally referred to as Type I, which is characterized by a temporary refractive index change of $\Delta n>0$ and its instability with temperature. Protracted UV exposure to Type I grating in some instances may result in complete or partial grating erasure, followed by the generation of Type IIA grating with a highly negative Δn. When the UV irradiation at energy levels greater than 1000 mJ/cm^2, the fiber core may be physically damaged [6], resulting in the generation of a Type II grating with a large refractive index change (of up to 10^{-2}). It is known that the Type II grating is the most stable grating against temperature change in these three types of FBGs.

Fiber gratings can be fabricated by using various techniques, with each having its own merits and limitations. Four commonly used techniques for fabricating fiber gratings will be briefly described in this section, which include the single-beam internal technique [1], [7], the dual-beam holographic technique [2], the phase mask technique [8], and the point-by-point fabrication technique [9].

In the single-beam internal technique, the grating formation is initiated by the light reflected from the far end of the fiber and propagating in the backward direction. The two counter-propagating waves interfere and create a standing-wave pattern with periodicity of $\lambda/(2n)$, where λ is the laser wavelength and n is the mode index at that wavelength. The refractive index of silica is modified locally the regions of high intensity, resulting in a periodic index variation along the fiber length. A disadvantage of the single-beam internal method is that the grating can be used only near the wavelength of the laser. A dual-beam holographic technique can solve this problem and is presented below.

The dual-beam holographic technique, as shown schematically in Fig. 2.2, makes use of an external interferometric scheme similar to that used for holography. Two optical beams obtained from the same laser (operating in the ultraviolet region) and making an angle of 2θ with respect to the beam axis are made to interfere at the exposed core of an optical fiber. A cylindrical lens is used to expand the beam along the fiber length. Similar to the single-beam scheme, the interference pattern creates an index grating. The most important feature of the holographic technique is that the grating period Λ can be varied over a wide range by simply adjusting the angle θ (see Fig. 2.2).

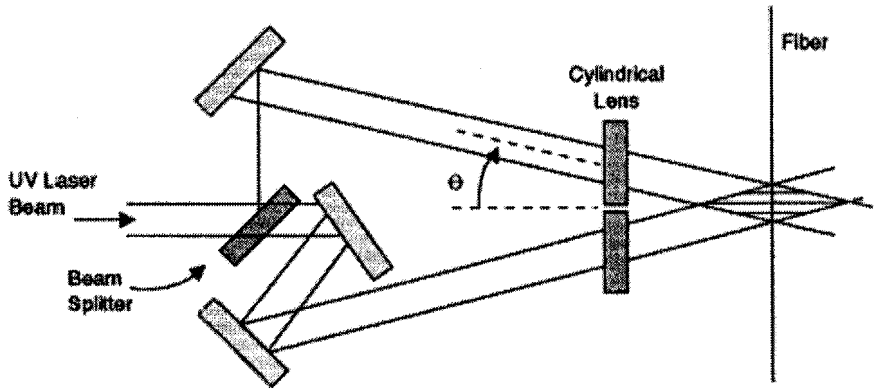

Figure 2.2 Schematic illustration of the dual-beam holographic technique.

The phase mask technique uses a photolithographic process commonly employed for fabrication of integrated electronic circuits. The basic idea is to use a phase mask with a periodicity related to the grating period. The main advantage of the phase mask method is that the demands on the temporal and spatial coherence of the ultraviolet beam are much less stringent because of the non-interferometric nature of the technique. The phase mask can also be used to form an interferometer using the setup shown in Fig. 2.3.

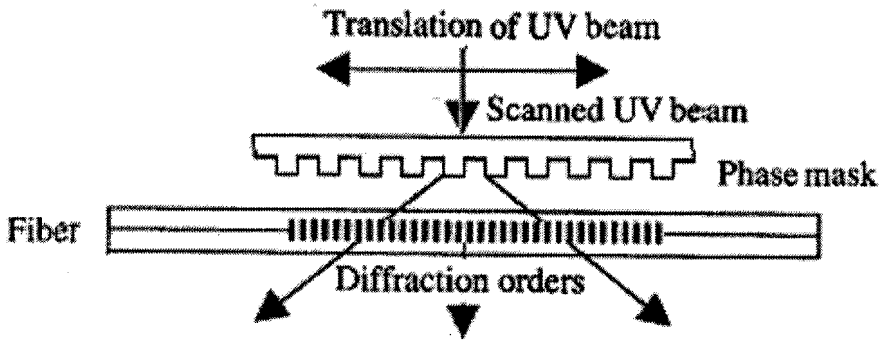

Figure 2.3 Schematic illustration of a phase mask interferometer technique used for making fiber gratings.

The UV laser beam falls normally on the phase mask and is diffracted into several beams in the Raman–Nath scattering regime. The zeroth-order beam (direct transmission) is blocked or canceled by an appropriate technique. The two first-order diffracted beams interfere on the fiber surface and form a periodic intensity pattern. The grating period is exactly one-half of the phase mask period. There are several advantages of using a phase mask interferometer technique. It is insensitive to the lateral translation of the incident laser beam and is tolerant of any beam-pointing instability. This non-holographic scanning technique bypasses the need of a master phase mask and fabricates the grating directly on the fiber, period by period, by exposing short sections of width w to the high-energy pulse. The fiber is moved by a distance, Λ, before the next pulse arrives, resulting in a periodic index pattern such that only a fraction w/Λ in each period has a higher refractive index. The method is referred to as point-by-point fabrication since a grating is fabricated period by period even though the period Λ is typically below 1 μm. The point-by-point fabrication method is also suitable for long-period gratings in which the grating period exceeds 10 μm and can even be longer than 100 μm, depending on the application.

2.3 Coupled-Mode Theory

Two different approaches have been used to study how a Bragg grating affects wave propagation in optical fibers. In one approach, Bloch formalism, which is commonly used for describing motion of electrons in semiconductors, is

applied to Bragg gratings [10]. In another method, forward- and backward-propagating waves are treated independently, and the Bragg grating provides a coupling between them. This method is known as the *coupled-mode theory* and has been used with considerable success in several different contexts [11]. In this section, the coupled-mode theory is presented and used to discuss the propagation of light through a Bragg grating.

Wave propagation in a linear periodic medium has been studied extensively using the coupled-mode theory [12]. The simplest form of coupling is between a forward-propagating mode S and an identical backward-propagating mode R along the grating position z, and these modes are expressed by the following coupled-mode equations [13]:

$$\frac{dR}{dz} + j\left[k_{dc} + \sigma - \frac{1}{2}\frac{d\phi}{dz}\right]R = -jk_{ac}^{*}S \qquad \textbf{(2.1)}$$

$$\frac{dS}{dz} - j\left[k_{dc} + \sigma - \frac{1}{2}\frac{d\phi}{dz}\right]S = jk_{ac}R \qquad \textbf{(2.2)}$$

where $j = \sqrt{-1}$, and k_{dc} and k_{ac} are the "dc" coupling constant and "ac" coupling constant respectively, which have very complicated expressions. k_{ac}^{*} is complex conjugate of k_{ac}, σ is the detuning, which indicates how rapidly the power is exchanged between the generated field and the polarization field and this weighting factor is proportional to the inverse of the distance the field travels in the generated mode. The rate of change of the phase of the grating, $d\phi/dz$, signifies a chirp in the period of the grating. For a single-mode Bragg reflection grating, k_{dc} and k_{ac} can be simply defined as

$$k_{dc} = \frac{2\pi}{\lambda}\overline{\delta n_{eff}} \tag{2.3}$$

$$k_{ac} = k_{ac}^{*} = \frac{\pi}{\lambda}\upsilon\overline{\delta n_{eff}} \tag{2.4}$$

where υ is the fringe visibility of the index change, λ is the wavelength of lightwave, and $\overline{\delta n_{eff}}$ is the peak value of the "dc" effective index of the change in refraction. If the grating is uniform along the z direction, then $\overline{\delta n_{eff}}$ is a constant. The detuning, σ, is defined as

$$\sigma = \beta - \frac{\pi}{\Lambda} \tag{2.5}$$

where β is the propagation constant and Λ is the period of the grating.

The coupled-mode equations (2.1) and (2.2) can be solved using transfer matrix method. It has been assumed that the amplitude of the incident radiation from $-\infty$ at the input of a fiber grating (of length L) at z=0 is $S(0)$=1, and that the field $R(L)$=0. These conditions result in the following analytical solution for the amplitude reflection coefficient [13]:

$$\rho = \frac{S(0)}{R(0)} = \frac{-k_{ac}\sinh(\alpha L)}{\delta\sinh(\alpha L) - j\alpha\cosh(\alpha L)} \tag{2.6}$$

where

$$\delta = k_{dc} + \sigma - \frac{1}{2}\frac{d\phi}{dz} \tag{2.7}$$

and

$$\alpha = \sqrt{|k_{ac}|^2 - \delta^2} \tag{2.8}$$

A few points regarding Eqs. (2.1)–(2.8) are worth mentioning. First, for reflection gratings that have a constant period Λ, the variation in the phase is $d\phi(z)/dz=0$. Second, for a precise phase matching (i.e. $\sigma=0$), the "ac" coupling constant k_{ac} is a real quantity. Furthermore, the power reflection coefficient $|\rho|^2$ is given by

$$|\rho|^2 = \frac{|k_{ac}|^2 \sinh^2(\alpha L)}{|k_{ac}|^2 \cosh^2(\alpha L) - \delta^2} \tag{2.9}$$

2.4 Tuning Technique of Fiber Bragg Gratings

Tunable optical components based on intracore FBGs are of great interest for application in optical fiber telecommunication and sensor networks. To select and manipulate different WDM channels, tuning of the Bragg wavelength of the FBG is necessary. The Bragg wavelength of FBG is given by

$$\lambda_B = 2n_{eff}\Lambda \tag{2.10}$$

where λ_B is the Bragg wavelength, n_{eff} is the effective index of the silica fiber, and Λ is the grating period. Hence, tuning of the Bragg wavelength can be realized by changing the grating period and/or the effective index. The change of the grating period and effective index can be achieved by applying strain to a section of the fiber or by heating a section of the fiber that contains a Bragg grating due to the photoelastic effect and the thermooptic effect of the silica fiber, respectively.

Due to the photoelastic effect of the silica fiber, the refractive index of the fiber will change with the applied external strain, and it relates to the photoelastic coefficient, p_e, which is defined as

$$p_e = \frac{n_{eff}^2}{2}\left[p_{12} - v(p_{11} + p_{12})\right] \tag{2.11}$$

where p_{11} and p_{12} are components of the photoelastic tensor, and v is the Poisson's ratio. The change in the grating spacing and the photoelastic induced change in the refractive index will result in the Bragg wavelength change, which is given by

$$\Delta\lambda_B = \lambda_B(1 - p_e)\varepsilon_z \tag{2.12}$$

where ε_z is the external strain and $\Delta\lambda_B$ is the shift in the Bragg wavelength of the FBG.

Due to the thermooptic effect of the silica fiber, the refractive index and the grating pitch will increase with temperature. The change of refractive index depends on the thermooptic coefficient, ξ, and the change of the grating pitch depends on the thermal expansion coefficient, α. The change of the grating pitch and the change of the refractive index will result in the Bragg wavelength change, $\Delta\lambda_B$, which is given by

$$\Delta\lambda_B = \lambda_B(\alpha + \xi)\Delta T \tag{2.13}$$

where ΔT is the temperature change.

The strain tuning technique is based on the sensitivity of FBGs to the applied strain. To control the strain applied on the FBG, several methods have been

proposed. The most popular method uses a piezoelectric actuator to apply and control the strain applied on the FBG (see Fig. 2.4) [14], [15]. The maximum tuning range of this method can reach 45 nm and the maximum tuning speed of 21 nm/ms has been realized. Other mechanisms to apply strain to FBGs include the Faraday effect [16], elastic beam method [17], and magnetic method [18], [19].

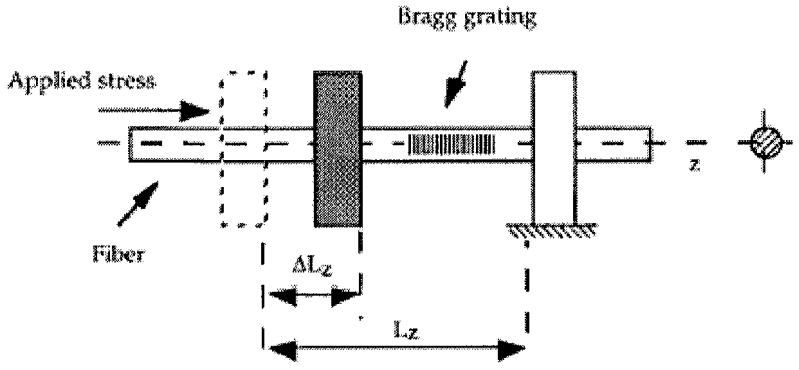

Figure 2.4 Tunable optical filter realized by FBG compression with a piezoelectric actuator [14].

Because of the sensitivity of FBG to temperature, controlling the temperature on the FBG is another method that can be used to tune the central wavelength of FBGs. Several methods have been proposed to control the temperature on the FBG. A tunable FBG has been developed using a resistive on-fiber coating to directly heat an intracore Bragg grating [20]. This device shows a tuning range of 2.15 nm with an applied electrical power of 0.54 W. demonstrated A electrically tunable FBG filter with a chemically etched cladding and an evaporated resistive layer on one side of the fiber has been demonstrated by E. R. Lyons *et al.* (see Fig. 2.5) [21]. Over an order of magnitude improvement in

the tuning efficiency has been demonstrated through a reduction of the cladding diameter and tuning under vacuum conditions. Vacuum based devices are not suitable for commercial systems due to the high cost and bulky size of using the vacuum approach.

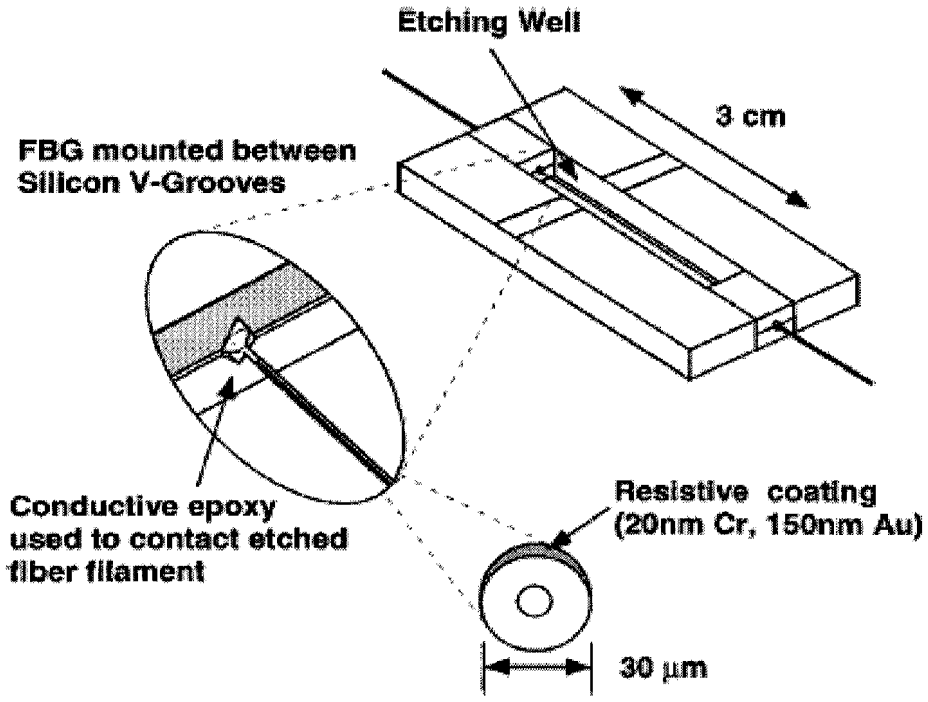

Figure 2.5 V-groove mounting fixture for thermally tunable FBG [21].

As well as the tuning techniques based on the photoelastic effect and the thermooptic effect, other techniques have also been proposed. The electrooptical effect and acousto-optical effect have been proposed to tune the Bragg wavelength of FBG. These techniques and their operating principles will be briefly reviewed as described below.

The electrooptical effect in a normal fiber is very weak, which makes the tuning very difficult and the tuning range is therefore very small. Electrooptic tuning of an FBG inscribed in a thermally-poled fiber has been demonstrated by B. Srinivasan et al. (see Fig. 2.6) [22]. A 40-pm tuning range has been demonstrated, which corresponds to an electrooptic coefficient of 0.25 pm/V.

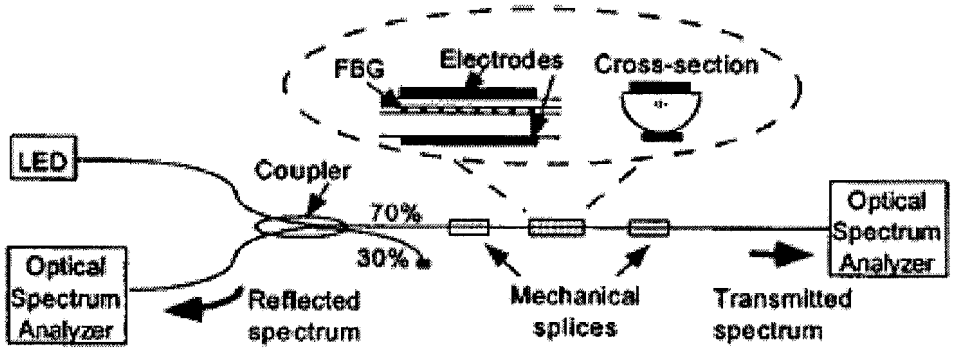

Figure 2.6 Experimental setup of a tunable FBG based on the electrooptical effect [22].

Acoustic waves may also be used to introduce a periodic internal strain in the silica fiber, which will induce a periodical refractive index change, resulting in an acoustically induced intracore grating. In the FBG, with the presence of an acoustically induced intracore grating, it will create an acousto-optic superlattice [23]. The acoustically induced reflection bands, which appear on both sides of the Bragg wavelength, can be tuned by altering the acoustic frequency (see Fig. 2.7) [24]. The bandwidth of the acoustically induced reflection bands is defined by the bandwidth of the FBG. In this technique, the reflection spectrum of FBG does not change in the tuning. However, the acoustically induced reflection band can be tuned by changing the acoustic

frequency. The short response time of the acousto-optical effect and the potentially large tuning range could make this technique very attractive.

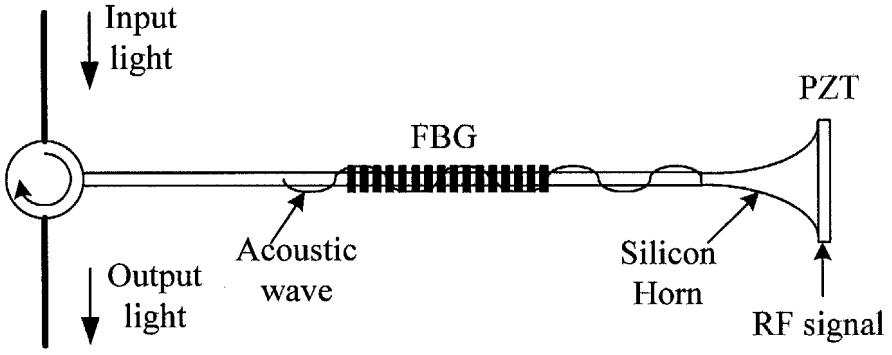

Figure 2.7 Schematic diagram of an all-fiber acousto-optic tunable filter based on the FBG. PZT is piezoelectric transducer.

2.5 Summary of Tunable Optical Filters

In the WDM systems, each WDM channel corresponds to a particular signal wavelength and thus channel manipulation and particularly channel selection will require optical wavelength selection or optical filtering. The next generation of reconfigurable optical networks will require dynamic selection and manipulation of WDM channels. Tunable optical filters (TOFs) capable of dynamically selecting the WDM channels are therefore important components in such networks.

Important parameters of TOFs include insertion loss, bandwidth, sidelobe suppression, tuning range, tuning speed, control mechanism, size, mass-

production possibility, and low cost. TOFs can be divided into two main categories depending on their applications, namely, slow-speed TOFs with tuning speed up to a few milliseconds and high-speed TOFs with tuning speed of the order of microsecond and nanosecond. Low-speed TOFs can be used in tunable lasers and fiber sensing systems, and high-speed TOFs can be used in packet- and cell-switching networks. Low-speed TOFs are mostly based on temperature or mechanical tuning methods and high-speed TOFs are normally based on the electrooptic effect or acousto-optic effect.

The TOFs based on FBG have already been briefly discussed in the previous section. Other types of TOFs will be presented in this section, which include the Fabry-Perot (F-P) interferometer tunable filter, Mach-Zehnder (M-Z) interferometer tunable filter, acousto-optic tunable filters (AOTFs), electrooptical tunable filters, tunable array waveguide grating (AWG), and tunable ring resonator.

A resonant cavity between two mirrors can form a F-P interferometer (see Fig. 2.8). The device has high transmission when the phase difference of the reflections of the lights is a multiple of 2π. The transmission of an F-P filter is a periodic Lorenzian function of frequency. The period of the transmission function is called the free spectral range (FSR). The finesse is the ratio between the FSR and the bandwidth of the filter, and is an indicator of the number of channels that can be allocated in one span of FSR. An optical_fiber F-P filter is commercially available with a resonant cavity formed by a gap

between two fiber ends, which act as two reflection mirrors [25], [26]. Its tuning is achieved by changing the length of the gap by means of heating or piezoelectric actuator.

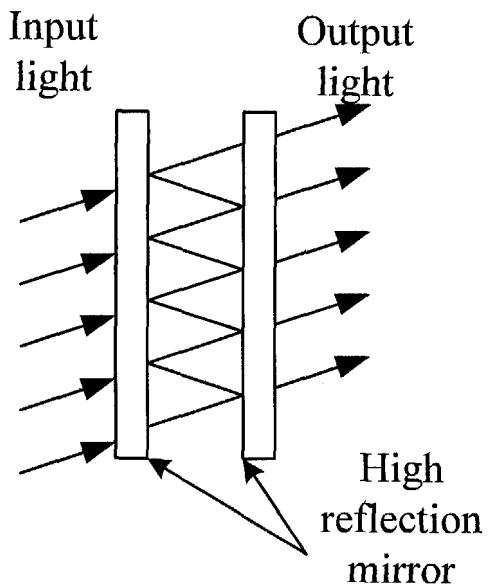

Figure 2.8 Schematic of a F-P interferometer filter.

The M-Z interferometer configuration is widely used in photonic applications. An incident beam of light is split into two paths and recombined after a short distance (see Fig. 2.9). The combining electromagnetic fields interfere according to the phase difference between the two fields. With a particular time delay difference between the two arms, the transmission is a periodic function of the optical frequency. The transfer function of the M-Z filter is usually not narrow enough for WDM applications. However, cascaded M-Z configurations can produce narrower filters [27]. The tuning of M-Z filter can be achieved by changing the refractive index of one arm using the electrooptic

effect.

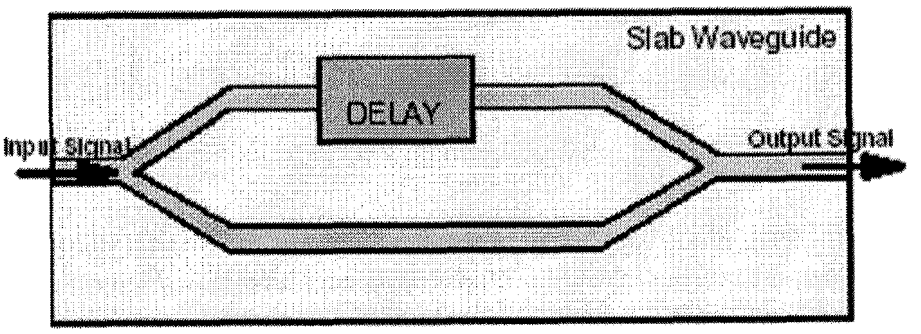

Figure 2.9 Schematic diagram of a Mach-Zehnder interferometer filter.

The interaction between a lightwave and a surface acoustic wave (SAW) over a suitable substrate causes a polarization shift at frequencies that satisfy the phase-matching condition. When combined with two polarization splitters, an efficient AOTF can be constructed to select only the small bandwidth that satisfies the phase-matching condition (see Fig. 2.10) [28]. The characteristics of this type of AOTF will be illustrated in details in Chapter 4.

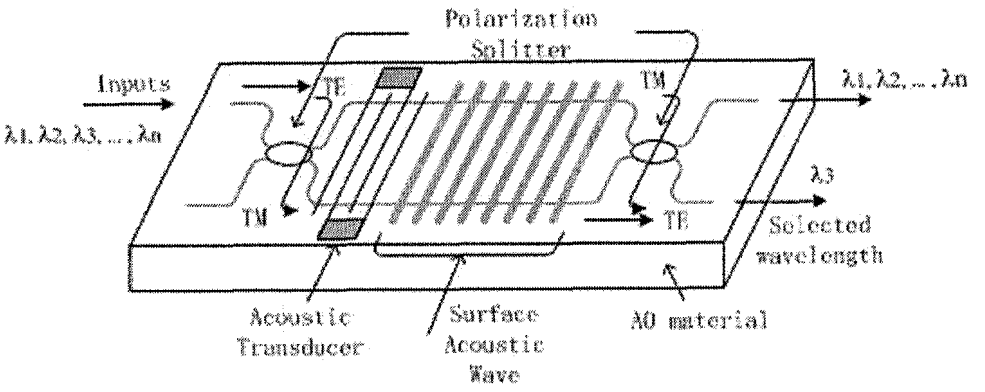

Figure 2.10 The schematic diagram of an AOTF based on the waveguide technology.

The operating principle of electrooptical tunable filters (EOTFs) is similar to that of AOTFs. The periodic perturbation of refractive index is induced by the electrooptic effect using electrodes positioned in equal space along the electrooptical waveguide (see Fig. 2.11). The polarization mode coupling occurs when the phase-matching condition is satisfied in a narrow frequency range. Tuning is achieved by a uniform electric field that tunes the average refractive index [29].

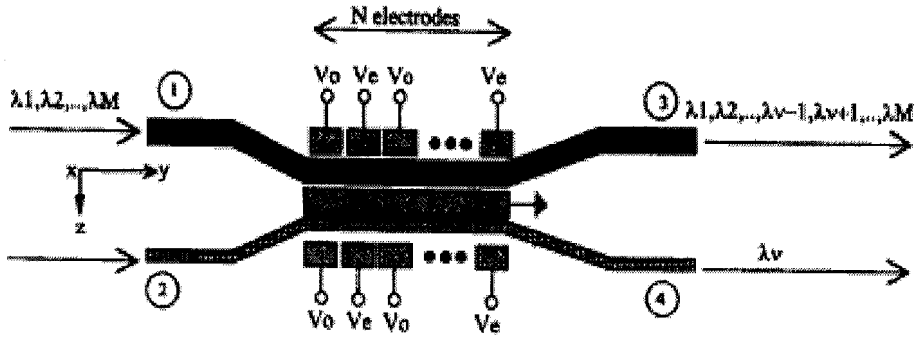

Figure 2.11 The schematic diagram of an electrooptical tunable filter [29].

A lightwave passing through an array of waveguides produces an interference pattern. The spatial intensity distribution is a function of the optical path length difference of the grating, the wavelength, and the angle of incidence of the light. In this way, different wavelengths will be diffracted at different angles (i.e., spatially separated). Wavelength tuning can also be achieved by using an array waveguide grating that is controlled by thermooptic switches (see Fig. 2.12) [30].

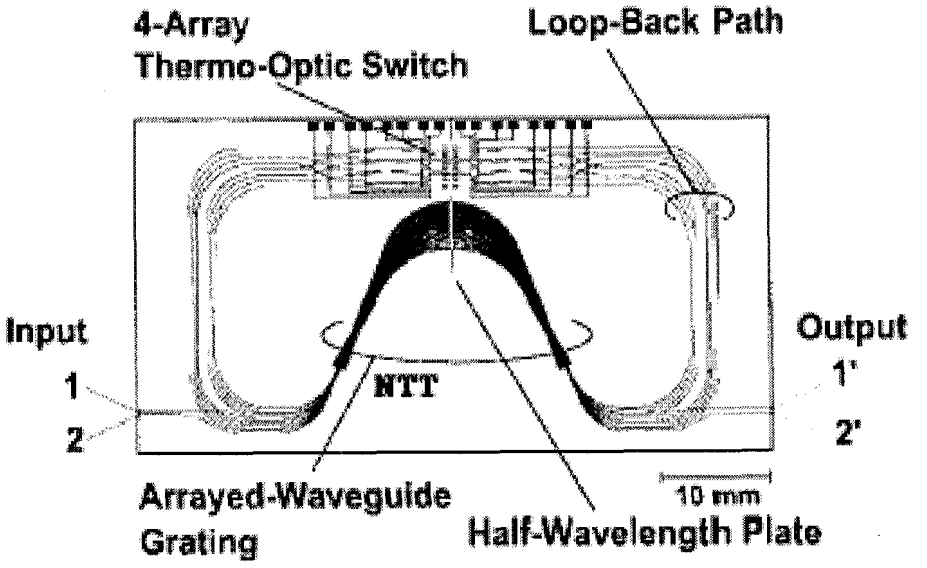

Figure 2.12 Circuit layout of a fabricated monolithically-integrated wavelength-selective switch [30].

A simple tunable filter based on a fiber ring resonator typically consists of a fiber coupler, a fiber loop and an adjustable phase shifter (see Fig. 2.13). The coupler is designed to optimize the filter performance in terms of transmitted power and bandwidth. The spectral transmission characteristics of the ring resonator are similar to those of F-P filters. The tunable phase shifter allows external control of the phase-matching condition of the loop resonator [31]. A change of the phase-matching condition leads to a frequency shift of the resonance frequency, which is proportional to the phase shift imposed by the phase shifter.

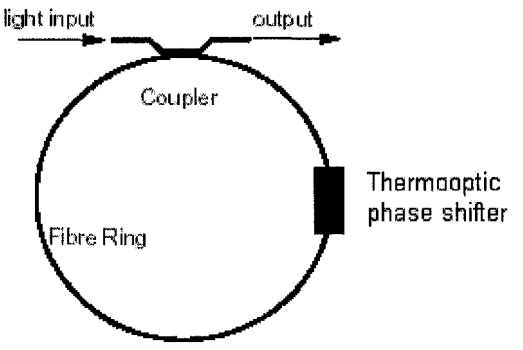

Figure 2.13 Construction of a fiber ring resonator.

2.6 Summary

Table 3.1 summarizes the important parameters of the various technologies of tunable optical filters that have been reviewed in this chapter. Tunable F-P filters are generally only suitable for low-speed network applications, and their tuning range is smaller than the operating band of an erbium-doped fiber amplifier (EDFA). M-Z interferometers suffer from low finesse and must be combined with additional wavelength selective elements, such as FBGs for applications that require narrow-bandwidth filters. AOTFs can perform multiple channel selection but suffer from large sidelobes and wide bandwidth. EOTFs offer high-speed tuning capability but also suffer from large sidelobes and wide bandwidth. AWGs should be used in combination with additional switching devices to achieve tunability. Tunable ring resonator filters presently make use of the thermal effect to achieve the tuning. However, they have potential for high-speed tuning by using current injection technique [32].

The FBG-based filters offering negligible insertion loss and good filtering shape is one of most promising tunable filters for photonics applications.

Type	**Insertion loss**	**Bandwidth**	**Tuning range**	**Tuning speed**	**Tuning method**
F-P	2 dB	< 0.5 nm	~ 10 nm	ms	PZT
M-Z	19 dB ($LiNbO_3$)	< 0.2 nm	~ 4 nm	50 ns	Electro-optic
AOTF	4 dB	~ 1.5 nm	> 60 nm	μs	Acousto-optic
EOTF	4 dB	~ 1.5 nm	~ 50 nm	ns	Electro-optic
AWG	8 dB	< 0.2 nm	~ 40 nm	10 ms	Thermo-optic
Ring resonator	3 dB	~ 0.2 nm	25 nm	ms	Thermo-optic
FBG	0.1 dB	< 0.2 nm	< 40 nm	2 ms	Thermal & strain

Table 2.1 Performance comparison of various tunable filter technologies.

2.7 Conclusion

The theory, characteristics, fabrication, and application of FBGs have been presented in this chapter. FBG is one of the most promising optical filters for use in the telecommunication systems. Furthermore, due to its temperature sensitivity and strain sensitivity, FBGs can be used for the development of TOFs for application in the next generation of dynamical optical networks. Besides FBGs, some other techniques of TOFs have been briefly discussed in this chapter, which include the F-P interferometer tunable filter, M-Z interferometer tunable filter, AOTF, electrooptical tunable filter, AWG-based tunable filter, and ring resonator tunable filter. Comparing with other tunable optical filtering technologies, FBGs have advantages which include low

insertion loss, sharp filtering shape, easy tunability, fiber geometry, compact size, polarization insensitivity, and low cost.

2.8 References

[1] K. O. Hill, Y. Fujii, D. Johnson and B. Kawasaki, "Photosensitivity in optical fiber waveguides: application to reflection filter fabrication," *App. Phys. Lett.* vol. 32, pp. 647–649, 1978.

[2] G. Meltz, W. Morey and W. H. Glenn, "Formation of Bragg gratings in optical fibers by a transverse holographic method," *Opt. Lett.,* vol. 14, pp. 823–825, 1989.

[3] P. J. Lemaire, R. M. Atkins, V. Mizrahi and W. A. Reed, "High pressure H_2 loading as a technique for achieving ultrahigh UV photosensitivity and thermal sensitivity in GeO_2 doped optical fibres," *Electron. Lett.*, vol. 29 , pp. 1191–1193, 1993.

[4] D. P. Hand and P. St. J. Russell, "Photoinduced refractive-index changes in germanosilicate fibers," *Opt. Lett.,* vol. 15, pp. 102–104, 1990.

[5] H. G. Limberger *et al.*, "compaction and photoelastic-index changes in fiber Bragg gratings," *App. Phys. Lett.*, vol. 68, pp. 3069–3071, 1996.

[6] A. Othonos and K. Kalli, *Fiber Bragg gratings: fundamentals and applications in telecommunications and sensing,* Artech House, 1999.

[7] B. S. Kawasaki *et al.*, "Narrow-band Bragg reflectors in optical fibers," *Opt. Lett.*, vol. 32, pp. 66–68, 1978.

[8] K. O. Hill *et al.*, "Bragg gratings fabricated in monomode photosensitive optical fiber by UV exposure thorough a phase mask," *App. Phy. Lett.*, vol. 62, pp. 1035–1037, 1993.

[9] B. Malo *et al.*, "Point-by-point fabrication of micro-Bragg gratings in photosensitive fiber using single excimer pulse refractive index modification techniques," *Electron. Lett.*, vol. 29, pp. 1668–1669, 1993.

[10] St. J. P. Russell *et al.*, "Bloch wave analysis of dispersion and pulse propagation in pure distributed feedback structures," *J. of Modern Opt.*, vol. 38, pp. 1599–1619, 1991.

[11] A. Yariv, "Coupled-mode theory for guided-wave optics," *IEEE J. Quantum Electron.*, vol. QE-9, pp. 919–933, 1973.

[12] K. A. Winick, "Effective-index method and coupled-mode theory for almost periodic waveguide gratings: a comparison," *App. Opt.*, vol. 31, pp. 757–764, 1992.

[13] T. Erdogan, "Fiber grating spectra," *IEEE J. Lightwave Technol.*, vol. 15, pp. 1277–1294, 1997.

[14] A. Iocco, H. G. Limberger, R. P. Salathe, L. A. Everall, K. E. Chisholm, J. A. R. Williams and I. Bennion, "Bragg grating fast tunable filter for wavelength division multiplexing," *IEEE J. Lightwave Technol.*, vol. 17, pp. 1217–1221, 1999.

[15] E. R. Lyons and H. P. Lee, "Demonstration of an etched cladding fiber Bragg grating filter with reduced tuning force requirement," *IEEE Photon. Technol. Lett.*, vol. 11, pp. 1626–1628, 1999.

[16] J. L. Arce, J. M. Lopez-Higuera and M. A. Muriel, "A new tunable optical filter based on the Faraday effect on a Bragg grating," *Lasers and Electro-Optics Society Annual Meeting, LEOS 96, IEEE*, vol. 2, pp. 307–308, 1996.

[17] C. S. Goh, M. R. Mokhtar, S. A. Butler, S. Y. Set, K. Kikuchi and M. Ibsen, "Wavelength tuning of fiber Bragg gratings over 90 nm using a simple tuning package," *IEEE Photon. Technol. Lett.*, vol. 15, pp. 557–559, 2003.

[18] J. L. Cruz, A. Diez, M. V. Andres, A. Segura, B. Ortega and L. Dong, "Fibre Bragg gratings tuned and chirped using magnetic fields," *Electron. Lett.*, vol. 33, pp. 235–236, 1997.

[19] S. Jin, P Espindola, H. Mavoori, A. Strasser and J. J. DeMarco, "Magnetically programmable fibre Bragg gratings," *Electron. Lett.*, vol. 34 , pp. 2158–2159, 1998.

[20] H. G. Limberger, H. K. Nguyen, D. M. Costantini, R. P. Salathe, C. A. P. Muller and G. R. Fox, "Efficient miniature fiber-optic tunable filter based on intracore Bragg grating and electrically resistive coating," *IEEE Photon. Technol. Lett.*, vol. 10, pp. 361–363, 1998.

[21] E. R. Lyons and H. P. Lee. "An efficient electrically tunable etched cladding fiber Bragg grating filter tested under vacuum," *IEEE Photon. Technol. Lett.*, vol. 13, pp. 484–486, 2001.

[22] B. Srinivasan and R. K. Jain, "First demonstration of thermally poled electrooptically tunable fiber Bragg gratings," *IEEE Photon. Technol. Lett.*, vol. 12, pp. 170–172, 2000.

[23] P. St. J. Russell and W. F. Liu "Acousto-optic superlattice modulation in fiber Bragg gratings," *J. Opt. Soc. Am. A*, vol. 17, pp. 1421–1429, 2000.

[24] D. Yeom, H. S. Park and B. Y. Kim; "Tunable narrow-bandwidth optical filter based on acoustically modulated fiber Bragg grating," *IEEE Photon. Technol. Lett.*, vol. 16, pp. 1313–1315, 2004.

[25] J. Stone and L. W. Stulz, "Pigtailed high finesse tunable FP interferometer with large, medium, and small FSR," *Electron. Lett.*, vol. 23, pp. 781–783, 1987.

[26] http://www.micronoptics.com/ffp-tf2.htm

[27] L. Wooten *et al.*, "Rapidly tunable narrowband wavelength filter using $LiNbO_3$ unbalanced Mach-Zehnder interferometers," *IEEE J. Lightwave Technol.*, vol. 6, pp. 1011–1015, 1988.

[28] H. Herrmann, K. Schafer and C. Schmidt, "Low loss tunable integrated acoustooptical wavelength filter in $LiNbO_3$ with strong sidelobe suppression," *IEEE Photon. Technol. Lett.*, vol. 10, pp. 120–122, 1998.

[29] D. Brooks and S. Ruschin, "Integrated electrooptic multielectrode tunable filter," *IEEE J. Lightwave Technol.*, vol. 13, pp. 1508–1513, 1995.

[30] S. Suzuki *et al.*, "Integrated multichannel optical wavelength selective switches incorporating an arrayed-waveguide grating multiplexer and thermooptic switches," *IEEE J. Lightwave Technol.*, vol. 16, pp. 650–655, 1998.

[31] C. Vazquez, S. Vargas, J.M.S. Pena and P. Corredera, "Tunable optical filters using compound ring resonators for DWDM," *IEEE Photon. Technol. Lett.*, vol. 15, pp. 1085–1087, 2003.

[32] J. W. Gray, Y. S. Jalili, P. N. Stavrinou, M. Whitehead, G. Parry, A. Joel, R. Robjohn, R. Petrie, S. Hunjan, P. Gong and G. Duggan, "High-efficiency, low voltage resonant-cavity light-emitting diodes operating around 650 nm," *Electron. Lett.*, vol. 36 , pp.1730–1731, 2000.

3 Tunable Dispersion Compensated Filters

3.1 Introduction

Dispersion refers to any effect that causes different components of a transmitted signal to propagate at different velocities in an optical fiber [1]. Dispersion in optical fibers results in the spread of an optical pulse in the time domain having propagated through a fiber link. Fiber dispersion causes interference between adjacent pulses due to the spread of the pulses, and this limits the transmitted distance of the optical signal. Dispersion can be divided into three main types, which are modal dispersion (or intermodal dispersion), chromatic dispersion (intramodal dispersion), and polarization mode dispersion. As presented in this chapter, the focus of this work is on the compensation of fibre chromatic dispersion, which is significant in a singlemode fiber at a wavelength of 1550 nm. In a singlemode fiber, the optical waves of different wavelengths propagate at different velocities, and this is due to the presence of chromatic dispersion in the fiber. Two main factors of chromatic dispersion are briefly described below:

- *Material dispersion*, which occurs due to the variation of the refractive index of the core material as a function of wavelength. As a result, the different wavelength components of an optical pulse are separated from each other after propagating through the optical fiber.
- *Waveguide dispersion*, which occurs because the various wavelength components of an optical pulse travel with slightly different group velocities in the fiber.

3.1.1 Signal Distortion Due to Fiber Dispersion

One of the most critical challenges in the next generation of high-speed long-haul optical transmission systems is to overcome fiber chromatic dispersion, which is the dominant dispersion mechanism in a singlemode fiber. The effect of signal distortion due to chromatic dispersion can be illustrated in Figure 3.1. As shown in Figure 3.1, the two sufficiently separated optical input pulses in a singlemode fiber at time t_0 are broadened and overlap with each other after time t_1 due to the effect of chromatic dispersion after propagating some distance along the fiber (i.e. at time t_1). After propagating a further distance (i.e. at time t_2), these two pulses will become indistinguishable resulting in transmission error at the end of the fiber link.

In the past ten years or so, with many improvements in the performance of laser sources and detectors and the shift of the optical communication window to the 1550 nm band, the transmission speeds in practical optical networks have at least been doubled every two years or so. The modulated optical signal

has its bandwidth broadened by twice the modulation frequency. That is, if one modulates a signal at 40 GHz then the bandwidth of the modulated optical signal will be broadened to 80 GHz. This broadened bandwidth can result in significant pulse broadening due to chromatic dispersion in the fiber. Furthermore, when one doubles the transmission speed, the width of a pulse in the time domain will be halved. The result is that the same amount of dispersion will have twice the effect it had before. Arising from the above, the conclusion is that the effect of dispersion will be amplified by a factor of four when doubling the transmission speed. Thus the dispersion tolerances will be four times more rigid with doubling of the transmission speed. For example, an optical signal that could travel over 1000 km of a standard single-mode fiber in a 2.5 Gb/s network without regeneration can only travel 60 km unregenerate in a 10 Gb/s network, and only 15 km in a 20 Gb/s network [2].

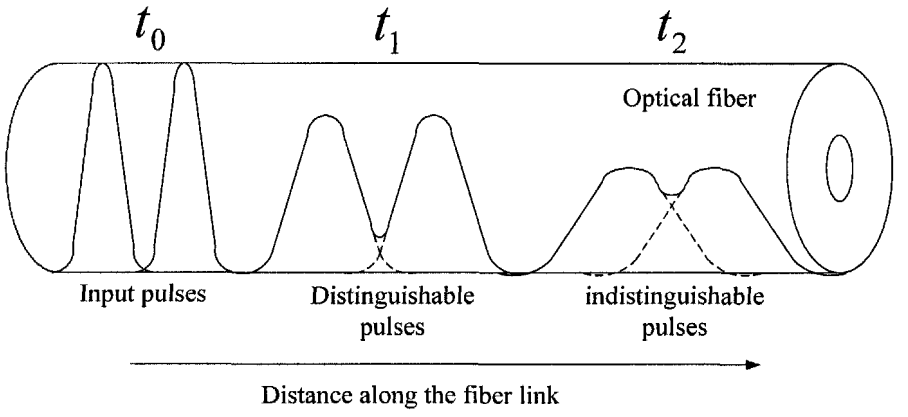

Figure 3.1 Broadening and attenuation of two adjacent pulses as they travel along an optical fiber due to the effect of chromatic dispersion.

3.1.2 Variation of Dispersion in Fiber Link

The variation in fiber chromatic dispersion due to the changing operating conditions of the systems can greatly degrade the system performance, especially in high-speed systems (e.g. 40 Gb/s systems) because of the rigid dispersion tolerance. There are several factors that cause dispersion variations.

- First, when the gain profiles of the in-line amplifiers are not flat, different WDM signals will experience different amount of gain along the transmission link, and this could introduce an additional nonlinear phase shift due to self-phase modulation (SPM) and cross-phase modulation (XPM) in the fiber, and this effect can result in dispersion variation [3].
- Second, environmental variations such as changes in the ambient temperature can also cause the system dispersion to vary [4].
- Furthermore, dynamic reconfigurations of a network to route a particular wavelength channel to a particular location will cause the accumulated dispersion along the link to vary because the total path taken by a particular wavelength channel from the source to the destination can vary [5].

For high-speed systems (e.g. 40 Gb/s), the dispersion tolerance for the system is very rigid. Hence, the residual variation of dispersion at the end of the link that can be neglected in the lower speed systems will greatly degrade the performance of the high-speed systems. To overcome the problems induced by the dispersion variation, tunable dispersion compensators are needed. The

tunable dispersion compensators can be used to dynamically adjust the dispersion map, and hence to minimize the impairment induced by the chromatic dispersion and variation of dispersion.

3.1.3 Existing Dispersion Compensation Methods

Existing dispersion compensation methods include pre-compensation and post-compensation schemes. The pre-compensation schemes involve the modification of the characteristics of input pulses at the transmitter output before they are launched into the fiber link. The pre-compensation schemes include prechirped technique [6]–[8], novel coding techniques (e.g. frequency-shift keying (FSK) format [9], duobinary coding [10]), and nonlinear prechirped techniques [11]. The post-compensation schemes include dispersion-compensating fibers [12]–[15], interferometric filters [16], [17], and fiber Bragg gratings [18], [19].

3.1.4 Chirped Fiber Bragg Gratings

As described in Chapter 2, a chirped fiber Bragg grating (FBG) is an FBG with monotonically varying period and/or monotonically varying refractive index. Figure 3.2 shows a schematic diagram of a chirped FBG with length L_g and chirped bandwidth $\Delta\lambda_{chirp}$. From Eq. (2.10), the local Bragg wavelength of a chirped FBG is given by [2]

$$\lambda_B(z) = 2n_{eff}(z)\Lambda(z) \tag{3.1}$$

where λ_B is the Bragg wavelength, n_{eff} is the effective index of the silica fiber, Λ is the grating period, and z is the distance along the fiber. Hence, the total chirp of the grating period, $\Delta\Lambda_{chirp}$, is related to the chirped bandwidth of the grating as

$$\Delta\lambda_{chirp} = 2n_{eff}\left[\Lambda(L) - \Lambda(0)\right] = 2n_{eff}\Delta\Lambda_{chirp} \tag{3.2}$$

where $\Lambda(L)$ and $\Lambda(0)$ are the grating period at the end and start positions respectively.

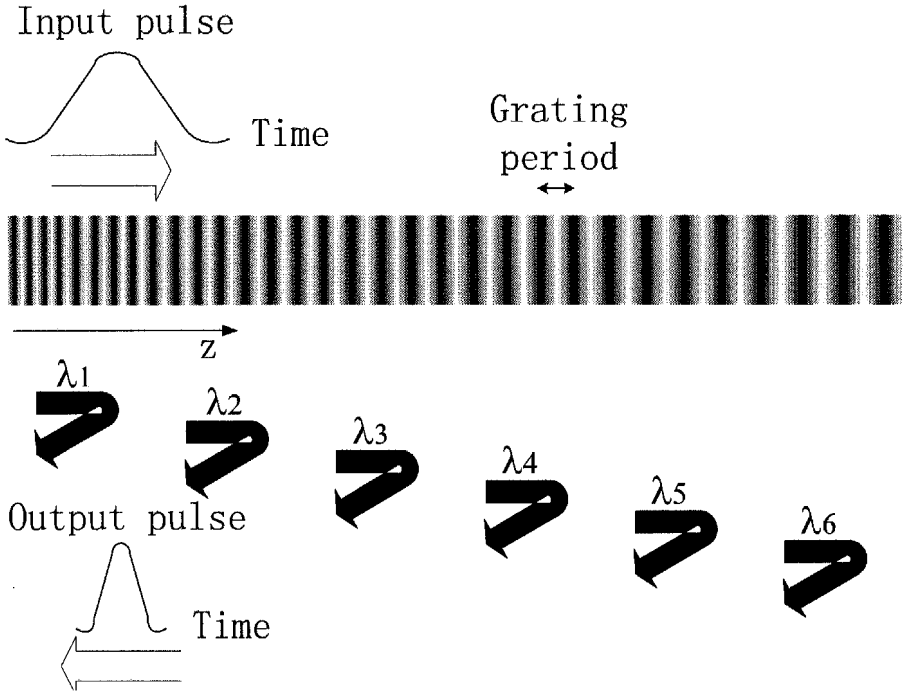

Figure 3.2 Operating principle of a chirped FBG as a dispersion compensator, λi is the reflected Bragg wavelength component of an input pulse.

It is noted from Eq. (3.1) that the Bragg wavelength varies along the chirped FBG. That is, the different wavelength components of an optical signal will be reflected at different positions along the chirped FBG. As a result, the optical

waves of different wavelengths will experience different group delay in the chirped FBG. And this group delay characteristic can be used to compensate for the chromatic dispersion in the fiber link. The dispersion of a linearly chirped FBG with positive chirp rate can be estimated by [2]

$$D(\lambda) = \frac{d\tau(\lambda)}{d\lambda} = \frac{d\left[\frac{\lambda - \lambda_0}{\Delta\lambda_{chirp}} \frac{2L}{v}\right]}{d\lambda} = \frac{2L}{\Delta\lambda_{chirp} v} \tag{3.3}$$

where λ_0 is the Bragg wavelength at the start end, v is the average group velocity of the light in the fiber, L is the length of the FBG, and λ is the wavelength of the input light.

It can be seen from Eq. (3.3), that the chirped FBG can be used to compensate for the chromatic dispersion in the fiber link. The chirped FBG with different length and/or different chirped bandwidth can be used to compensate for different amount of chromatic dispersion in fibers of different lengths. Furthermore, the tunable dispersion compensators can be designed by adjusting the chirped bandwidth of the chirped FBG.

There are several techniques reported on the fabrication of the chirped FBG. The first report of the fabrication of a chirped FBG was by Byron *et al.* [20] who used a conventional two-beam ultraviolet (UV) interferometer to produce a uniform-period pattern in a tapered photosensitive fiber. The approximately linear variation of the fiber effective index along the tapered section will produce a chirp in the grating. Other fabrication methods include bending fiber

method [21], tilting fiber method [22], applying non-uniform strain [23], UV post-processing technique [24] and mostly used chirped phase mask technique [25].

3.1.5 Tunable Dispersion Compensators Based on Chirped Fiber Bragg Gratings

Chirped FBGs (CFBGs) have been used to compensate for the chromatic dispersion dynamically in optical communication systems due to their unique advantages, which include inherent fiber compatibility, low loss, simple tuning mechanism, low cost and polarization insensitivity [26]. The dispersion of a CFBG can be tuned by adjusting the chirp on the fiber grating using externally applied perturbation such as temperature perturbation [27]–[29] and strain perturbation [18], [30]–[32]. Recently, an electrically tunable CFBG has been developed using an on-fiber thin-film heater [19].

Figure 3.3 illustrates the concept of tuning the induced dispersion of a nonlinearly chirped FBG using an external mechanical stretching element [18]. Before applying strain to the nonlinearly chirped FBG, the dispersion at a particular wavelength λ_0 is D_0. After applying the strain to the grating by means of stretching, the whole Bragg wavelength band is shifted to the longer wavelength side. As a result, the dispersion value corresponding to the wavelength λ_0 will be changed to D_1 because of the characteristics of the nonlinearly chirped FBG.

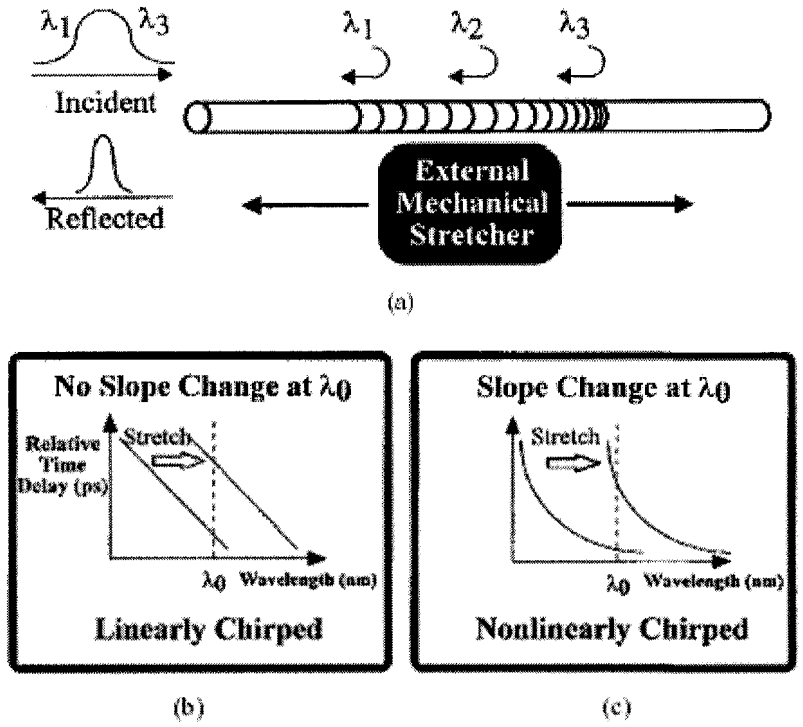

Figure 3.3 (a) Schematic diagram of a tunable dispersion compensator based on a nonlinearly chirped FBG. Also shown is the time delay as a function of wavelength for (b) a linearly chirped FBG and (c) a nonlinearly chirped FBG [18].

Figure 3.4 illustrates the tuning principle of a chirped FBG using an on-fiber thin-film heater [19]. The chirp in the grating can be produced by using an on-fiber coating whose thickness varies with position along the length of the grating in a prescribed manner. When applying a DC voltage to the thin-film coating, a temperature gradient is obtained in the grating area, and due to the thermo-optical effect, a chirp will be introduced into the grating as a result of the change in the refractive index. The chirp rate can be adjusted by varying the applied current.

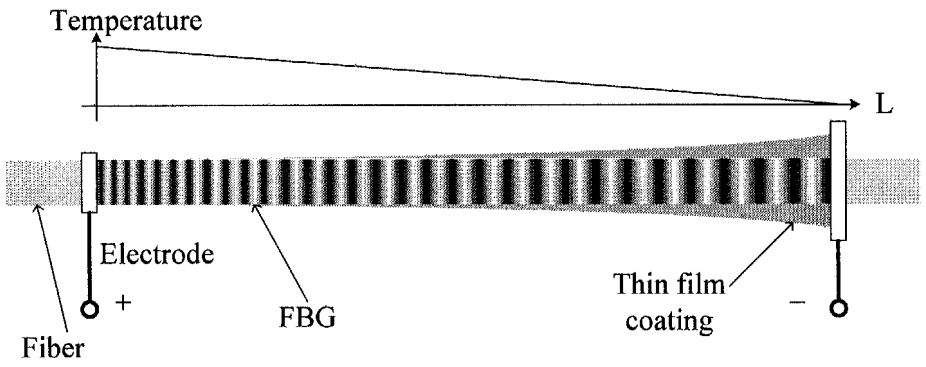

Figure 3.4 Schematic diagram of a dispersion tunable FBG based on an on-fiber thin-film heater.

However, a critical problem faced by most methods to adjust the chirp of the fiber grating is the large shift in the center wavelength of the filter passband in order to increase the dispersion tuning range. Because of the large center wavelength shift, the passband of the dispersion compensating FBG may not be able to capture the complete spectrum of the signal to be compensated and hence may cause distortion of the signal spectrum. Tunable dispersion compensators with a fixed central wavelength are thus highly desirable.

Several methods have been proposed for tuning the chirp of the FBG with a fixed central wavelength such as those using mechanical structures [33]–[35]. Because of the complexity and bulky size of the control mechanisms, these devices are not attractive for telecommunication system applications. An interesting method was proposed by J. A. Rogers *et al.* [36]. They employed a taper on-fiber thin-film heater to adjust the chirp of the FBG as well as another uniform thin-film heater inside the taper on-fiber thin-film heater to keep the

central wavelength fixed. But this method requires two independent control sources, which makes it costly and more difficult to control.

3.2 Proposed Tunable Dispersion Compensator

This section presents the design and development of a new tunable dispersion compensator that can electrically adjust the chirp of an FBG with almost-fixed center wavelength by changing the temperature gradient and strain gradient on the FBG in a prescribed manner. At the same time, the center wavelength of the operating band of the FBG is maintained almost-fixed during the tuning process.

3.2.1 Operating Principle

Figure 3.5 shows the schematic diagram of the proposed tunable dispersion compensating filter based on FBG. This electrically tunable CFBG device consists of an intracore uniform FBG in a fiber that is etched to a prescribed diameter profile, an on-fiber thin-film heater whose local resistance varies with position in a prescribed manner along the grating length, and a negative thermal expansion coefficient (NTEC) ceramic with a conductive paint layer on the surface. The FBG with the thin-film heater is mounted in the NTEC ceramic under pre-tension. The electrodes make contact with both the conductive paint and thin-film coating. Appling the pre-tension avoid bending the fiber when the FBG is under compression.

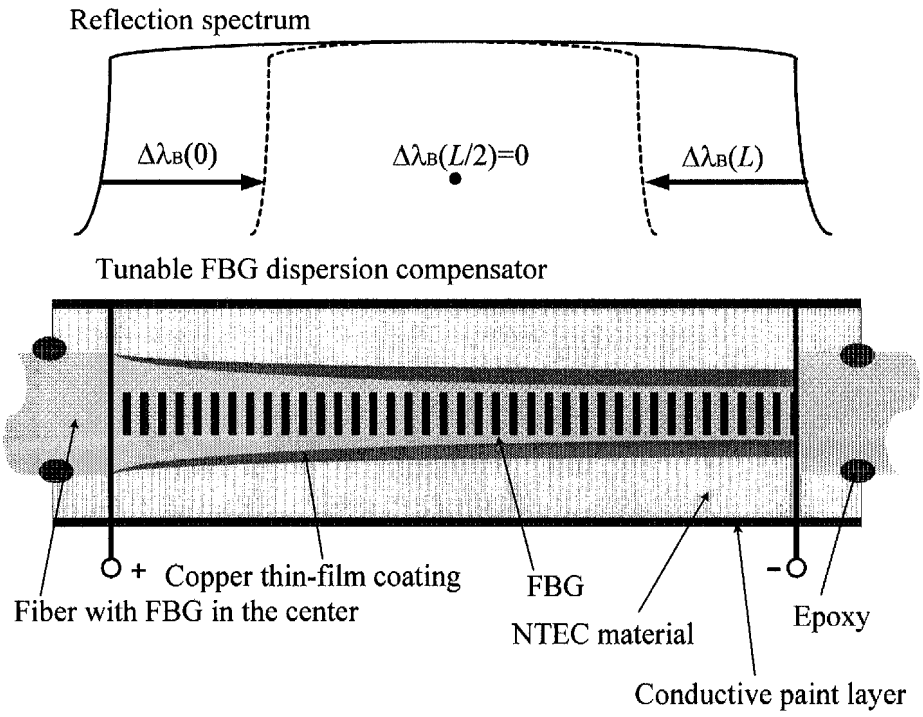

Figure 3.5 Schematic diagram of the proposed tunable dispersion compensating FBG with fixed central wavelength. When current flows through the thin-film coating and the conductive paint layer, the bandwidth and chirp of the FBG can be tuned while the center wavelength is kept fixed.

Electrical current flowing through the thin film generates a temperature gradient because of the prescribed thickness profile of the metal film. At the same time, the current flowing through the conductive paint heats the NTEC ceramic resulting in the shrinkage of the NTEC ceramic, and this imposes a strain gradient on the FBG because of the diameter profile of the fiber with FBG. Both the temperature gradient and strain gradient reduce the original chirp imposed by the pre-tension, and hence the dispersion of the FBG can be adjusted. The center wavelength can be kept fixed because the effect of

temperature rise, which shifts the center wavelength of the reflection spectrum to the longer wavelength side, and the compression of FBG, which shifts the center wavelength of the reflection spectrum to the shorter wavelength side, can be made to offset each other.

To the author's knowledge, this is the first proposal to combine the temperature gradient and strain gradient as a dispersion tuning technique using a CFBG. As an example to demonstrate the effectiveness of the proposed method, a tunable linearly chirped FBG of 25 mm length has been developed, and it has a dispersion tuning range of −178 ps/nm to −302 ps/nm with a central wavelength shift of as small as 0.16 nm and an applied electrical power smaller than 0.68 W.

3.2.2 Design and Construction

The shift of the Bragg wavelength, $\Delta\lambda_B(z)$, at an axial point z along the CFBG is determined by the temperature change at that point, $\Delta T(z)$, [37] and the strain change at that point, $\Delta\varepsilon(z)$, [38] as

$$\Delta\lambda_B(z) = \lambda_B(\alpha+\xi)\Delta T(z) + \lambda_B(1-p_e)\Delta\varepsilon(z) \qquad \textbf{(3.4)}$$

where λ_B is the Bragg wavelength, α the expansion coefficient (for silica, it is typically ~0.55×10^{-6} /°C), ξ the thermo-optic coefficient (for silica, it is typically ~8.6×10^{-6} /°C), and p_e is the photoelastic coefficient (for silica, it is typically ~0.21).

The proposed dispersion compensating device is schematically shown in Fig. 3.5. When an electrical current flows through the thin-film coating and the conductive paint layer, the resistive heat will shift the Bragg wavelength to the longer wavelength side. At the same time, shrinkage of the NTEC ceramic will compress the FBG and will shift the Bragg wavelength to the shorter wavelength side. In Fig. 3.5, on the thinner side of the thin-film coating (i.e. on the left side of the diagram), the thermal effect is larger than the strain effect so the Bragg wavelength at this point, $\lambda_B(0)$, will shift to the longer wavelength side resulting in a wavelength change of $\Delta\lambda_B(0)$. On the thicker side of the thin-film coating (i.e. on the right side of the diagram), the strain effect is larger than the thermal effect so the Bragg wavelength at this point, $\lambda_B(L)$, will shift to the shorter wavelength side resulting in a wavelength change of $\Delta\lambda_B(L)$, where L is the length of the FBG. The total chirp of this device can be adjusted and it relates to the bandwidth change of the CFBG. At the middle of the FBG, the strain effect and the thermal effect will offset each other so the Bragg wavelength at this point, $\lambda_B(L/2)$, will be kept fixed (i.e. $\Delta\lambda_B(L/2)=0$). For a linearly chirped FBG, the Bragg wavelength at the middle of the FBG, $\lambda_B(L/2)$, corresponds to the central wavelength of the reflection band. As a result, the center wavelength can be kept fixed when tuning the chirp and hence dispersion of the FBG.

3.2.3 Design Profiles of Coating Thickness and Fiber Diameter

A linear chirp is required in the design of a dispersion compensating FBG for compensation of the fiber chromatic dispersion. Hence, the thickness profile of the thin-film coating and the diameter profile of FBG should be properly designed. For the sake of simplicity and without loss of generality, it is assumed that:

1. The temperature distribution in the core of the fiber follows the distribution of heating power produced by the resistive film;
2. The resistivity of the metal is not strongly dependent on temperature;
3. An increase in temperature is linearly related to the heating power [29], [39].

Using these assumptions, which are valid, it is possible to derive the cross-sectional area of the thin-film coating along the fiber that is required to generate a linear temperature gradient (and hence linear chirp) on the FBG.

The local resistance should be linearly distributed along the length of FBG to introduce a linear temperature gradient because of the temperature change, $\Delta T \sim I^2 R$, where I is the electrical current applied to the thin-film metal coating and R is the resistance of the metal coating. The local resistance is proportional to the reciprocal of the cross-sectional area of the thin-film coating, $A_c(z)$, which is $R \sim 1/A_c(z)$. The local cross-sectional area of the thin-film coating can thus be expressed as

$$A_c(z) = \frac{LA_c(L)A_c(0)}{[A_c(0) - A_c(L)]z + LA_c(L)} \tag{3.5}$$

where L is the length of FBG, and $A_c(0)$ and $A_c(L)$ are the cross-sectional areas of the thin-film coating at the beginning and end of the FBG, respectively. z is the axial position along the grating ($0 \le z \le L$).

For the sake of simplicity and without loss of generality, it is further assumed that: 1) the thin-film coating is tightly adhered to the fiber; 2) the change in the Young's modulus of the coating and in the silica fiber with an increase in the temperature is negligible; and 3) there is only axial tension applied to the fiber. The local axial strain introduced by the applied tension is given by

$$\varepsilon(z) = \frac{F}{E_c A_c(z) + E_f A_f(z)} \tag{3.6}$$

where F is the axial tension applied to the grating; E_c the Young's modulus of the thin-film coating material (for copper, E_c = 1.1×10^{11} N/m^2); E_f the Young's modulus of silica (E_f = 7.25×10^{10} N/m^2); $A_c(z)$ the local cross-sectional area of the resistive thin-film coating as defined in Eq. (3.5), and $A_f(z)$ is the local cross-sectional area of the FBG.

To introduce a linear chirp on the FBG, a linear axial strain gradient on the FBG is required. Under this condition, the local cross-sectional area of FBG, $A_f(z)$, can be derived from Eqs. (3.5) and (3.6) as

$$A_f(z) = \frac{1}{E_f(mz+n)} - \frac{E_c}{E_f} A_c(z) \tag{3.7}$$

where

$$m = \frac{1}{L\left[E_c A_c(L) + E_f A_f(L)\right]} - \frac{1}{L\left[E_c A_c(0) + E_f A_f(0)\right]} \tag{3.8}$$

$$n = \frac{1}{E_c A_c(0) + E_f A_f(0)} \tag{3.9}$$

where $A_f(0)$ and $A_f(L)$ are the cross-sectional areas of the FBG at the beginning and end of the FBG, respectively. The diameter profile of FBG, $D(z)$, can be derived from Eq. (3.7) as

$$D(z) = 2\sqrt{\frac{A_f(z)}{\pi}} = 2\sqrt{\frac{1}{\pi E_f(mz+n)} - \frac{E_c}{\pi E_f} A_c(z)} \tag{3.10}$$

When the diameter of FBG is much larger than the thickness of the thin-film coating, the thickness profile of the thin-film coating, $H(z)$, can be approximately given by

$$H(z) = \frac{A_c(z)}{\pi D(z)} \tag{3.11}$$

Figure 3.6 shows the simulation results of the designed profile based on Eqs. (3.10) and (3.11). In this design, the length of the FBG is 25 mm, the diameter of the tapered FBG varies from 125 μm to 90 μm, and the thickness of the thin-film coating varies from 1 μm to 5 μm. Figures 3.6(a)–(c) represent the radius profile of FBG, the thickness profile of the thin-film coating and the total radius profile of FBG with the thin-film coating. Fabrication of the

tunable dispersion compensator based on this design is presented in Section 3.3.

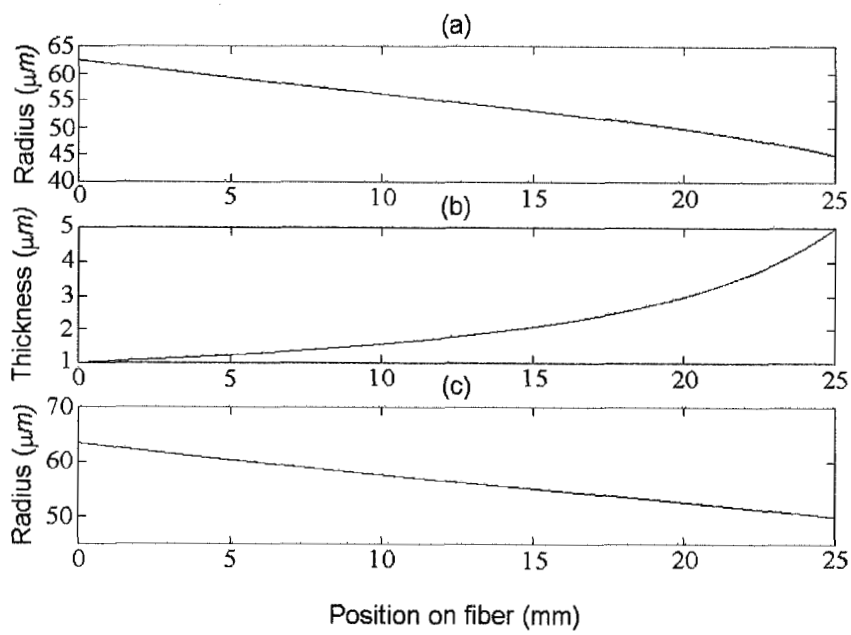

Figure 3.6 (a) Radius profile of a 25 mm long FBG, where the prescribed radii at z = 0 and z = 25 mm positions are 62.5 μm and 45 μm, respectively. (b) Profile of the thickness of the copper thin film, where the prescribed thicknesses at z = 0 and z = 25 mm positions are 1 μm and 5 μm, respectively. (c) Total radius profile with thin-film coating.

3.2.4 Fixing the Center Wavelength of a Chirped FBG

From the fiber diameter profile as defined in Eqs. (3.5) and (3.10) and the coating thickness profile as defined in Eqs. (3.5) and (3.11), it can be seen that the temperature gradient and strain gradient on the fiber grating are linear, and this characteristic introduces a linear chirp in the fiber grating, which can be

used to compensate for the fiber chromatic dispersion. The center wavelength of the operating band is fixed, the effects of temperature and strain on the center Bragg wavelength $\lambda_B(L/2)$ must offset each other as explain earlier in Section 3.2.1. To achieve this, one must design the thickness or resistance of the conductive painting deposited on the NTEC material in such a way as to ensure that the shrinkage of the NTEC material and the temperature increase will offset each other.

For a linearly chirped FBG, the central wavelength shift is the Bragg wavelength shift at the $z = L/2$ position, which is given by

$$\Delta\lambda_B(L/2) = \lambda_B(\alpha+\xi)\Delta T(L/2) + \lambda_B(1-p_e)\Delta\varepsilon(L/2) \tag{3.12}$$

and the change in bandwidth is given by

$$\Delta\lambda_{chirp} = \lambda_B(\alpha+\xi)[\Delta T(L) - \Delta T(0)] + \lambda_B(1-p_e)[\Delta\varepsilon(L) - \Delta\varepsilon(0)] \tag{3.13}$$

To keep the center wavelength fixed, the Bragg wavelength shift at the middle of FBG should be zero. That is, $\Delta\lambda_B(L/2) = 0$ is used in Eq. (3.12) and the following relationship is obtained

$$\frac{\Delta T(L/2)}{\Delta\varepsilon(L/2)} = -\frac{1-p_e}{\alpha+\xi} \tag{3.14}$$

Knowing that the axial strain is given by $\varepsilon_z = \Delta L_z / L$ and using Eq. (3.6), the axial displacement is given by

$$\Delta L_z = \int_0^L \varepsilon(z)dz = \int_0^L \frac{F}{E_c A_c(z) + E_f A_f(z)} dz \tag{3.15}$$

where L is the original FBG length and F is the tension applied to the fiber.

In packaging, the FBG was mounted in the NTEC ceramic and there was no external tension applied to the fiber and ceramic. Thus, the axial displacement is determined by the temperature change of the NTEC ceramic according to

$$\Delta L_z = L\alpha_N \Delta T_N \tag{3.16}$$

where α_N (=-7.6×10^{-6}/°C) is the expansion coefficient of the NTEC ceramic and ΔT_N is the temperature change of the NTEC ceramic.

Using Eqs. (3.6), (3.15) and (3.16), the local strain change, $\Delta\varepsilon(z)$, relates to the temperature change of the NTEC ceramic, ΔT_N, as

$$\Delta\varepsilon(z) = \frac{L\alpha_N \Delta T_N}{\left[E_c A_c(z) + E_f A_f(z)\right] \cdot \int_0^L \frac{1}{E_c A_c(z) + E_f A_f(z)} dz} \tag{3.17}$$

For a linear strain gradient, the change in strain at the middle of FBG, $\Delta\varepsilon(L/2)$, is equal to the average strain change along the FBG length, $\overline{\Delta\varepsilon(z)}$, which can be expressed by the temperature change on the NTEC ceramic as

$$\Delta\varepsilon(L/2) = \overline{\Delta\varepsilon(z)} = \Delta L_z / L = \alpha_N \Delta T_N \tag{3.18}$$

Because $\Delta T \sim U^2/R$ where U is the applied voltage and R is the resistance, and the same voltage is applied to the conductive paint layer on the surface of the NTEC ceramic and the thin-film coating, and if one assumes that the temperature change of the NTEC ceramic, ΔT_N, and the temperature change of the FBG, $\Delta T(z)$, only depends on the resistances of the heaters deposited on its surface (i.e. there is no temperature exchange between the two heaters), the following equation is obtained

$$\frac{R_N}{R_c} = \frac{\Delta T(L/2)}{\Delta T_N} = -\alpha_N \frac{1-p_e}{\alpha+\xi} \tag{3.19}$$

where R_N is the resistance of the conductive paint layer and R_c is the resistance of the thin-film coating. This means that if the resistances of the conductive paint layer and the thin-film coating follow the relationship as given in Eq. (3.19), the left term in Eq. (3.12) would be equal to zero ($\Delta\lambda_B(L/2) = 0$), which means the center wavelength will be fixed when tuning the chirp and hence the dispersion.

3.3 Device Fabrication

The fabrication of this device involves several processes, which are FBG fabrication, controlled etching of fiber grating, metallization of fiber grating using e-beam evaporation technique, controlled electrical plating, mounting an FBG inside an NTEC ceramic, and metal coating on the outer conductive painting layer. This section presents these fabrication processes.

3.3.1 FBG Fabrication

A uniform FBG (25 mm long) was inscribed in a bare photosensitive fiber (PS-RMS-50, StockerYale Inc.) using the standard ultraviolet (UV) exposure technique with a phase mask whose period is 1065.7 nm. The corresponding central wavelength of the FBG is around 1546 nm.

3.3.2 Wet Etching to Obtain a Prescribed Diameter Profile of an FBG

An adjustable translation stage was used to dip the FBG into the hydrofluoric (HF) acid at a controlled rate to obtain a desired FBG diameter profile according to Eq. (3.10). Figure 3.7 shows the schematic setup for controlling the etching process.

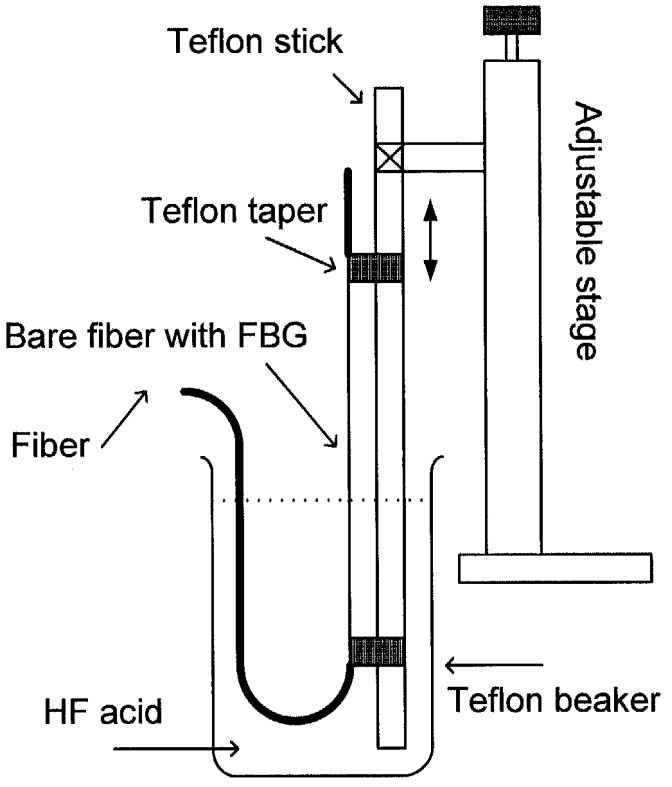

Figure 3.7 Schematic diagram of a wet etching setup used to obtain a prescribed diameter profile of an FBG.

The etching rate is linear with time and therefore any desired taper profile can be obtained by controlling the movement of the fiber [40]. The concentration of the HF acid used was ~49%, and the estimated etching rate for the bare

fiber is about 3.6 μm/min. The polymer jacket of the fiber and the Teflon taper were used to isolate the fiber outside the FBG area from the HF acid. After etching, the diameter of the fiber varied from ~90 μm to 125 μm along the FBG length. A microscope with a CCD camera connected was used to observe the surface of FBG and to roughly measure the diameter of FBG after etching. A photograph of the fiber profile after etching is shown in Fig. 3.8.

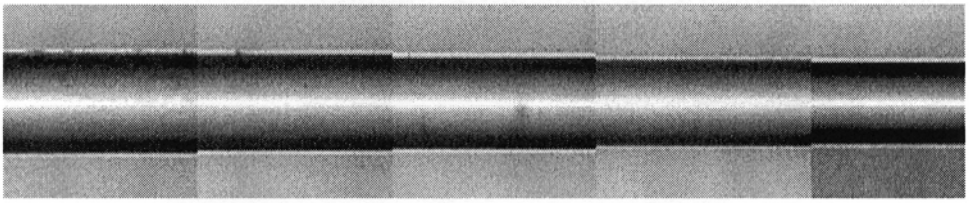

Figure 3.8 Photograph of a fiber profile after etching with diameter varying from ~90 μm to 125 μm.

3.3.3 Metallization of FBG

Before deposition of the on-fiber thin-film coating on the outer surface of the grating using electrochemical plating technique, the fiber should be metallized first to make conductive connection possible. The fiber with the FBG was mounted on a holder, which was fixed on the rotation platform of an electron beam evaporator. Ideally, the fiber should rotate axially in the electron beam chamber to enable uniform thin-film coating. Because of equipment limitation, metal was first deposited on one side of the fiber and then on the other side of the fiber. Using this kind of holder, it was quite easy to change the orientation of metallization on the fiber. Titanium (~200 Å as adhesion promoter) and gold (~2500 Å) were evaporated onto the entire outer surface of a stripped

section of the fiber with the grating. The non-uniformity of the titanium and gold coatings do not affect the performance of the device because the thicknesses of the titanium and gold are negligible compared to the 5 μm thickness of the copper coating on the outside.

3.3.4 Controlled Electrochemical Plating

Figure 3.9 shows the schematic diagram of a controllable electrochemical plating method. After etching and metallization, a thin film was deposited on the outer surface of the tapered and metallized fiber using a controllable electrochemical plating technique [29]. Using an adjustable translation stage, thin copper coating with a prescribed thickness profile, which is determined by Eq. (3.11), was deposited on the outer surface of the fiber by pulling the fiber from an electroplating bath with a controlled speed while plating at a constant rate with constant electrical current. The plating speed is given by $P \sim I/A_p$, where I is the plating current and A_p is the plating area. To ensure a constant plating speed, I and A_p must be constant.

A copper sheet with a large surface area was electrically connected to the fiber and dipped into the plating bath during the plating process. Thus, the change in the plating area when removing the fiber from the bath is negligible. With a plating current of 200 mA, the estimated thickness plating speed was 1.6 μm/min. After plating, the thickness of the thin-film coating varied from 1 μm

to 5 μm over the FBG range. The resistance of the final copper thin-film coating is $R_c \approx 4.0\ \Omega$.

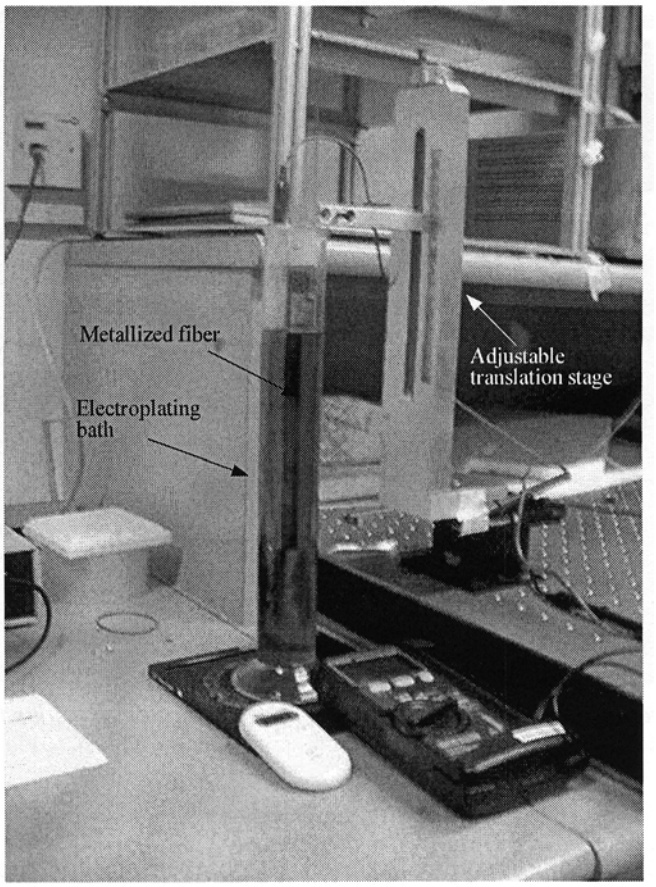

Figure 3.9 Photograph of the setup of a controllable electrochemical plating method.

3.3.5 Packaging of FBG

To fix the center wavelength during the tuning process, the fiber with FBG (with a taper thin-film coating on its surface) must be mounted inside the NTEC ceramic (3×3×50 mm, with 0.3×0.3 mm groove) under pre-tension, and this will shift the central wavelength to the longer wavelength side and will

introduce chirp to the uniform FBG. Figure 3.10 shows the setup for mounting the FBG in the NTEC ceramic under pre-tension.

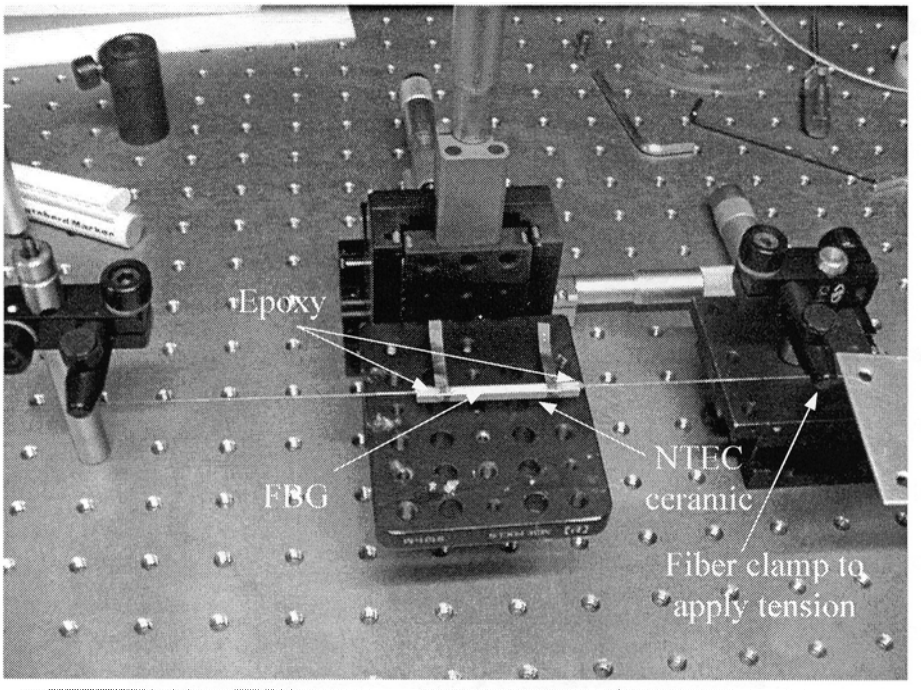

Figure 3.10 Mounting the FBG in a NTEC material under tension.

The NTEC material is typically used to compensate for the temperature sensitivity of FBG [41]. The NTEC material will shrink when being heated and will compress the FBG inside it to offset the shift of the Bragg wavelength due to the temperature rise. The thermal-expansion coefficient of the NTEC material is -7.6×10^{-6} /°C. Pre-tension was applied to the FBG to avoid bending of the fiber when the FBG was compressed by the shrinkage of the NTEC ceramic. An optical spectrum analyzer (OSA) was used to monitor the central wavelength shift and bandwidth broadening when applying the axial pre-tension to the FBG. The epoxy was trickled on both ends of the NTEC ceramic to fix the fiber with the NTEC ceramic. To ensure that the pre-tension

can be maintained on the FBG, the type of epoxy used is very important, which should be stable with a high temperature of up to 200 °C. Suitable epoxy recipe should be studied and optimized before the device can be practically used for commercial purpose. There was no additional tension on the fiber and the NTEC ceramic so the strain change on the fiber will depend only on the temperature change of the NTEC ceramic. After mounting the FBG inside the NTEC ceramic with epoxy, the central wavelength shifted from ~1546.4 nm to ~1550.0 nm while the 3-dB bandwidth changed from ~0.2 nm to ~1.2 nm (see Figure 3.11).

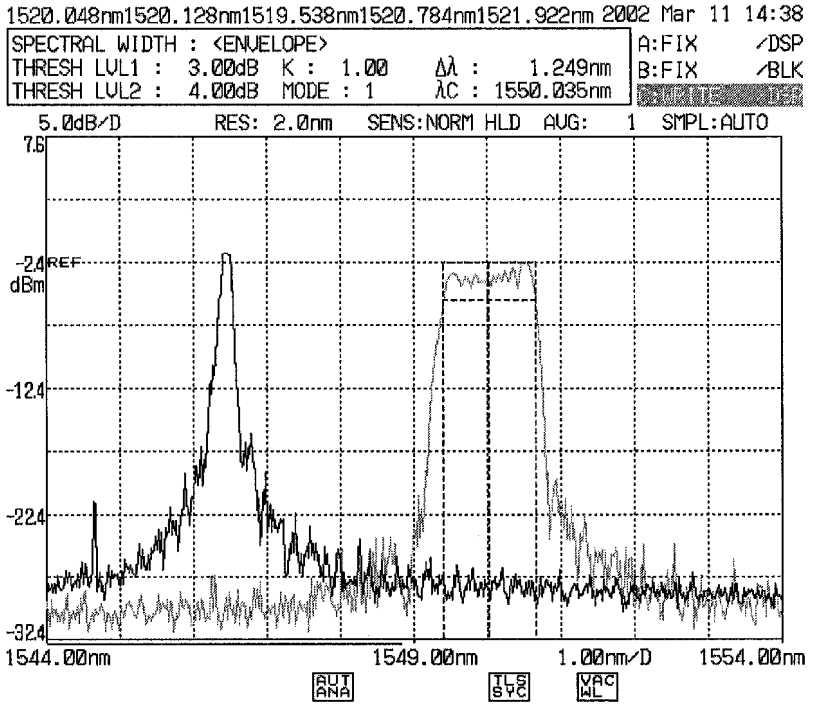

Figure 3.11 Shift in the reflection spectrum of FBG mounted inside the NTEC ceramic under tension. The reflection spectrum of FBG before packaging (black) and after packaging (gray) with pre-tension. The center wavelength was shifted by ~3.6 nm and the bandwidth was increased by ~1 nm.

3.3.6 Outer Conductive Layer

A layer of conductive paint was deposited on the surface of the NTEC ceramic, which is used to heat the NTEC ceramic when current flows through it. The resistance of the conductive paint layer is $R_N \approx 4.1\ \Omega$. Two copper sheets as electrodes were attached to the thin-film coating and the conductive paint layer on both ends of the NTEC ceramic with silver epoxy. Figure 3.12 shows the photograph of a packaged prototype of a tunable FBG dispersion compensator. To isolate the outside temperature fluctuation, this device can be further packaged using, for example, a heat resistive material.

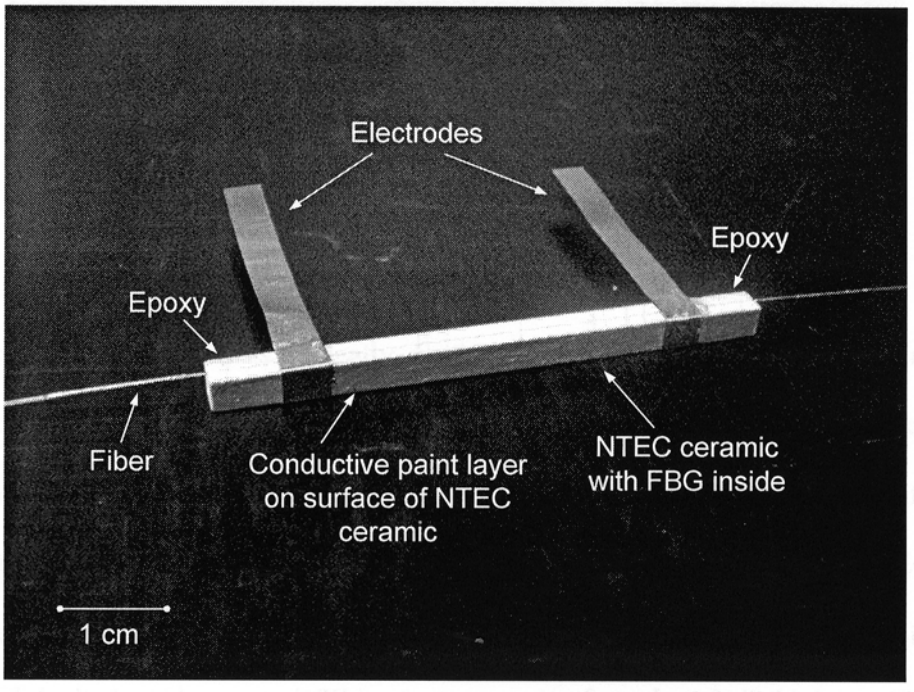

Figure 3.12 Photograph of a packaged tunable FBG dispersion compensator.

3.4 Dispersion Measurement Setup

The phase-shift method was used to measure the dispersion of this tunable dispersion compensator. The phase-shift method is an established technique for performing high-accuracy dispersion measurements. It has traditionally been used to determine the dispersion of an optical fiber, which can be derived from the differentiation of the measured group delay with wavelength. Nowadays, the method has also been employed for characterization of optical filters such as FBGs. The experimental setup is illustrated in Fig. 3.13.

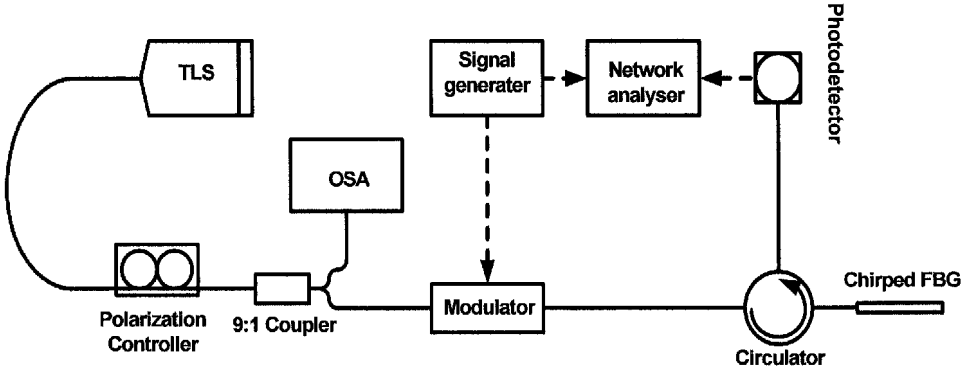

Figure 3.13 Schematic diagram of the experimental setup use to measure the dispersion of the tunable dispersion compensator using phase-shift method.

An electric signal generator was used to intensity modulate the output of a tunable laser source (TLS) by means of an external optical modulator. An OSA was used to monitor the wavelength of the output laser. After detecting the transmitted signal with a photodetector, a network analyzer was used to measure the phase of the detected signal relative to the electrical modulation source. The phase measurement was repeated at regular wavelength intervals, $\Delta\lambda$, across the spectral band of interest.

The relative group delay $\tau_{GD}(\lambda)$ of a signal component at the optical wavelength λ and the measured electrical phase shift $\phi(\lambda)$ of the intensity-modulated signal are related by the well-known equation

$$\tau_{GD}(\lambda) = \frac{\phi(\lambda)}{2\pi f_m} \tag{3.20}$$

where f_m is the modulation frequency of the electrical signal. And the dispersion can be expressed as

$$D = \frac{d\tau_{GD}(\lambda)}{d\lambda} = \frac{1}{2\pi f_m}\frac{d\phi(\lambda)}{d\lambda} \tag{3.21}$$

3.5 Experimental Results

Figure 3.14 shows the change in the reflection spectrum due to the current-induced shift of chirp in the tunable dispersion compensator. When the applied voltage was increased from 0 V to 1.2 V, the center wavelength was shifted by ~0.16 nm to the longer wavelength side and the reflection spectrum was narrowed by ~0.6 nm from about 1 nm. In this process, the chirp rate of the device changes from ~0.5 nm/cm to ~0.26 nm/cm. The central wavelength shift is probably due to the fact that the resistances of the conductive paint layer and the thin-film coating do not exactly match each other according to Eq. (3.19).

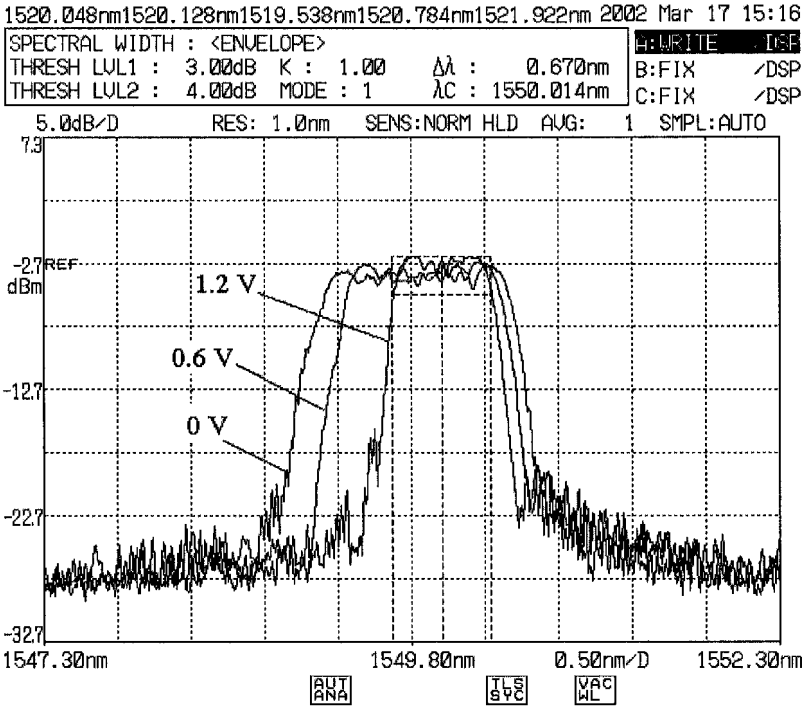

Figure 3.14 The spectrum of FBG changes under different applied voltages.

Figure 3.15 shows the central wavelength shift and the bandwidth change as a function of the applied voltage. When the applied voltage was raised from 0 V to 0.8 V, the central wavelength shifted by as small as 0.079 nm and the bandwidth was narrowed by up to 0.309 nm. When the applied voltage was reduced from 0.8 V to 0 V, the central wavelength shifted by as small as 0.066 nm and the bandwidth changed by up to 0.303 nm. Comparing with the bandwidth change, the central wavelength shift is relatively small when tuning the dispersion. It can be seen from Fig. 3.15 that there are no significant differences (< 0.01 nm) between the curves of ascending and descending voltages for both the bandwidth change and central wavelength shift, and this shows that the device has a small hysteresis. The small difference between

these two curves may be caused by the temperature fluctuation of the FBG and the NTEC material.

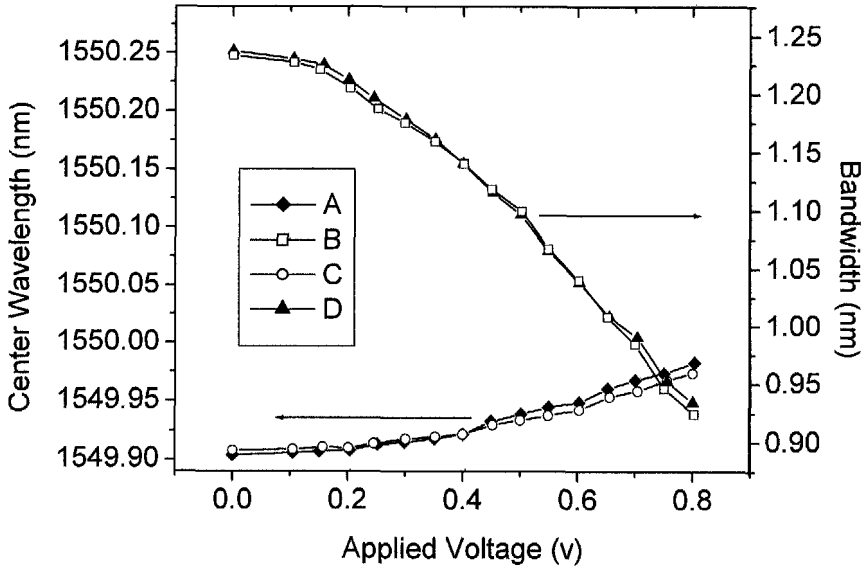

Figure 3.15 The central wavelength shift and the bandwidth change with the applied voltage. Curve A: Central wavelength shift when raising the voltage from 0 V to 0.8 V. Curve B: Bandwidth change when raising the voltage from 0 V to 0.8 V. Curve C: Central wavelength shift when reducing the voltage from 0.8 V to 0 V. Curve D: Bandwidth change when reducing the voltage from 0.8 V to 0 V.

For measuring the chromatic dispersion of the tunable dispersion compensator, the standard phase-shift method with a modulation frequency of 1.5 GHz was employed in the experiment. Figure 3.16 shows the group delay responses of the chirp grating under the applied voltages of 0 V, 0.4 V, 0.8 V and 1.2 V. The dispersion varies from –178 ps/nm to –302 ps/nm with an increase in the

applied voltage from 0 V to 1.2 V. The deviation of the group delay response from the linear fit (i.e. group delay ripple) has a maximum value of ~30 ps. This is normally due to imperfection in the production of the grating [42], [43]. But here the imperfection of the thin-film coating is the main reason for the group delay ripple and the ripple increases with the applied voltage. For the dispersion tuning range of –178 ps/nm to –302 ps/nm, the applied power was less than 0.68 W.

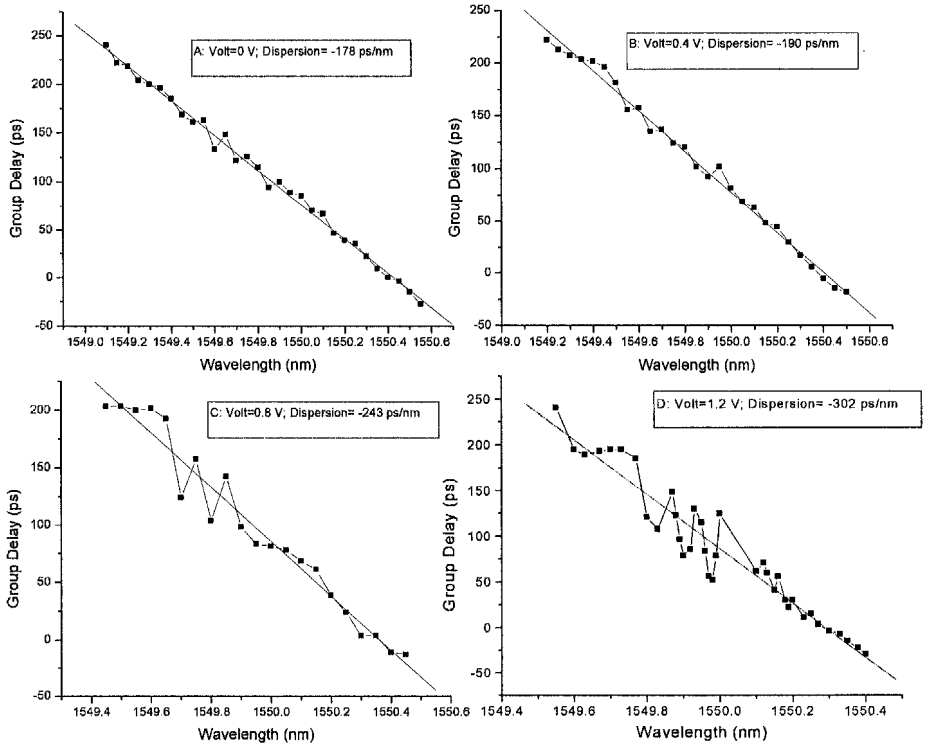

Figure 3.16 The dispersion varies from –178 ps/nm to –302 ps/nm with an increase in the applied voltage from 0 V to 1.2 V.

Figure 3.17 shows the simulation and experimental results of the center wavelength shift and the bandwidth change, and the two results agree

reasonably well with each other. In Fig. 3.17, the discrepancy between the simulation result and the experimental result of the bandwidth change as a function of the applied voltage is < 0.01 nm, and the discrepancy between the simulation result and the experimental result of the central wavelength change as a function of the applied voltage is < 0.001 nm. It should be noted that the dispersion value and the tuning range could be greatly increased by using a longer FBG. The tuning speed of this device depends on the temperature response time of the NTEC ceramic and is of the order of several seconds.

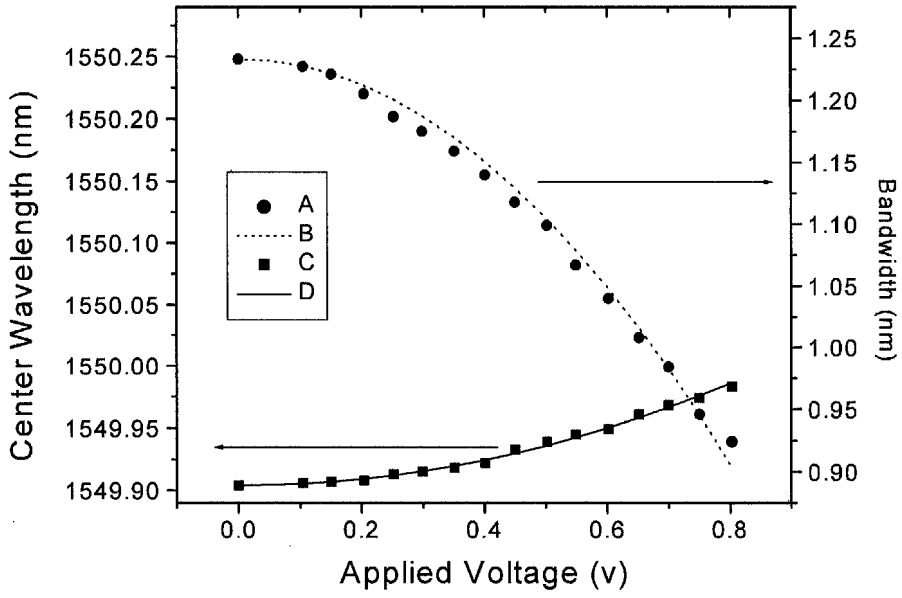

Figure 3.17 Comparison of the experimental results with the simulation results. Experimental result (curve A) and simulation result (curve B) of the bandwidth change versus the applied voltage. Experimental result (curve C) and simulation result (curve D) of the center wavelength shift versus the applied voltage.

3.6 Summary

A novel tunable dispersion-compensating filter based on FBG with almost-fixed central wavelength has been proposed and experimentally demonstrated. The dispersion varies from –178 ps/nm to –302 ps/nm with the center wavelength shift as little as 0.079 nm, and the group delay ripple is smaller than 30 ps. This device is based on the temperature sensitivity and strain sensitivity of FBG. This integrated device has many advantages, which include compact size, electrical tunability, almost-fixed central wavelength, low insertion loss, simple controllability, and power efficiency. It should be noted that the proposed technique can also be applied to multi-channel dispersion compensation by using a superstructure FBG. For multi-channel dispersion compensation, keeping the center wavelength fixed is much more important because the tolerance of the center wavelength shift must be much smaller than that in single-channel dispersion compensation to avoid crosstalk between the wavelength channels. It should be noted that with a proper design of the diameter profile of FBG and the thickness profile of the thin-film coating, this device can also be applied to higher-order dispersion compensation (such as dispersion slope compensation), which is an important issue in high-bit rate transmission systems.

3.7 References

[1] Gerd Keiser, *Optical Communications Essentials*, McGraw-Hill Networking Professional, 2003.

[2] A. Othonos and K. Kalli, *Fiber Bragg gratings: fundamentals and applications in telecommunications and sensing,* Artech House, 1999.

[3] G. P. Agrawal, *Nonlinear Fiber Optics (Third Edition)*, Academic Press, 2001.

[4] W. H. Hatton and M. Nishimura, "Temperature dependence of chromatic dispersion in single mode fibers," *IEEE J. Lightwave Technol.*, vol. LT-4, pp. 1552–1555, 1986.

[5] K. M. Feng, J. X. Cai, V. Grubsky, D. S. Starodubov, M. I. Hayee, S. Lee, X. Jiang, A. E. Aillner and J. Feinberg, "Dynamic dispersion compensation in a 10-Gb/s optical system using a novel voltage tuned nonlinearly chirped fiber Bragg grating," *IEEE Photon. Technol. Lett.*, vol. 11, pp. 373–375, 1999.

[6] N. Henmi, T. Saito and T. Ishida, "Prechirp technique as a linear dispersion compensation for ultrahigh-speed long-span intensity modulation direct detection optical communication systems" *IEEE J. Lightwave Technol.*, vol. 12, pp. 1706–1719, 1994.

[7] T. Saito, N. Henmi, S. Fujita, M. Yamaguchi and M. Shikada, "Prechirp technique for dispersion compensation for a high-speed long-span transmission" *IEEE Photon. Technol. Lett.*, vol. 3, pp. 74–76, 1991.

[8] T. L. Koch and R. C. Alferness, "Dispersion compensation by active predistorted signal synthesis," *IEEE J. Lightwave Technol.*, vol. 3, pp. 800–805, 1985.

[9] P. Spano, M. Tamburrini and S. Piazzolla, "Optical FSK modulation using injection-locked laser diodes" *IEEE J. Lightwave Technol.*, vol. 7, pp. 726–728, 1989.

[10] G. May, A Solheim and J. Conradi, "Extended 10 Gb/s fiber transmission distance at 1538 nm using a duobinary receiver," *IEEE Photon. Technol. Lett.*, vol. 6, pp. 648–650, 1994.

[11] N. A. Olsson, G. P. Agrawal and K. W. Wecht, "16 Gbit/s, 70 km pulse transmission by simultaneous dispersion and loss compensation with 1.5 μm optical amplifiers," *Electron. Lett.*, vol. 25, pp. 603–605, 1989.

[12] A. J. Antos and D. K. Smith, "Design and characterization of dispersion compensating fiber based on the LP_{01} mode," *IEEE J. Lightwave Technol.*, vol. 12, pp. 1739–1745, 1994.

[13] S. N. Knudsen, "Design and manufacture of dispersion compensating fibers and their performance in systems" Optical Fiber Communication Conference and Exhibit (OFC), pp. 330–332, 2002.

[14] J. Liu, Y. L. Lam, Y. C. Chan, Y. Zhou and J. Yao, "Fabrication of High-Performance Dispersion Compensating Fiber by Plasma Chemical Vapor Deposition," *Fiber Integ. Opt.*, vol. 18, pp. 63–67, 1999.

[15] L. Gruner-Nielsen, S. N. Knudsen, B. Edvold, T. Veng, D. Magnussen, C. C. Larsen and H. Damsgaard, "Dispersion Compensating Fibers," *Opt. Fiber Technol.*, vol. 6, pp. 164–180, 2000.

[16] T. Ozeki, "Optical equalizers", *Opt. Lett.*, vol. 17, pp. 375–377, 1992.

[17] K. Takiguchi, K. Okamoto, S. Suzuki and Y. Ohmori, "Planar lightwave circuit optical dispersion equalizer," *IEEE Photon. Technol. Lett.*, vol. 6, pp. 86–88, 1994.

[18] A. E. Willner, K.-M. Feng, S. Lee, J. Peng and H. Sun, "Tunable compensation of channel degrading effects using nonlinearly chirped passive fiber Bragg gratings," *IEEE J. Selected Topics in Quantum Electronics,* vol. 5, pp. 1298 –1311, 1999.

[19] B. J. Eggleton, J. A. Rogers, P. S. Westbrook and T. A. Strasser, "Electrically tunable power efficient dispersion compensating fiber Bragg grating," *IEEE Photon. Technol. Lett.*, vol. 11, pp. 854 –856, 1999.

[20] K. C. Byron, *et al.* "Fabrication of chirped Bragg gratings in photosensitive fiber," *Electron. Lett.*, vol. 29, pp. 1659–1660, 1993.

[21] K. Sugden, *et al.* "Chirped gratings produced in photosensitive optical fiber deformation during exposure," *Electron. Lett.*, vol. 30, pp. 440–441, 1994.

[22] Y. Painchaud, A. Chandonnet and J. Lauzon, "Chirped fiber gratings produced by tilting the fiber," *Electron. Lett.* vol. 31, pp. 171–172, 1995.

[23] M. A. Putnam, G. M. Williams, and E. J. Friebele, "Fabrication of tapered strain-gradient chirped fibre Bragg gratings," *Electron. Lett.* vol. 31, pp. 309–310, 1995.

[24] K. O Hill *et al.*, "chirped in-fiber Bragg grating for compensating of optical fiber dispersion," *Opt. Lett.*, vol. 19, pp. 1314–1316, 1994.

[25] R. Kashyap, P. F. McKee, R. J. Campbell and D. L. Williams, "A novel method of writing photo-induced chirped Bragg gratings in optical fibers," *Electron. Lett.,* vol. 12, pp. 996–997, 1994.

[26] R. Kashyap, *Fiber Bragg gratings,* Academic Press, 1999.

[27] J. Lauzon, S. Thibault, J. Martin and F. Ouellette, "Implementation and characterization of fiber Bragg gratings linearly chirped by a temperature-gradient," *Opt. Lett.,* vol. 19, pp. 2027 2029, 1994.

[28] Z. H. Chen, C. Lu, J. H. Ng, X. F. Yang and T. H. Cheng, "Tunable chirped fiber Bragg gratings by a distributed heater," *Opt. Eng. Lett.,* vol. 40, pp. 1156 1157, 2001.

[29] J. A. Rogers, B. J. Eggleton, J. R. Pedrazzani and T. A. Strasser, "Distributed on-fiber thin film heaters for Bragg grating with adjustable chirp," *Appl. Phys. Lett.,* vol. 74, pp. 3131 3133, 1999.

[30] P. C. Hill and B. J. Eggleton, "Strain gradient chirp of fiber Bragg grating," *Electron. Lett.,* vol. 30, pp. 1172 1174, 1994.

[31] M. Pacheco, A. Medez, L. A. Zenteni and F. Mendoz-Santoyo, "Chirping Optical fiber Bragg gratings using tapered-thickness piezoelectric ceramic," *Electron. Lett.,* vol. 34, pp. 2348 2350, 1998.

[32] Y. N. Zhu, P. L. Swart and B. M. Lacquet, "Chirp tuning of a fiber Bragg grating by using different tapered transducers and loading procedures: an application in the accelerometer," *Opt. Eng.*, vol. 40, pp. 2092 2096, 2001.

[33] T. Imai, T. Komukai and M. Nakazawa, "Dispersion tuning of a linearly chirped fiber Bragg grating without a center wavelength shift by applying a strain gradient," *IEEE Photon. Technol. Lett.*, vol. 10, pp. 845 847, 1998.

[34] Y. Q. Liu, J. P. Yao, X. Y. Dong, and J. L. Yang, "Tunable chirping of a fiber Bragg grating without center wavelength shift using a simply supported beam," *Opt. Eng.*, vol. 41, pp. 740 741, 2002.

[35] Y. W. Song, D. Starodubov, Z. Pan, Y. Xie, A. E. Willner, and J. Feinberg, "A tunable dispersion compensator with fixed bandwidth for WDM systems using a uniform FBG," *CLEO*, 2001.

[36] J. A. Rogers, B. J. Eggleton, R. J. Jackman, G. R. Kowach and T. A. Strasser, "Dual on-fiber thin film heaters for fiber gratings with independently adjustable chirp and wavelength," *Opt. Lett.*, vol. 24, pp. 1328 1330, 1999.

[37] H. G. Limberger, N. H. Ky, D. M. Costantini, R. P. Salathé, C. A. P. Muller and G. R. Fox, "Efficient miniature fiber-optic tunable filter based on intracore Bragg grating and electrically resistive coating," *IEEE Photon. Technol. Lett.*, vol. 10, pp. 361 363, 1998.

[38] A. Iocco, H. G. Limberger, R. P. Salathé, L. A. Everall, K. E. Chisholm, J. A. R. Williams and I. Bennion, "Bragg grating fast

tunable filter for wavelength division multiplexing," *IEEE J. Lightwave Technol,* vol. 17, pp. 1217 1221, 1999.

[39] J. A. Rogers, B. J. Eggleton and P. Kuo, "Temperature stabilized operation of tunable fiber grating devices that use distributed on-fiber thin film heaters," *Electron. Lett.,* vol. 35, pp. 2052 2053, 1999.

[40] L. Dong, J. L. Cruz, L. Reekie and J. A. Tucknott, "Fabrication of chirped fibre gratings using etched tapers," *Electron. Lett.,* vol. 31, pp 908 909, 1995.

[41] A. Richter, T. Andritschke, H. Bock, P. Leisching, D. Stoll, L. Quétel and S. Aguy, "Passive temperature compensation of piezo-tunable fiber Bragg gratings," *Electron. Lett.* vol. 35, pp. 1269 1271, 1999.

[42] R. Feced and M. N. Zervas, "Effects of random noise and amplitude errors in optical fiber Bragg gratings," *IEEE J. Lightwave Technol,,* vol. 18, pp. 90 100, 2000.

[43] S. J. Minailov, F. Bilodeau, K. O. Hill, D. C. Johnson, J. Albert, D. Stryckman and C. Shu, "Comparison of fiber Bragg grating dispersion-compensators made with holographic and e-beam written phase masks," *IEEE Photon. Technol. Lett.,* vol. 11, pp. 572 574, 1999.

4 All-Fiber Acousto-Optic Tunable Filter

4.1 Introduction

Acousto-optic (AO) devices can be used to adjust the optical characteristics of an AO medium using an acoustic method, which is based on the AO effect in the AO medium. The AO effect is also referred to as an elastic-optical effect, which is the effect on the characteristics of an optical wave in the presence of an acoustic wave or external force [1]. When an external force is applied to the AO material, the reflective index of the material will change. Thus, when an acoustic wave, which can be treated as a periodic internal strain, is applied to the AO material, a periodic reflective index variation is introduced into the material. This periodic reflective index variation can be treated as an artificial grating whose period is determined by the wavelength of the acoustic wave, and the refractive index modulation depth will depend on the strength of the acoustic wave [2].

4.1.1 Acousto-Optic Tunable Filter Using Acousto-Optic Waveguide

Many different devices can be fabricated based on the AO effect, such as AO modulator [3], acousto-optic tunable filter (AOTF) [4], AO polarization converter [5] and AO frequency shifter [6]. In these components, AOTF is a very useful device for application in wavelength division multiplexing (WDM) systems because the AOTF can be used to select information of one particular wavelength channel from all the other background WDM channels.

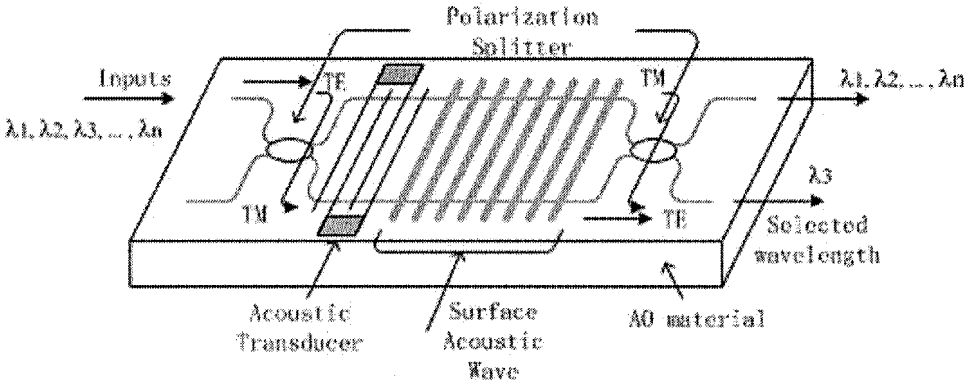

Figure 4.1 Schematic diagram of an AOTF based on optical waveguide technology.

Figure 4.1 shows the schematic diagram of a typical AOTF based on optical waveguide technology. The AOTF consists of an AO material substrate, an acoustic transducer, and two polarizers. When the light wave is transmitted through the AO medium in the presence of an applied acoustic wave, the light wave of a particular wavelength that matches the phase-matching condition is perfectly changed to the orthogonal polarization state. Using two polarizers,

the light wave of a particular wavelength that matches the phase-matching condition can be selected from the background of the light waves of other wavelengths.

The phase-matching condition can be expressed as [7]

$$\left|n_{eff}^{TE} - n_{eff}^{TM}\right| / \lambda_0 = f_a / v_a \qquad \textbf{(4.1)}$$

where f_a and v_a are the frequency and velocity of the surface acoustic wave (SAW), respectively, n_{eff}^{TE} and n_{eff}^{TM} are the effective indices of the *TE* and *TM* polarized optical modes respectively, and λ_0 is the optical wavelength. When the frequency of the SAW changes, the optical wavelength of the optical wave to be phase-matched is varied. This is the basic principle of AOTF. For wavelengths in the C-band (1525–1565 nm) of the third communication window, the SAW frequency for phase-matching in $LiNbO_3$ is around 170 MHz with a tuning slope of ~8 nm/MHz [7].

The advantages of the AOTF technology include [8]:

- Broad tuning range (1200 nm to 1600 nm). Due to the ease of modifying the properties of the acoustic wave (e.g. frequency and voltage), the optical wavelength can be selected from within a very large tuning range.
- High tuning speed of the order of microseconds. The tuning speed of AOTF depends on the time it takes for SAW traveling through the interaction region. It is much faster than many other methods using mechanical or thermal tuning techniques.

- Ability to switch multiple channels simultaneously. When superimposing multiple SAWs with different frequencies together, the AOTF can be used to select multiple optical wavelengths.

However, the AOTF based on the waveguide technology also suffers from several disadvantages, which include high insertion loss (~ 5 dB), strong sidelobes of the transfer function that could degrade the filtering efficiency, polarization sensitivity, and unwanted frequency shift due to the Doppler effect in the AO device. Furthermore, the bandwidth of an AOTF is not very narrow. Although the insertion loss can be reduced to ~ 4.1 dB [9] and improved structural design can provide strong sidelobe suppression and low polarization dependence [10], most of these problems still need to be solved or improved before the AOTF can be widely used in WDM systems for future dynamic network applications.

4.1.3 All-Fiber Acousto-Optic Tunable Filter

In 1997, an all-fiber AOTF was demonstrated by Kim *et al.* [11]. The single-mode fiber (SMF) based AOTF causes mode coupling of light that satisfies the phase matching condition from the fundamental mode (LP_{01}) to several low-order cladding modes (LP_{11}, LP_{12}). This mode coupling is mainly induced by the periodic refractive index perturbation along the fiber, which is caused by the propagation of an acoustic wave in the fiber. An optical wave at a particular wavelength, which is coupled from the fiber core to the cladding, will be coupled out of the fiber. As a result, an all-fiber AOTF acts as a notch

filter, which can be used to filter out a lightwave of a particular wavelength from the background wavelengths. Comparing to waveguide based AOTF, the all-fiber AOTF has low insertion loss and can avoid the complicated alignment process in fabrication. A typical application of the all-fiber AOTF is as a dynamic gain equalizer of optical amplifiers [12].

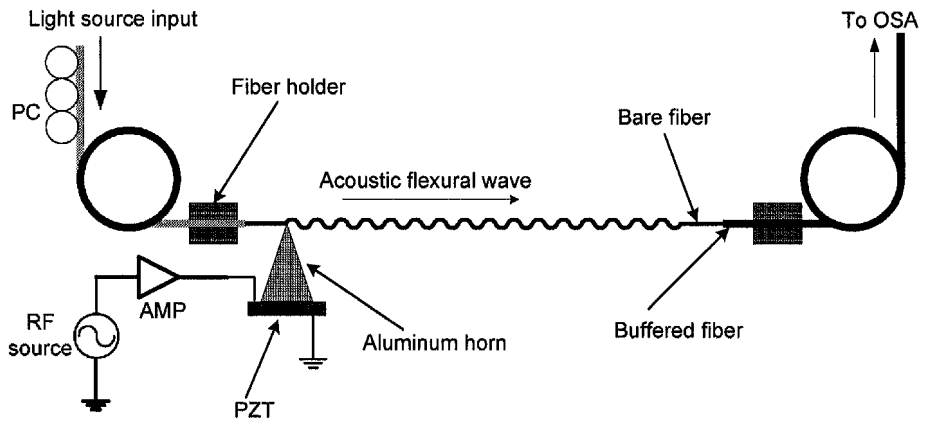

Figure 4.2 Experimental setup of an all-fiber AOTF.

A typical experimental setup of an all-fiber AOTF is shown in Fig. 4.2. In this setup, the acoustic wave is generated by applying a radio frequency (RF) signal to a piezo-electric transducer (PZT). A silica horn is attached to the PZT using epoxy, and hence the acoustic wave generated by the PZT will be amplified and concentrated at the tip of the silica horn, and is then coupled into the SMF. The dimension of the tip of the silica horn is about the same as the fiber diameter to achieve high acoustic coupling efficiency. Using epoxy to permanently align the tip of the silica horn to the bare SMF, the acoustic wave can be coupled into the silica fiber and will propagate in the fiber. When the optical wave transmits through the fiber region, where there is acoustic wave, the coupling between the core mode and cladding modes will take place at the

phase matching condition, and hence a notch filtering characteristic can be formed.

The acoustic wave in the fiber introduces the variation of stress and strain into the fiber. And the periodic variation of the strain and stress will change the optical properties of the material through the change in refractive index. This perturbation will cause coupling of an input symmetric fundamental mode to an asymmetric cladding mode. The coupled light will then be exhausted in the cladding [13]. The fiber with the acoustic wave functions in a similar manner to a temporary long period grating. This grating couples light of certain optical wavelength into the cladding where it is lost. Thus, the fiber based AOTF functions as a notch filter.

4.2 Design Principle of an All-Fiber AOTF

In this section, the design principle of PZT, aluminum horn and the coupling mechanism of light will be discussed. The AO coupling efficiency and the phase-matching condition in the AO resonance will also be analyzed. A theoretical model to determine the bandwidth of the all-fiber AOTF will also be presented.

4.2.1 Transduction and Excitation

As discussed earlier, the acoustic wave is generated by the PZT, concentrated by the horn and coupled into the SMF by gluing the tip of the horn with the

SMF. Assuming a symmetrical horn shape, surface-wave-like acoustic modes are required to be excited at the wider end of the horn, and thus a hollow horn or edge-banded transducers can be used to achieve this [14].

Although a solid horn was used in the experiment (see Fig. 4.2) and this transduction was not optimized, the effect at the thicker end of the solid horn is similar to that of applying edge-bonded transducers or using hollow horn for surface wave excitation. It has been proven experimentally that this transduction is sufficiently strong to excite the AO coupling.

Because the diameter of the PZT is much larger than that of the fiber, the acoustic mode pattern excited at the larger end of the horn are much more complicated than the acoustic mode propagating in the fiber, which is typically only a single acoustic mode. The other acoustic modes, which are excited at the larger end of the horn or created due to mode conversion in the horn, cannot be coupled into the SMF. As a result, a good design of the horn is very important to suppress the high-order acoustic modes from propagating through the horn.

One possible way to analyze the transmission of acoustic power in the horn is to use mode expansion theory and by dividing the horn into short cylindrical parts with varying diameter to approximate the desired horn profile. Such analysis has been performed as presented in reference [15]. A horn with a gradually varying radius, a, will transform the acoustic modes of a larger

diameter section into modes of the smaller diameter section at the tip of the horn. If this tapering is sufficiently gradual, the mode conversion will take place without noticeable loss.

From the above, an ideal design of the PZT is a ring shape to excite the surface-wave-like acoustic modes into the horn. Furthermore, the hollow horn is more suitable than the solid horn to simplify the acoustic mode pattern at the wider end, which can avoid high loss in mode conversion. Finally, a horn with longer length and slowly varying diameter is highly desirable for this application. Although an optimum design of the horn is highly desirable, our laboratory does not have the necessary facility to fabricate the optimally designed horn. With a simple design of the horn, the author has determined experimentally (see Section 4.4) that the acoustic power coupled to the SMF is sufficient to excite the desired AO effect within the fiber. The optimization of the horn design could be an objective for future work.

4.2.2 Coupling Efficiency

The acousto-optic coupling coefficient in the single-mode fiber can be expressed as [16]

$$\kappa_0 = \frac{\pi}{\lambda}\sqrt{\frac{\varepsilon_0}{\mu_0}}n_0 \int_A \psi_1(x,y)\Delta n(x,y)\psi_2(x,y)dx\ dy \qquad \textbf{(4.2)}$$

where n_0 is the refractive index of the single-mode fiber, λ is the central wavelength of the filter, ε_0 and μ_0 are the dielectric coefficient and magneto-electric coefficient, respectively, $\Delta n(x,y)$ is the depth of the refractive index

modulation caused by the acoustic wave, and $\psi_1(x,y)$ and $\psi_2(x,y)$ are the field distributions of the core and cladding modes, respectively. The coupling coefficient is proportional to the spatial overlap of the core and cladding modes and $\Delta n(x,y)$, which is proportional to the amplitude of the acoustic wave and the photo-elastic coefficient of the fiber [16].

Equation (4.2) helps to provide a better understanding of the coupling efficiency of the AO induced mode coupling. To enhance the coupling efficiency, one can reduce the diameter of the fiber and/or increase the interaction length. The accumulated AO coupling will be enhanced with an increase in the interaction length. By reducing the fiber cladding diameter through tapering or etching, the overlap of optical fields is enhanced, which also increases the coupling efficiency. In addition, the amplitude of the acoustic wave is also enlarged due to tighter confinement.

By assuming uniform distributions of acoustic energy over the entire cross section of both etched and unetched sections of the fiber and neglecting the coupling loss at the interface, it can be shown that the amplitude of the flexural acoustic is enhanced by a factor of $(D_1/D_2)^{1.25}$ [17], where D_1 and D_2 are the diameters of unetched and etched sections of the fiber. However, the tapered fiber requires special tools to fabricate it, and it is difficult to achieve uniform fiber tapering over a long distance. Comparing with the tapering technique, the fabrication process of chemical etching is much simpler and a uniform etched fiber with a longer length can be relatively easily

achieved. When the fiber diameter D is greater than 20 μm, the propagating characteristics of the core mode has been observed to be essentially unchanged, which ensures low insertion loss at the interfaces of the etched and unetched sections of the SMF [16]. Even though 20 μm is relatively large comparing with the diameter of the core of SMF (9 μm), etching the fiber diameter from 125 μm to 20 μm may have already damaged the core due to the non-uniformity of the fiber cross-section and possible scratches on the fiber surface after the fibre coating is mechanically stripped off. In the experiment, no signal can be received after the fiber was etched to a diameter of 20 μm.

The general theory for single-mode fiber that assumes infinite cladding is no longer suitable for an etched fiber when the outer diameter is small. Thus a doubly clad theory has to be used to describe the AO interaction in an etched fiber [18]. The doubly clad theory hypothesizes that the fiber consists of a core, a limited fiber cladding as the inner cladding, and then a boundless air layer that is enclosed out of the fiber as the outer cladding. Since the cladding mode propagates in this composite multiple waveguide, it is difficult to obtain an analytical solution. Numerical computation is thus used for studying the modes in the fiber as presented by reference [19].

4.2.3 Phase-Matching Condition

In the earlier section, it has been described that the acoustic wave would introduce a periodic refractive index perturbation along the fiber, and this

results in the coupling of the input fundamental mode to the cladding modes where light is then lost into the cladding. This phenomenon only takes place when the phase matching condition is satisfied.

The phase matching condition is satisfied when the acoustic wavelength is equal to the beat length between the fundamental and cladding modes. For a given acoustic frequency, the coupling between the fundamental and cladding modes takes place for a particular optical wavelength since the beat length has considerable wavelength dispersion [11].

The beat length between the two modes is expressed as

$$L_B = \frac{2\pi}{(\beta_{core} - \beta_{cladding})} \tag{4.3}$$

where β_{core} and $\beta_{cladding}$ are the propagation constants for the core mode and resonant cladding mode respectively [20].

The acoustic wavelength Λ of the flexural acoustic wave is expressed as [21]

$$\Lambda \equiv \frac{2\pi}{\kappa} = \left[\frac{\pi b C_{ext}}{f}\right]^{\frac{1}{2}} \tag{4.4}$$

where κ is the acoustic wave constant, b is the radius of the fiber diameter, C_{ext} is the speed of acoustic waves, which is 5760 m/s for silica, and f is the frequency of the flexural acoustic wave, which is the same as the frequency of the electrical signal driving the PZT.

Thus, at the phase matching condition, $L_B = \Lambda$, by rearranging Eq. (4.3) and Eq. (4.4), the frequency of the flexural acoustic wave is given by

$$f = \frac{\pi b C_{ext}}{L_B^2} = \frac{\pi b C_{ext}}{\Lambda^2} \tag{4.5}$$

In this equation, the optical wavelength λ is actually hidden in L_B. From this equation, one can calculate the value of the acoustic frequency for a particular beat length L_B that would give the phase matching condition for that optical wavelength. Thus, the position of the notch can be determined simply by changing the frequency f of the electrical signal applied to the transducer. As a result, a tunable notch filter can be developed based on this principle.

4.2.4 Bandwidth of All-Fiber AOTF

For a given acoustic frequency and an optical center wavelength, the 3-dB bandwidth of an all-fiber AOTF can be expressed as [14]

$$\sigma_\lambda = \frac{0.8\pi}{L\left(\frac{\partial \beta_{01}}{\partial \lambda} - \frac{\partial \beta_{1n}}{\partial \lambda}\right)} \tag{4.6}$$

where λ is the wavelength of the light, L is the length of the coupling region, β_{01} and β_{1n} are the propagation constants of the core mode and the cladding mode, respectively.

To simplify the equation, one can express σ_λ in terms of the beat length L_B between the core and cladding modes and a dimensionless parameter N as

$$\sigma_\lambda = \frac{0.8L_B}{L}\frac{1}{N}\lambda \tag{4.7}$$

where N is given by

$$N = \frac{\partial L_B}{\partial \lambda} \Big/ \frac{L_B}{\lambda} \tag{4.8}$$

which is related to the dispersion features of the fiber and the beat length L_B is the same as that defined in the previous section [19].

Using the above equations, the bandwidth of the AOTF varies with the interaction length L, and this is also observed in the experiment (as described below in Section 4.3) to investigate the effect of the interaction length on the performance of the filter.

4.3 Experimental Setup

This section presents the experimental development of an AOTF.

4.3.1 Development of All-Fiber AOTF

Figure 4.2 shows the configuration of an all-fiber AOTF, which consists of a SMF, a piezoelectric transducer (PZT), an aluminum horn, a signal generator and an RF amplifier. The frequency range of the amplifier is from 5 MHz to 500 MHz and the peak gain is 29 dB at a frequency of 300 MHz. The RF signal generated from the signal generator is amplified by the RF amplifier before it is applied to the PZT. The amplified RF signal induces a high-frequency vibration in the PZT due to the piezoelectric effect. The acoustic

wave generated by the high-frequency vibration is focused on the tip of the aluminum horn. By splicing the tip of the horn with the bare SMF, the acoustic wave can be coupled into the SMF and be transmitted in the SMF to form an all-fiber AOTF inside the SMF. The frequencies of the PZT used range from 2 MHz to 5 MHz. The diameter of the PZT disk is about 10 mm.

In the setup, an aluminum horn was used to concentrate the acoustic wave generated by the PZT, which can increase the coupling efficiency of the acoustic wave into the SMF. Ideally, the horn should be fabricated with silica because a high coupling efficiency and a low acoustic reflection can be achieved when the acoustic wave is coupled into the SMF through the horn. However, fabrication of the silica horn is difficult. Hence, in this investigation, horns made of aluminum were used because the Young's module of aluminum is very close to that of the silica, which can result in a low acoustic reflection and high coupling efficiency.

The bare SMF was fixed on a 3-D stage set to avoid external strain or vibration. The 3-D stage can be used to apply tension to the fiber and avoiding external strain as well as to align the fiber with the tip of the aluminum horn. To bond the horn to the tip of the fiber, an ultraviolet (UV) curing epoxy was used, which was then cured using an UV light source. A very small drop of UV epoxy was applied to the point of contact of the tip of the horn and the fiber, and was cured using UV light at an intensity of

approximately 4800 mW/cm^2 for one minute. With this method, the fiber was securely bonded to the horn.

An all-fiber AOTF using SMF with different diameter has been developed to study the effect of the fiber diameter on the performance of the AOTF. The various fiber diameters can be obtained using the chemical etching method. The chemical etching of the optical fiber was carried out using hydrofluoric (HF) acid of 49% concentration. The etching process has been described in Chapter 3. With a small fiber diameter, the etched portion was very fragile and extreme care was required when setting up the experiment using the etched fiber.

4.3.2 Testing Platform

A tunable laser source was used to provide an input light for testing the spectral responses of the all-fiber AOTF, which were measured using an optical spectrum analyzer (OSA). The RF signal generated by the signal generator and the signal applied to the PZT were monitored using an oscilloscope.

The frequency of the RF signal applied to the PZT was varied to investigate the performance of the AOTF. The actual frequency range depends mainly on the cladding diameter of the fiber used in the filter. The frequency was varied in steps of 10 kHz from 1.6 MHz to 2.4 MHz. The results obtained are discussed in the following section.

4.4 Experimental Results of an All-Fiber AOTF

In this section, the results and observations obtained from the experiments are presented. From the results, certain parameters such as polarization of the input light, interaction length, fiber diameter and the frequency and voltage of the RF signal applied to the PZT will be investigated to study their effects on the performance of the filter.

4.4.1 Effects of Polarization of the Input Light

Using a polarization controller (PC) in the experimental setup, the polarization of the input light was varied to study its effect on the performance of the filter. Figure 4.3(a) shows the notch obtained when an RF signal with frequency of 1.91 MHz and peak-to-peak voltage of 30 V was applied to the PZT. The PZT connected to the SM fiber with interaction length of 10 cm and diameter of 125 μm with an aluminum horn. Since the light from the tunable laser source was unpolarized, it can be seen that the fundamental mode in the core was coupled to different cladding polarization modes, which correspond to different wavelengths to satisfy the phase-matching condition. As a result, the spectral response of the filter (see Fig. 4.3(a)) can be obtained.

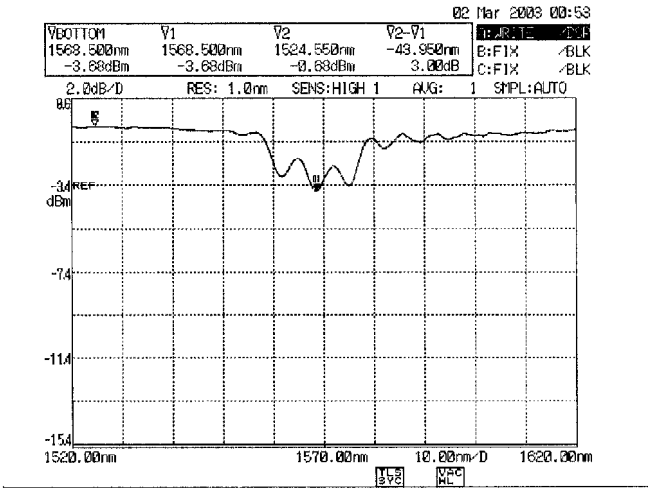

(a)

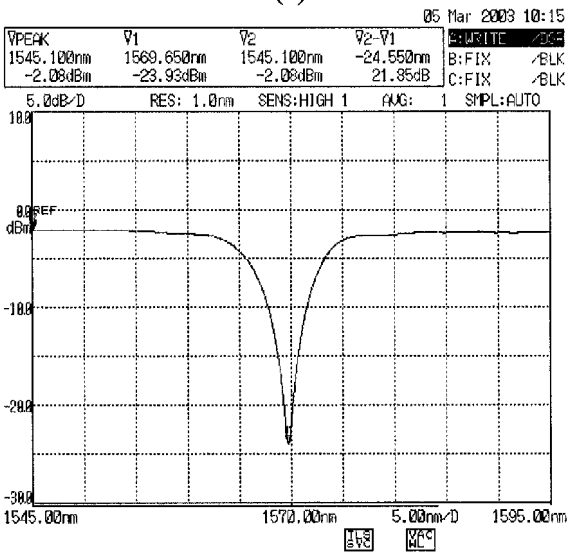

(b)

Figure 4.3 Measured spectrum of all-fiber AOTF with interaction length of 10 cm, fiber diameter of 125 μm, RF frequency of 1.91 MHz, and RF peak-to-peak voltage of 30 V. (a) With unpolarized input light; (b) with polarized input light.

From Fig. 4.3(a), there are three different notches, with each representing a different polarization mode in the cladding. Using the polarization controller,

the polarization of the input light was changed to suppress some of the modes while enhancing others. This effect can be seen in Fig. 4.3(b), which shows only one notch was observed using the polarization controller (PC) to suppress the side polarization modes. The other experimental conditions are unchanged.

From the observations above, one can conclude that polarization of light does indeed play a very important part in modifying the filter characteristics. Unfortunately, there are no appropriate instruments in the laboratory to identify the different types of modes and further investigation is thus needed. In addition, the PC employed was a manual one. Therefore, there was no means to precisely determine the polarization state of the input light.

4.4.2 Effects of Interaction Length

In testing the effects of the fiber interaction length on the performance of the filter, the unetched fibers with different lengths of bare fiber sections were used to develop the all-fiber AOTF. Here the interaction length is defined as the section of the fiber with its plastic coating stripped, in which the acoustic wave can propagate with low attenuation. Acoustic absorbers were also placed on both ends of the bare fiber to further confine the acousto-optic interaction in the bare fiber section.

Five tests were carried out to verify the effects of interaction length on the filter performance. The different interaction lengths tested vary from 60 cm to 100 cm at an interval of 10 cm. The fiber diameter was kept unchanged at 125

μm. For each interaction length, the RF signal with frequency of 2210 kHz and peak-to-peak voltage of 30 V was used to analyze the filter performance. Comparing the results obtained with different interaction lengths, Fig. 4.4 shows that the depth of the notch filter increases with an increase in the interaction length.

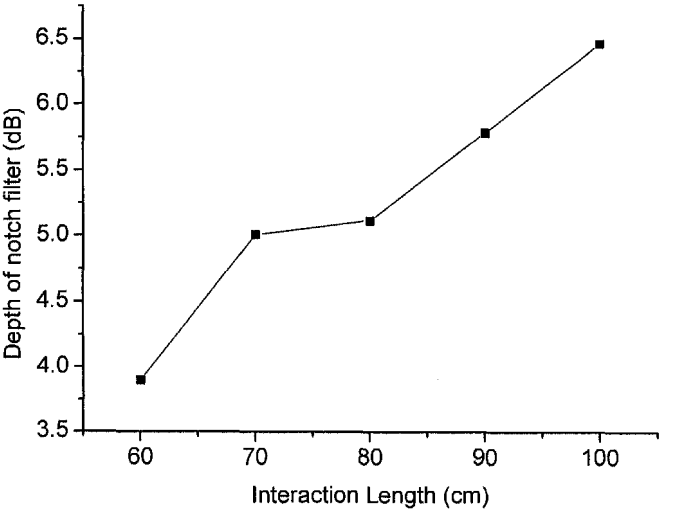

(a)

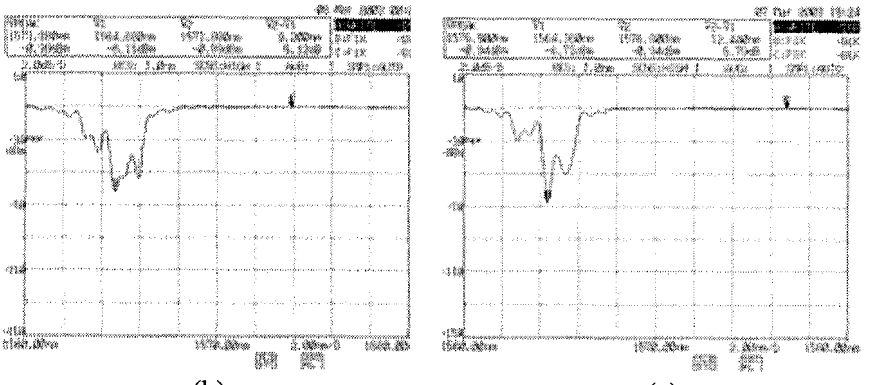

(b) (c)

Figure 4.4 (a) The depth of the notch filter increases with the interaction length. The RF signal has a frequency of 2.21 MHz and a peak-to-peak voltage of 30 V); (c) The spectra of AOTFs with interaction length of 80 μm and (c) 90 μm.

4.4.3 Effects of Fiber Cladding Diameter

With the reduction in the fiber cladding diameter, it has been found that there was a significant change in the performance of the filter as described here. Among the changes observed were wider bandwidth, deeper notches, and a shift in the center wavelength of the notch. The diameter of the fiber was reduced with chemical etching technique using hydrofluoric (HF) acid as described in Chapter 3. The results of the effect on the filter characteristic are shown in Fig 4.5 and 4.6.

The first significant effect of using a reduced fiber cladding diameter was the shift of the center wavelength of the notch although the frequency of the acoustic wave remained unchanged. The center wavelength of the notch shift towards the shorter wavelength side. Figure 4.5(a) shows the position of the notch for a fiber diameter of 90 μm while Fig. 4.5(b) shows the position of the notch for a fiber diameter of 72.5 μm. The interaction lengths were 10 cm for both cases. The acoustic frequency was 1.77 MHz and the peak-to-peak voltage of the RF signal was 30 V for both cases. It can be observed in Fig. 4.5 that the center wavelength shifted downwards from 1608.95 nm to 1586.8 nm with a reduction in fiber diameter from 90 μm to 72.5 μm.

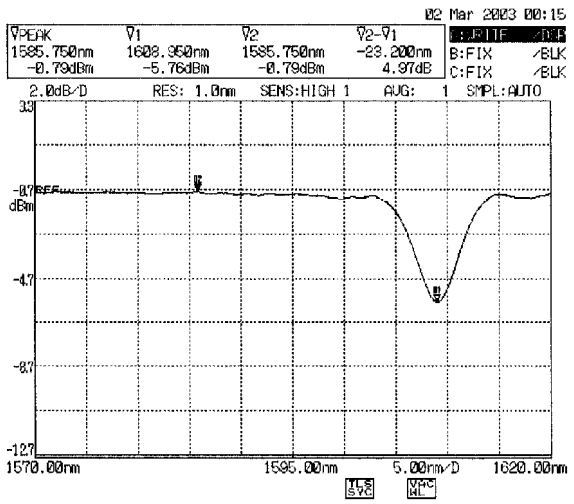

(a)

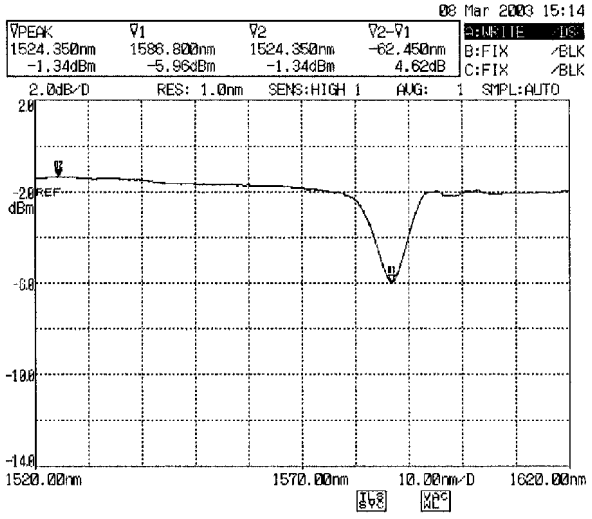

(b)

Figure 4.5 Variation of the central wavelength from (a) 1608.95 nm to (b) 1586.8 nm with a change in the fiber diameter of (a) 90 μm, (b) 72.5μm. The interaction length is 10 cm, the frequency of the RF signal is 1.77 MHz, and the peak-to-peak voltage of the RF signal is 30 V for both cases.

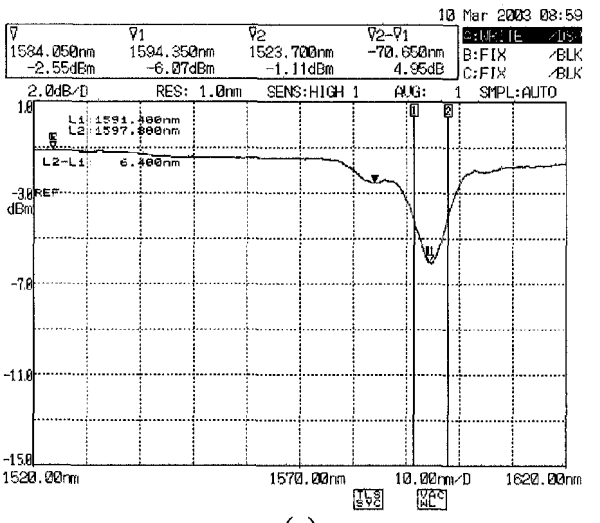

(a)

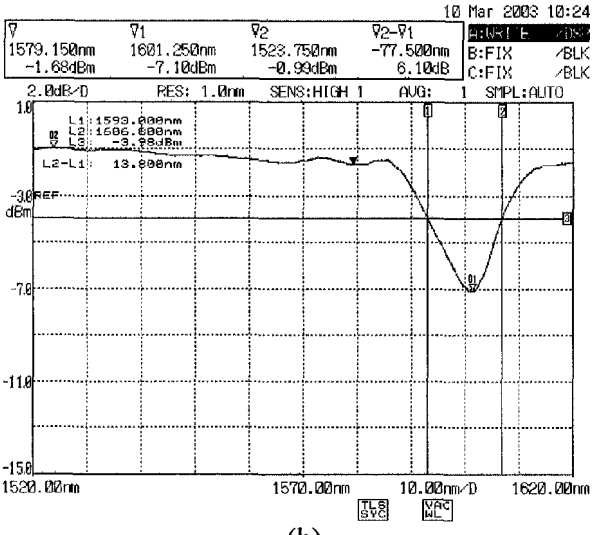

(b)

Figure 4.6 The filter bandwidth change with a change in the fiber diameter; (a) 3-dB bandwidth of 6.4 nm with fiber diameter of 72.5 μm; (b) 3-dB bandwidth of 13.8 nm with fiber diameter of 55μm.

The second significant effect of using a reduced fiber cladding diameter was the widening of the bandwidth. As the fiber cladding diameter was reduced, the bandwidth of the notch increases. Figure 4.6(a) and Figure 4.6(b) illustrate this point. Both results were obtained at an acoustic frequency of 1.74 MHz, a

peak-to-peak voltage of the RF signal of 30 V, and an interaction length of 10 cm. The bandwidth of the notch of a fiber diameter of 72.5 μm was 6.4 nm while the bandwidth of the notch of a fiber diameter of 55 μm was 13.8 nm.

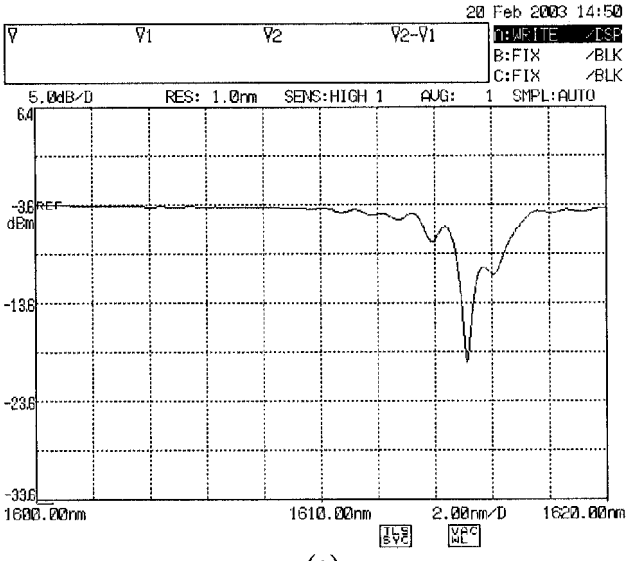

(a)

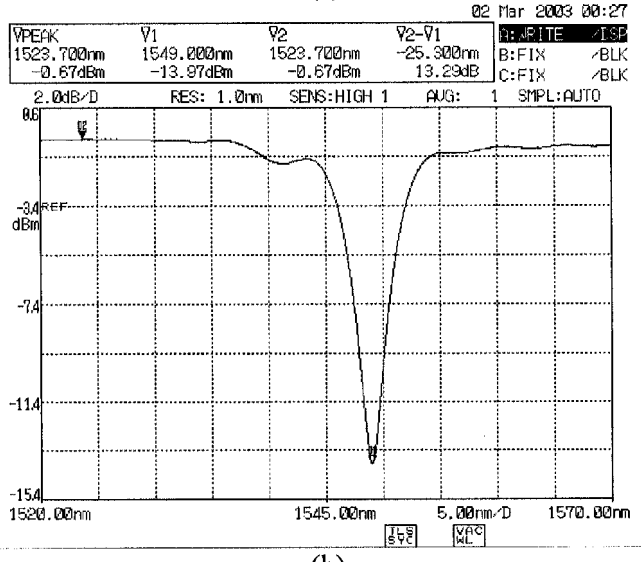

(b)

Figure 4.7 To achieve the same notch depth, different interaction lengths were needed with different fiber diameters; (a) 60 cm unetched fiber; (b) 10 cm etched fiber with diameter of 90 μm.

The third effect is the reduction in the required interaction length of the fiber to achieve a given depth of notch. For an unetched fiber with a diameter of 125 μm, an interaction length of almost six times that of an etched fiber cladding diameter of 90 μm was needed to obtain the same depth of the notch. Figure 4.7(a) and Figure 4.7(b) show that an interaction length of almost 60 cm was needed for the unetched fiber in order to achieve a similar notch depth as that of an etched fiber with a cladding diameter of 90 μm using only a 10 cm interaction length.

The main reason for this observation is that a smaller fiber cladding diameter increases the coupling efficiency of the acoustic wave into the fiber due to the overlap of optical fields being enhanced and the amplitude of the acoustic wave also being enhanced because of tighter confinement [16]. Thus, a notch of similar depth could be obtained even though a much shorter interaction length was used for the etched fiber.

Finally, as the fiber diameter decreases, the slope of the center wavelength to the acoustic frequency increases, and this is illustrated in Fig. 4.8.

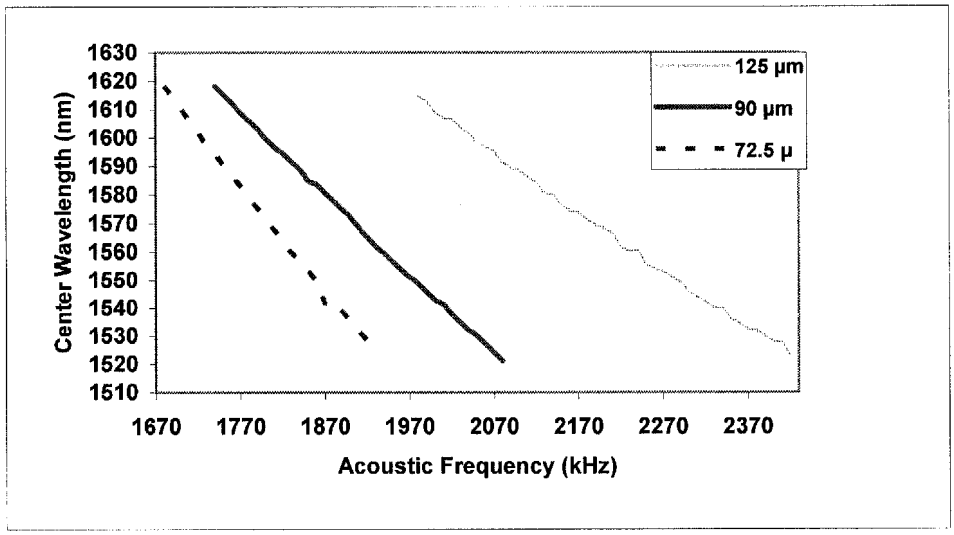

Figure 4.8 Change in the tuning slope with the fiber diameter (AOTF with interaction length of 10 cm and diameter of 90 µm).

4.4.4 Effects of Acoustic Frequency and Voltage

The all-fiber AOTF is based on the coupling of an input fundamental mode to the cladding modes through the periodic refractive index perturbation along the fiber caused by an acoustic wave, and this coupling mechanism results in a notch filter. By changing the frequency and voltage of the electrical signal applied to the PZT, the position of the notch as well as its depth can be varied.

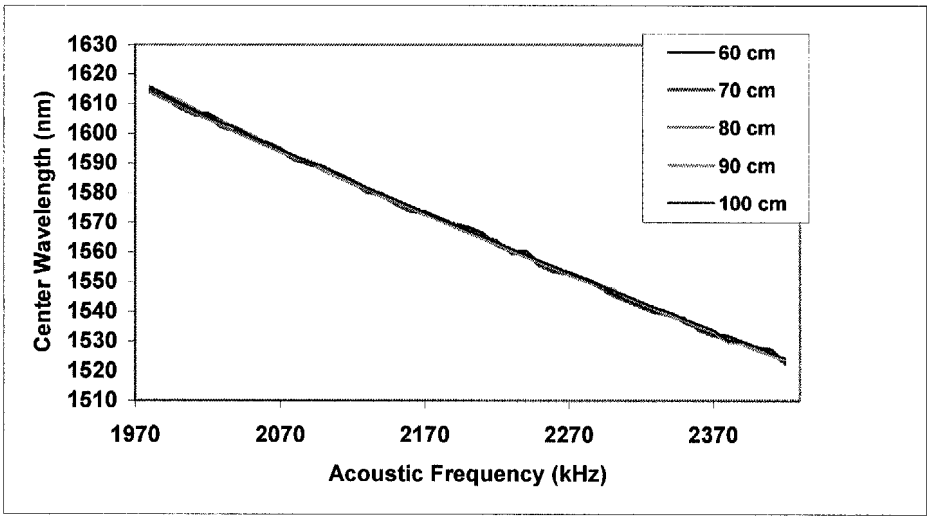

Figure 4.9 Change in the center wavelength of the notch with the frequency of the acoustic wave. The fiber is an unetched fiber with different interaction lengths varying from 60 cm to 100 cm.

Figure 4.9 shows that the central wavelength changes with the acoustic frequency for unetched fibers with different interaction lengths. From Eq. (4.5), there is a linear relationship between the central wavelength and the acoustic frequency.

Figure 4.10(a)–(c) shows a change in the depth of the notch with changing the voltage of the electrical signal applied to the PZT. The interaction length, fiber diameter and acoustic frequency were kept unchanged.

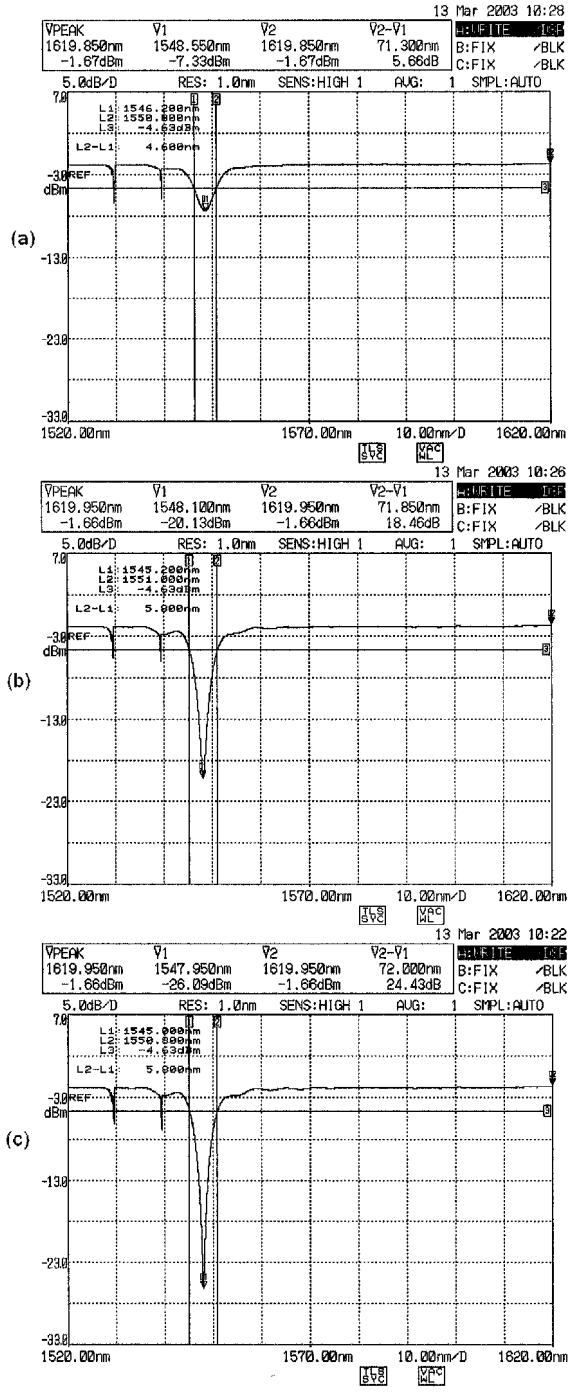

Figure 4.10 Notch depth increases with the applied voltage (a) notch depth of ~5 dB with a peak-to-peak voltage of 7 V, (b) notch depth of ~18 dB with a peak-to-peak voltage of 22 V, (c) notch depth of ~24 dB with a peak-to-peak voltage of 30 V.

4.5 Summary

In conclusion, several parameters that affect the performance of the all-fiber AOTF have been investigated. Based on these findings, all-fiber AOTFs can be designed with optimized performances for different types of application.

Changing the polarization of light modifies the filtering characteristics. The depth of the notch filter increases with an increase in the interaction length. The first significant effect of using a reduced fiber cladding diameter to develop the AOTF was the downwards shift of the center wavelength of the notch with the frequency of the acoustic wave remaining the same. The second significant effect was the widening of the bandwidth. The third effect was the increased depth of the filter notch. Finally, as the fiber diameter decreases, the slope of the center wavelength to the acoustic frequency increases. The central wavelength changes with a change in the applied acoustic frequency. A change in the depth of the notch with a change in the voltage of the electrical signal applied to the PZT has been observed.

4.6 References

[1] Milton Gottlieb, Clive L.M. Ireland and John Martin Ley, *Electro-optic and acousto-optic scanning and deflection*, New York: M. Dekker, 1983.

[2] L. N. Magdich and V. Ya. Molchanov, *Acoustooptic devices and their applications*, New York: Gordon and Breach Science Publishers, 1989.

[3] G. E. Marx, M. Gottlieb and G. B. Brandt, "Integrated optical detector array, waveguide, and modulator based on silicon technology," *IEEE Journal of Solid-State Circuits*, vol. 12, pp. 10–13, 1977.

[4] J. Frangen, H. Hermann, R. Ricken, H. Siebert, W. Sohler and E. Strake, "Integrated optical acoustically tunable wavelength filter," *Electron. Lett.*, vol. 25, pp. 1583–1584, 1989.

[5] A. Alippi, A. Palma, L. Palmieri and G. Socino, "Polarization states of light diffracted by acoustic surface waves" *Applied Optics.* vol. 15, pp. 811–816, 1986.

[6] W. P. Risk, G. S. Kino and H. J. Shaw, "Fiber-optic frequency shifter using a surface acoustic wave incident at an oblique angle," *Opt. Lett.* vol. 11, pp. 115–117, 1986.

[7] N. Grote and H. Venghaus, *Fibre Optic Communication Devices*, Springer, 2000.

[8] H. J. R. Dutton, *Understanding Optical Communications*, International Technical Support Organization.

[9] H. Herrmann, K. Schafer and C. Schmidt," Low-loss tunable integrated acoustooptical wavelength filter in LiNbO3 with strong sidelobe suppression," *IEEE Photon. Technol. Lett.*, vol. 10, pp.120 122, 1998.

[10] G. Keiser, *Optical Fiber Communications* (*Third edition*), McGraw-Hill International Editions, 2002.

[11] H. S. Kim, S. H. Yun, I. K. Kwang and B. Y. Kim, "All-fiber acousto-optic tunable notch filter with electronically controllable spectral profile," *Opt. Lett.*, vol. 22, pp. 1476 1478, 1997.

[12] H. S. Kim, S. H. Yun, H. K. Kim, N. Park and B. Y. Kim, "Actively gain-flattened Erbium-doped fiber amplifier over 35 nm by using all-fiber acoustooptic tunable filters," *IEEE Photon. Technol. Lett.*, vol. 10, pp. 790–792, 1998.

[13] J. Xu and S. Robert, *Acousto-Optic Devices Principles: Design Applications*, John Wiley & Sons Inc, New York, 1992.

[14] H. E. Engan, B. Y. Kim and H. J. Shaw, "Propagation and optical interaction of guided acoustic waves in two-mode optical fibers," *IEEE J. Lightwave Technol.*, vol. 6, pp. 428 435, 1988.

[15] H. E. Engan, D. Ostling, P. O. Kval and J. O. Askautrud, "Scattering of torsional waves in circular rods from diameter discontinuities," *Proc. 1997 IEEE Ultrasonics Symposium*, pp. 597–600, 1997.

[16] Q. Li, X. Liu, J. Peng, B. Zhou, E.R. Lyons and H.P. Lee, "Highly efficient acoustooptic tunable filter based on cladding etched single-mode fiber," *IEEE Photon. Technol. Lett.*, vol. 14, pp. 337-339, 2002.

[17] T. A. Birks, P. St. J. Russel and D. O. Culverhouse, "The acousto-optic effect in single-mode fiber tapers and couplers," *IEEE J. Lightwave. Technol.*, vol. 14, pp. 2519 2529, 1996.

[18] M. Monerie, "Propagation in doubly clad single-mode fibers," *IEEE J. Quantum Electron.*, vol. 18, pp. 535–542, 1982.

[19] T. Jin, Q. Li, J. Zhao, K. Cheng and X. Liu, "Ultra-broadband AOTF based on cladding etched single mode fiber," *IEEE Photon. Technol. Lett.*, vol. 14, No 8, pp. 1133 1135, 2002.

[20] Timothy E. Dimmick, Duane A. Satorius and Geoffrey L. Burdge, "All-Fiber Acousto-Optic Tunable Bandpass Filter," *OFC*, 2000.

[21] J. N. Blake, B. Y. Kim, H. E. Engan and H. J. Shaw, "Analysis of intermodal coupling in a two-mode fiber with periodic microbends," *Opt. Lett.*, vol. 12, pp. 281–283, 1987.

5 Tunable Bandpass Filters

5.1 Introduction

The next generation of reconfigurable optical networks will require dynamic selection and manipulation of wavelength division multiplexing (WDM) channels. Tunable optical bandpass filters (TOBFs) capable of dynamically selecting the WDM channels are therefore important components in such networks. Fiber Bragg grating (FBG) is one of the most promising components used for the development of TOBFs due to several of its advantages, which include all-fiber geometry, low polarization sensitivity, low insertion loss, small size, simple tuning technique and low cost. However, an FBG operating in the transmission mode is a band rejection filter, and it therefore needs to be combined with an expensive and bulky circulator to operate in the reflection mode as a bandpass filter. To overcome this problem, a novel technique is proposed here for the development of a TOBF based on the transmission mode of an FBG.

To save cost and to minimize the insertion loss, a TOBF based on FBG without using any additional optical component is highly desirable for application in the reconfigurable WDM networks. Phase-shifted FBGs [1] and chirped-Moiré gratings [2] are two well-known bandpass fiber gratings. However, the ultra-narrow transmission bandwidth and the Lorentzian shape of the passband of these structures are not suitable for many system applications, which normally requires filters with broader bandwidth and steeper slope [3]. K. Sugden *et al.* have developed a bandpass filter using concatenated chirped FBGs [4], and it has large out-of-band rejection range of ~25 nm and broad transmission bandwidth of ~1 nm. However, this method requires precise control on the grating fabrication process and thus makes tuning of the passband difficult. Large cladding-mode loss in FBGs has also been used to develop bandpass filters [5]. In the transmission spectrum, the gap between the stopband of the large cladding-mode loss and the stopband of FBG are used as the passband of the filter, but the out-of-band rejection range is small (typically < 1 nm). Furthermore, the stopband and transmission bandwidth change when the wavelength of the passband is varied [5]. Another interesting attempt has been carried out by M. G. Xu *et al.* [6]. In their experiment, a piezoelectric stack was used to change the local strain to introduce a temporary phase shift at different positions along a linearly chirped FBG (LCFBG). A step-tunable bandpass filter has been obtained using this method, however, the tuning mechanism is complicated and the rejection ratio of the filter is only 10.6 dB.

5.1.1 Phase-Shifted Fiber Bragg Gratings

A phase-shifted FBG, which comprises a phase jump within a section of the grating, is one of the simplest and most successful bandpass fiber gratings. The phase-shifted FBG can be treated as a Fabry-Perot (F-P) filter with a F-P cavity smaller than the pitch of FBG. The wavelength and transmission ratio of a narrow bandpass peak are determined by the position and size of the phase shift, respectively. Figure 5.1 illustrates the schematic diagram of a typical phase-shifted FBG. Similar to the distributed feedback (DBF) structure used in a semiconductor laser to achieve single-mode operation [7], the FBG with $\lambda/4$ phase shift in the central part of the grating has a passband in the middle of the stopband, which has a very narrow Lorentzian line shape. The principle of the phase shift has been demonstrated in periodic structures made from semiconductor materials, where a phase shift was introduced by etching a larger spacing at the center of the device [8].

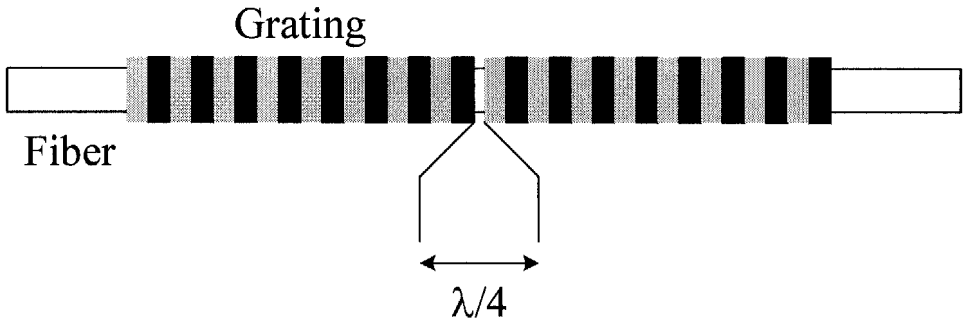

Figure 5.1 Schematic diagram of a typical phase-shifted FBG.

The coupled-mode theory presented in Chapter 2 can be used to analyze the phase-shifted FBG. The transfer matrix method provides a simple means to

obtain the transfer function of the phase-shifted FBG. A phase shift can be incorporated into the T-matrix by multiplying the reflectivity of the *i*th section by matrix elements containing only the phase terms. The transfer matrix of a phase-shifted FBG can be written as [9]

$$\begin{bmatrix} R(-L/2) \\ S(-L/2) \end{bmatrix} = [T^N] \cdots [T^2] \cdot [T^{PS}] \cdot [T^1] \cdot \begin{bmatrix} R(L/2) \\ S(L/2) \end{bmatrix} \tag{5.1}$$

where the transfer matrix T^N represents the amplitude and phase responses of the Nth section of the grating; R and S represent the input and output field amplitudes; L is the length of the phase-shifted FBG. T^{PS} is the phase shift matrix, which can be expressed as

$$T^{PS} = \begin{bmatrix} e^{-j\phi/2} & 0 \\ 0 & e^{j\phi/2} \end{bmatrix} \tag{5.2}$$

where the phase factor, $\phi/2$, is any arbitrary phase that could be due to a change in the local effective refractive index n_{eff} or a gap within the grating, and $j = \sqrt{-1}$.

The phase shift could be introduced into a tiny region in the grating without UV radiation or with UV post-radiation, and hence n_{eff} of a small section of the grating is different from that of the whole grating. In either case, this phase shift can be expressed as [9]

$$\phi = \frac{4\pi}{\lambda}(n_{eff} + \Delta n)\Delta L \tag{5.3}$$

where λ is the wavelength and Δn is the local refractive index change due to UV radiation over a small grating section of length ΔL.

Figure 5.2 shows the measured transmission spectrum of an 8-mm long grating with a quarter-wavelength phase jump in the center [10]. A uniform grating of the same length but without the phase shift incorporated into the grating has a rejection bandwidth approximately half that of the phase-shifted FBG.

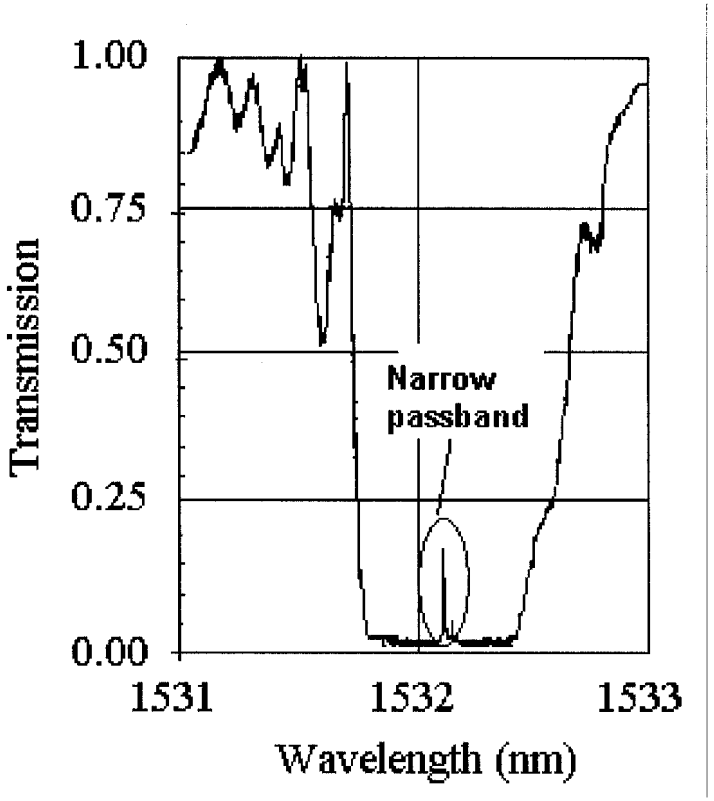

Figure 5.2 Measured transmission spectrum of an 8-mm long grating with a quarter-wavelength phase jump in the center [10].

The phase-shifted FBG can be inscribed into a photosensitive fiber using various techniques as described below.

- *Phase-shifted phase masks.* The phase shift section is incorporated into the phase mask [10]. By using the scanning UV-beam technique or interferometer method, a periodic refractive index modulation with phase shift can be inscribed into the photosensitive fiber resulting in a phase-shifted FBG. The phase-shifted phase mask method provides the repeatability of the manufacture of phase-shifted FBGs in a simple and controlled manner.
- *UV post-processing method.* A permanent phase-shifted FBG can be developed by means of post processing the center of a uniform grating with UV radiation [11]. This method relies on the fact that the UV radiation changes the refractive index locally to produce an additional phase shift [12]. The UV-induced refractive index change required for a $\lambda/4$ phase shift in a 1-mm-long fiber region with a Bragg wavelength of 1530 nm is $\sim 3.8\times10^{-4}$, which can be easily achieved with UV radiation [9].
- *Thermal post-processing method.* It has been observed experimentally that for a high temperature of > 600 K applied to the FBG, the refractive index of the grating can be permanently changed, and for a high temperature of > 1000 K the change is rapid and saturates within minutes [13]. Based on this principle, a phase shift can be induced by post processing a small grating section with high temperature [14]. However, thermal post processing is not easy to control in manufacture, and hence the repeatability and stability of this method are low comparing to other methods.

The features and fabrication methods of phase-shifted FBGs have been briefly described above. The permanent phase-shifted FBG has some important applications in optical communication systems and laser systems as a bandpass filter with ultra-narrow bandwidth. Furthermore, with the trend towards the development of reconfigurable optical networks, tunable bandpass filters are highly desirable. This chapter presents the development of several types of bandpass filters based on the insertion of a temporary phase shift in the chirped FBG.

5.1.2 Temporary Phase Shift in Fiber Gratings

A temporary phase shift introduced into the FBG by external means, such as heating [13], tension [6] or pressure [15], has also been reported. The temporary phase shift will be removed from the FBG in the absence of the external disturbance. The principle of temporary phase shift and its application in optical filters are discussed in this section.

Due to the elastic-optical effect, the refractive index of the fiber changes with external strain. Hence, the external strain applied to a small section of the fiber introduces a phase shift at that point. Using this principle, a tunable optical bandpass filter (TOBF) based on the phase-shifted FBG has been demonstrated by Xu *et al.* who used a piezoelectric stack to change the local strain to introduce a temporary phase shift at different points along the LCFBG, which in turn results in a TOBF [6]. But their proposed TOBF cannot

be continuously tuned in wavelength, its control mechanism is complicated and expensive and its rejection ratio is only 10.6 dB. These disadvantages make it unsuitable for communication applications.

Similarly, the refractive index of the fiber changes with temperature due to the thermo-optical effect. Hence, the temperature change in a small section of the fiber will introduce a phase shift at that point. In this experiment, a resistance wire heater was used to introduce the phase shift in the FBG. The value of the phase shift introduced into the FBG by this technique can be determined by [9]

$$\phi = \frac{2\pi L}{\lambda}\beta\Delta T \tag{5.4}$$

where ϕ is the phase change, L is the length of the heated region, which is the diameter of the resistance wire, ΔT is the temperature change, λ is the wavelength, and β is the thermal-optical coefficient (~8.6×10^{-6} K^{-1} for silica fiber). Here, the change of L due to the thermal expansion coefficient (~0.55×10^{-6} /°C) of the fiber is neglected because it is much smaller than the thermal-optical coefficient of the silica fiber.

For a thermally-induced temporary phase shift, it is important to control the temperature because the high temperature of > 600 K can create a permanent phase shift into the grating as reported in reference [13]. To study the effects of temporary phase shift and permanent phase shift, a 28-mm long FBG was inserted into a tightly fitted loop of NiCr wire with a diameter of 250 μm, which was used as the heating element. The grating was then thermally

bonded to a Peltier-effect heat pump, which was used to keep the unprocessed region of the grating at a constant temperature. For a temperature of less than 570 K, no permanently induced changes in the reflection spectrum of the FBG were observed, even after hours of continuous heat treatment. In comparison, for temperatures > 600 K, permanent resonances were observed in the grating spectrum, and for temperatures approaching 1000 K, the change in the spectrum were rapid and saturated within minutes. In summary, to achieve a repeatable temporary phase shift inserted into the FBG, the applied temperature of less than 570 K must be used.

5.2 Design Principle

This section presents the issues involved in the design of the tunable optical bandpass filters (TOBFs). These issues include the type of grating used, methods to induce a temporary phase shift and heat sink. The design of different types of the TOBFs based on the insertion of a temporary phase shift into the grating is presented.

5.2.1 Linearly Chirped Fiber Bragg Grating

As mentioned in the previous section, a bandpass filter can be achieved by inserting a phase shift into the FBG when the FBG operates in the transmission mode. However, this kind of grating inherently has some unwanted transmission outside of the stopband of FBG. In WDM applications, the unwanted transmission may introduce significant crosstalk between the

wavelength channels. And in laser applications, some unwanted sidemodes could not be easily eliminated from the laser output. Based on this consideration, a grating with a high rejection bandwidth is highly preferred. In all the types of the gratings, a chirped FBG has a large bandwidth, which can be as large as 100 nm by using a phase mask with longer length and larger chirp rate to fabricate the grating. As presented in reference [9], the concept of the phase shift is still applicable in the chirped FBG.

Another feature of the chirped FBG is that its local Bragg wavelength monotonically corresponds to the position of the grating. As a result, tuning of the bandpass peak can be achieved by changing the position of the temporary phase shift introduced into the grating, which can be easily achieved by adjusting the local heating position. A LCFBG with a local Bragg wavelength linearly related to the grating position is desirable for use in the development of tunable optical filters because of the simple tuning mechanism. The local Bragg wavelength relates to the position of a LCFBG as [9]

$$\lambda_B(z) = 2n_{eff}\Lambda(z) = 2n_{eff}\left(\Lambda_0 + \Lambda_1 z\right) \tag{5.5}$$

where $\Lambda(z)$ is the local period of the grating, n_{eff} is the effective refractive index of the fiber, Λ_0 is the starting period of the grating, Λ_1 is the chirping rate, and z is the distance along the fiber.

It should be noted that, when heating the LCFBG with a thermal element, not only a temporary phase shift is introduced into the grating but also a local Bragg wavelength shift due to the temperature sensitivity of FBG. The change

in the local Bragg wavelength due to a temperature change can be expressed as [9]

$$\Delta\lambda_B(z) = \lambda_B(\alpha + \xi)\Delta T(z) \tag{5.6}$$

where λ_B is the Bragg wavelength, $\Delta T(z)$ is the local temperature change, α is the thermal expansion coefficient (for silica, it is typically ~0.55×10^{-6} /°C), and ξ is the thermo-optic coefficient (for silica, it is typically ~8.6×10^{-6} /°C).

From Eq. (5.6), it can be seen that the local Bragg wavelength changes with the variation in the local temperature. Hence, when heating the LCFBG with a thermal element, the Bragg wavelength at the heated section shifts to the longer wavelength side. Theoretically, a transmission peak will be introduced into a continuous stopband of the LCFBG due to the absence of the local Bragg wavelength. However, in the experiment, the heated section is very small and is typically only 0.1–0.2 mm. Using a chirp rate of 2.25 nm/cm of the phase mask, the wavelength gap corresponding to a 0.2 mm heating section is only 0.06 nm, which cannot be identified in the spectrum due to the gradual interface of the heating and unheated sections.

When heating a small section of LCFBG without using the heat sink, due to heat conduction, the small regions of LCFBG on both sides of the heating point are slightly heated (see Fig. 5.3(a)). Due to the temperature sensitivity of FBG, the Bragg wavelength at this relatively broad heated section also shifts to the longer wavelength side. As a result, some broad spectral disturbance is observed in the spectrum of the grating. On the longer wavelength side of the

main transmission peak, because the Bragg wavelengths in the shorter wavelength region are heated and shifted to this region, there is no spectral disturbance observed [16]. When developing a narrowband TOBF, this broad spectral disturbance is undesirable and must be eliminated. Using heat sink, the spectral disturbance can be easily eliminated (see Fig. 5.3(b)). In some other applications, such as the development of TOBF with a broader bandwidth and optical filter with adjustable bandwidth (see Section 5.2.4 and Section 5.2.5), this broad spectral disturbance is desirable to overcome the drawback of the narrow bandwidth and the Lorentzian shape of the phase-shift induced passband.

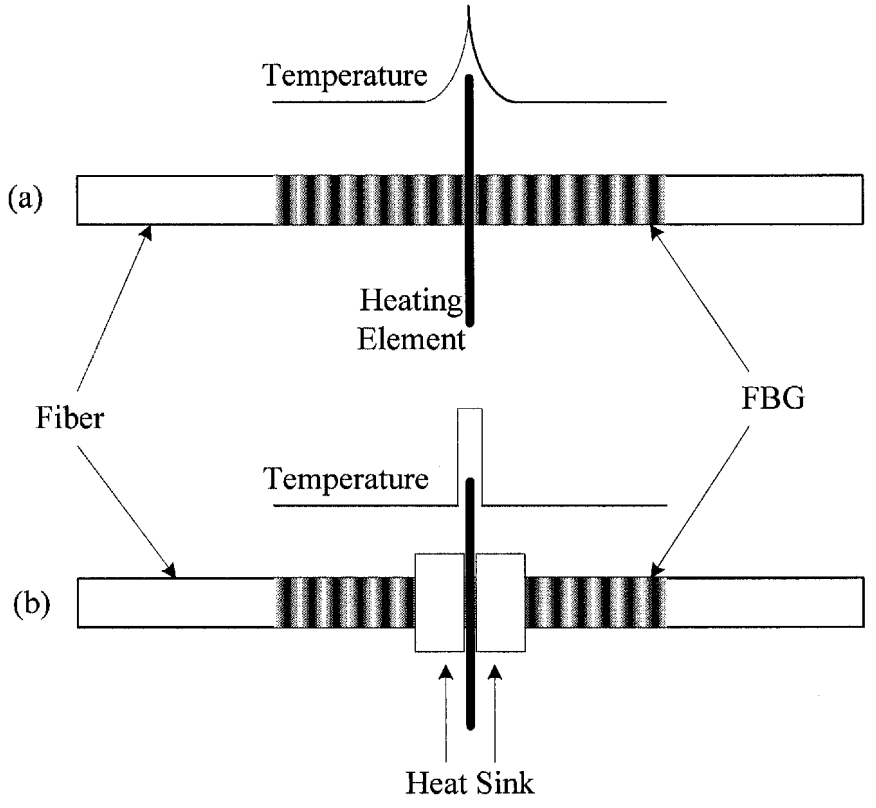

Figure 5.3 Comparison of temperature distribution on the FBG heated by resistance wire without (a) and with (b) heat sink.

In summary, a LCFBG operating in the transmission mode is an ideal choice for use in the development of the TOBF based on the principle of temporary phase shift. This method provides the advantages, which includes large rejection range, large tuning range, and simple tuning mechanism. On the other hand, the tuning speed of the TOBF based on this method is relatively low (< 2 nm/sec).

5.2.2 Heating Mechanism

To develop a tunable filter by introducing a temporary phase shift into the LCFBG, a movable heating element needs to be used to introduce a temporary phase shift. An ideal heating element should satisfy the requirements as described below.

- The heating element should heat the LCFBG at a small section with low thermal conductivity to ensure that the temperature is constant in the unprocessed section.
- The temperature of the thermal element must be easily controlled to allow adjustment of the temperature to achieve optimized performance. From Eq. (5.4), the phase shift value depends on the applied temperature, and hence to achieve a $\lambda/4$ phase shift, the thermal element should be adjusted to a particular temperature.
- The heating element should have minimum damage to the grating (i.e. a permanent refractive index change or physical impairment).

Considering the lifetime of the device, a non-contact heating element is more desirable than a contact heating element. However, a soft-contact heating element is still acceptable in practical applications due to the small strain applied to the fiber.

- The thermal element should be able to be easily scanned along the grating. And the temperature and strain applied to the grating should not change during the scanning. This is very important for a practical tunable filter.
- The consumed power should be as small as possible.

Based on the requirements as described above, two different methods to introduce a temporary phase shift into an FBG have been studied. The first method involves the use of a CO_2 laser to heat the grating and the scanning of the laser beam to tune the filter. The other approach is based on the use of a resistance wire as a thermal element to heat the grating, and the wire can be scanned along the grating which can be controlled by a travel stage.

5.2.2.1 Scanning CO_2 Laser Beam Method

Due to the concern on the repeatability and lifetime of the developed device, the approach involving a non-contact thermal element is highly desirable for this purpose. The CO_2 laser is an ideal heating source, which provides such advantages as small heating point, low thermal conduction, high temperature, and non-contact heating.

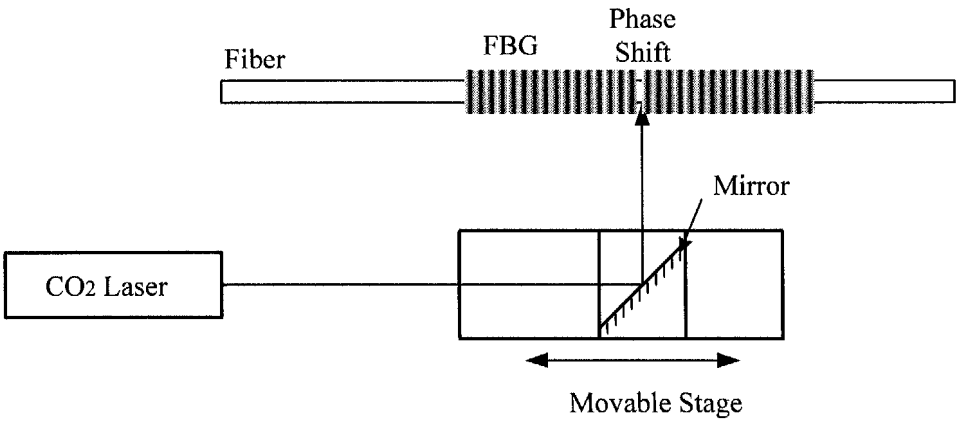

Figure 5.4 Experimental setup for testing the performance of a CO_2 laser as the heating element.

Figure 5.4 shows the configuration of the experimental setup used to test the performance of the CO_2 laser as the heating element. A CO_2 laser with a maximum output power of 25 W was used in the testing. The size of the laser beam was about 2 mm, which had not been focused using extra lenses in the experiment. A pulse generator was used to control the CO_2 laser and the pulse duration was about 1 μs. A 25-mm long uniform FBG was used in this experiment, and the center wavelength of this grating is about 1547.5 nm. By adjusting the mirror, the laser beam could heat the FBG at the center point of the grating. The transmission spectrum of the grating with a temporary phase shift induced by the CO_2 laser is shown as the solid line in Fig. 5.5. For comparison, the original FBG spectrum is shown as the dash line in Fig. 5.5. After switching off the CO_2 laser, the transmission spectrum of the grating was observed to return exactly to the original spectrum.

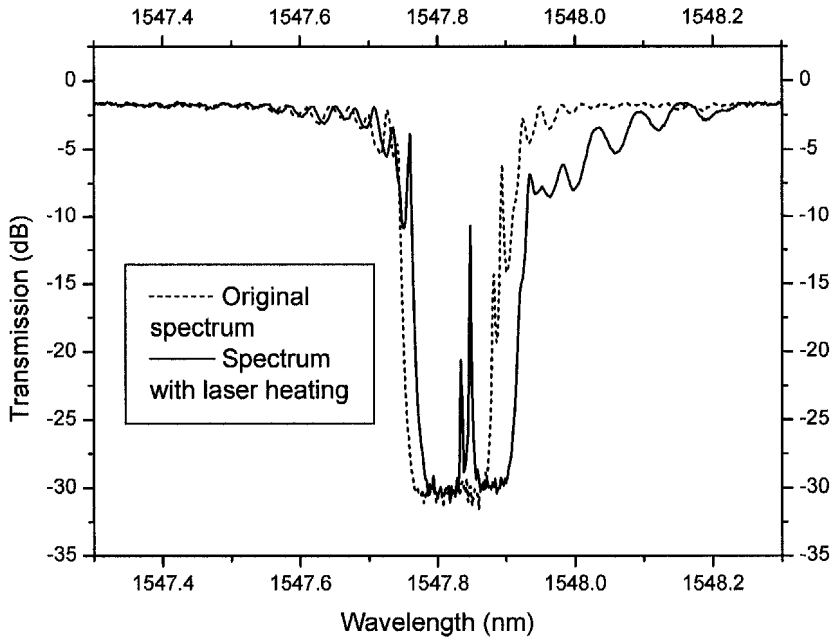

Figure 5.5 Measured transmission spectrum of the grating with a temporary phase shift induced by the CO2 laser.

In the experiment, it has been observed that the whole FBG stopband shifted to the longer wavelength side when the FBG was heated by the CO_2 laser, and this was probably due to the thermal distribution on the grating. At the same time, the bandwidth of the grating was slightly broadened due to the chirp created by the temperature gradient along the grating. One point to note is that the second peak on the short wavelength side of the main passband peak (see Fig. 5.5) is due to the birefringence of the fiber, which is estimated to be $\sim 1\times10^{-5}$ [9]. Another critical drawback of the CO_2 laser heating method is that the laser output power is very unstable. The laser power fluctuation was up to

10% in the experiment, and hence the temperature experienced by the grating could also fluctuate significantly. Furthermore, this method requires use of the CO_2 laser which is very costly. As a result, this method is not suitable for the development of the tunable filter.

5.2.2.2 Scanning Resistance Wire Method

The structure for testing this heating technique is shown in Fig. 5.6. The resistance wire used was a NiCr wire with a diameter of 0.5 mm. A uniform FBG with length of 25 mm and center wavelength of 1546.8 nm was used in the testing. The DC voltage applied to the resistance wire can be adjusted to change the temperature applied to the grating. The resistance wire makes contact with the fiber at the center of the grating.

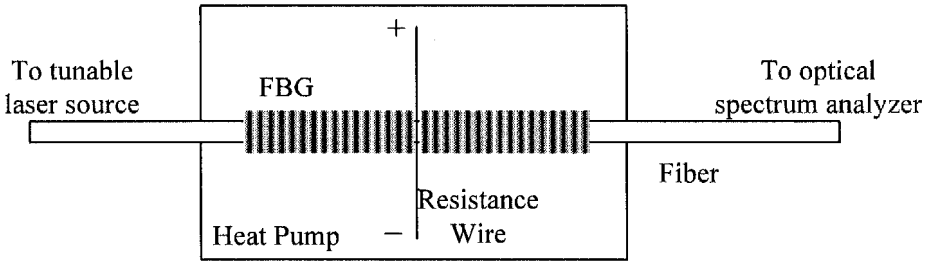

Figure 5.6 Experimental setup for testing the performance of a phase-shifted FBG heated using a resistance wire.

Figure 5.7 shows that the transmission spectrum changes when the temperature applied to the grating increases. The bandpass peak induced by the temporary phase shift was observed as shown in Fig. 5.7 and it was shifted to the longer wavelength side with an increase in the applied temperature of the resistance wire.

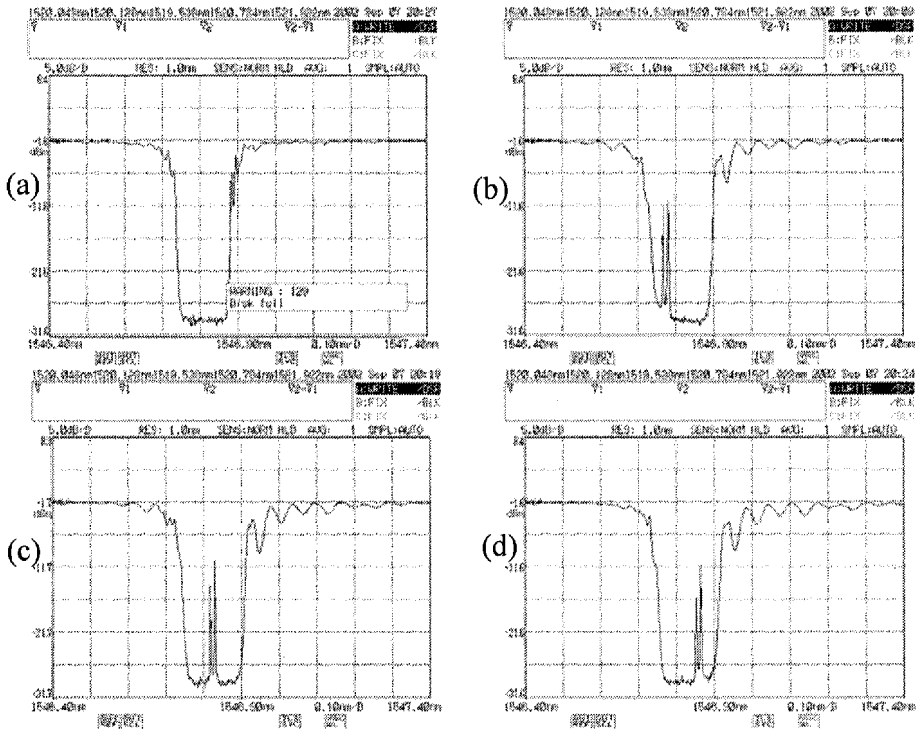

Figure 5.7 Transmission spectrum changes with an increase in the applied temperature of the resistance wire. The temperature increases from curve (a) to curve (d).

The bandpass peak caused by the temporary phase shift was very stable. Additionally, the switching time of the bandpass peak is relatively fast, which is in the sub-second order. It is easy to design a stage for scanning the wire along the grating smoothly. Due to the high temperature of the processing section, the method provides good stability to environmental temperature change. The environmental temperature fluctuation can be neglected compared with the high temperature of the resistance wire, which is up to 300 °C. However, it is noted that this device should be well isolated from

environmental airflow because the violent airflow could cause fluctuation of the temperature of the heating point. Thus, heating using the resistance wire has been found to be suitable for the development of this type of tunable filter. In Fig. 5.7, the sub-peak (next to the main peak) could be due to the presence of birefringence in the fiber that could be caused by the local pressure applied on the fiber after mounting the resistance wire. In the later experiment (see Section 5.3), a new stage was developed to overcome this birefringence problem.

5.2.3 Design of Narrowband Tunable Optical Bandpass Filter

Theoretically, a 100% transmission peak within the stopband can be obtained with $\lambda/4$ phase shift introduced into the center of a uniform FBG. For a LCFBG, the Bragg wavelength changes linearly with the position along the LCFBG [17]. As a result, the central wavelength of the transmission peak can be determined by the position at which the phase shift is introduced. This phenomenon can be verified by simulation using the transfer matrix method. From Eq. (5.1), a phase shift matrix can be inserted in any sequence in the matrix array according to the position of the phase shift introduced into the grating. Figure 5.8 shows the simulation results of a 6-cm long phase-shifted LCFBG with $\lambda/4$ phase-shift point inserted at different positions of the LCFBG. From Fig. 5.8(b), the transmission peak in the stopband of LCFBG changes linearly with the position of the inserted phase shift. Thus, if one can change the phase-shifted position in the LCFBG, a TOBF can be developed.

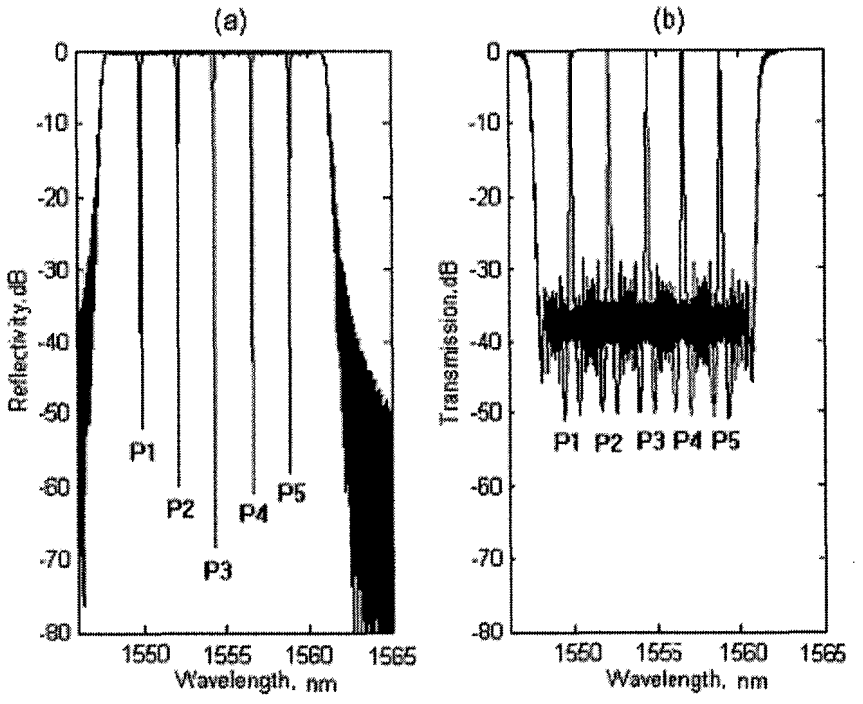

Figure 5.8 Simulation results of (a) reflection spectrum and (b) transmission spectrum of a 6-cm long LCFBG with λ/4 phase shift inserted at positions of P1=1 cm, P2=2 cm, P3=3 cm, P4=4 cm, P5=5 cm.

Due to possible heat conduction, the small regions of LCFBG on both sides of the heating point could be slightly heated. Due to the temperature sensitivity of FBG, the Bragg wavelength at the heated section will shift to the longer wavelength side. As a result, some broad spectral perturbations will be introduced to the shorter wavelength side of the main transmission peak. On the longer wavelength side of the main transmission peak, because the Bragg wavelength in the shorter wavelength region is heated to shift to this wavelength region, there is no spectral perturbation observed [16]. Hence, a heat sink must be used to achieve a high-performance filter with narrow bandwidth and sharp edge of the filter.

5.2.4 Design of Broadband Tunable Optical Bandpass Filter

Even though the phase-shifted FBG is very attractive for some applications such as locking of laser mode when placed in the laser cavity, its ultra-narrow transmission bandwidth and the Lorentzian shape of the passband are not suitable for many system applications, which normally require filters with broader bandwidth and steeper slope [18].

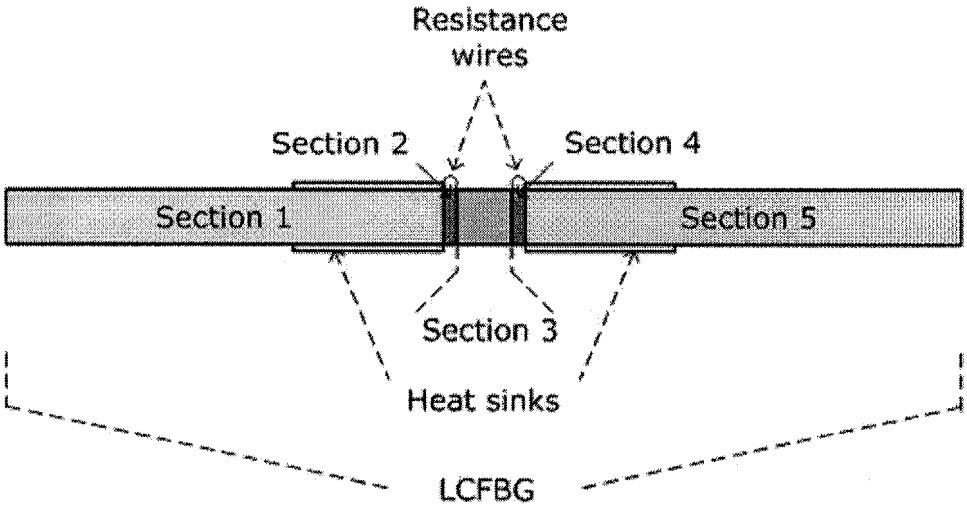

Figure 5.9 Schematic of the proposed broadband TOBF based on the phase-shifted LCFBG. The LCFBG can be divided into five sections when heated by two resistance wires.

Figure 5.9 shows the schematic diagram of the proposed TOBF. Two resistance wires are placed across the outer surface of the LCFBG as thermal heads to introduce the thermo-refractive effects into the LCFBG. Two heat sinks are placed beside the two resistance wires to eliminate any unwanted

effect due to thermal conduction. When applying the DC power to the resistance wires, due to the local Bragg wavelength shift and the phase shifts induced by a temperature increase as described in Section 5.1.2, a broad passband peak within a wide stopband of the LCFBG can be obtained.

The passband peak can be switched off by removing the DC power supply from the resistance wires. The center wavelength of the passband can be tuned within the stopband of the LCFBG by scanning the resistance wires together with the heat sinks along the LCFBG. The stopband of the LCFBG remains unchanged when tuning the passband peak over the whole tuning range. The tuning range of the proposed TOBF is only limited by the stopband window of the LCFBG, which could be as large as 100 nm by using a long phase mask with large chirp rate to fabricate the LCFBG.

For the same DC voltage applied to the two resistance wires, the LCFBG can be divided into 5 sections according to the heat distribution (see Fig. 5.9). It is assumed that the temperature in each section is uniform. Sections 1 and 5 are the sections of LCFBG that are not thermally affected by the resistance wires. Hence, the temperatures in sections 1 and 5 will remain unchanged before and after heating. As a result, the local Bragg wavelengths of the LCFBG in section 1 and section 5 will remain unchanged before and after heating. The two resistance wires are placed in contact with the LCFBG at sections 2 and 4. It is assumed that the areas of the heating points (sections 2 and 4) are equal to the diameter of the resistance wires. This assumption is valid when the

diameters of the resistance wires (~0.1 mm) are smaller than or comparable to the diameter of the fiber (0.125 mm). Sections 2 and 4 of the LCFBG are directly heated by the resistance wires, resulting in a large increase in the temperature. Section 3 is the gap between the two resistance wires. Because there is no heat sink in section 3, the temperature of section 3 will also increase due to thermal conduction. The local Bragg wavelength in section 3 will shift to the longer wavelength side, resulting in a passband peak in the transmission spectrum because of the absence of the Bragg wavelengths in the LCFBG that would otherwise be reflected in section 3. At the same time, the high temperatures in sections 2 and 4 will result in two temporary phase shifts. Due to the small sizes of sections 2 and 4, the local Bragg wavelength shift can be neglected. The strong resonances at these two points due to the phase shifts will introduce two steep slopes to the broad passband induced by the local Bragg wavelength shift in section 3. Thus, a broad passband with steep slopes can be obtained.

Using the transfer matrix method, the transmission spectrum response of the LCFBG heated by two resistance wires has been simulated. The simulation result is shown as the dotted line in Fig. 5.10. In the simulation, the length of the LCFBG is 60 mm, the chirp rate is 2.25 nm/cm, the distance between the two resistance wires is 3.5 mm, and the same temperature of sections 2 and 4 and the temperature of section 3 are set as 250 °C and 150 °C, respectively. The experimental result is also shown in Fig. 5.10 as the solid line. It can be seen from Fig. 5.10 that the experimental result matches reasonably well with

the simulation result within the passband. In the two stopbands, the discrepancies between the simulated and experimental results are due to the transmission noises, which cannot be predicted in the simulation.

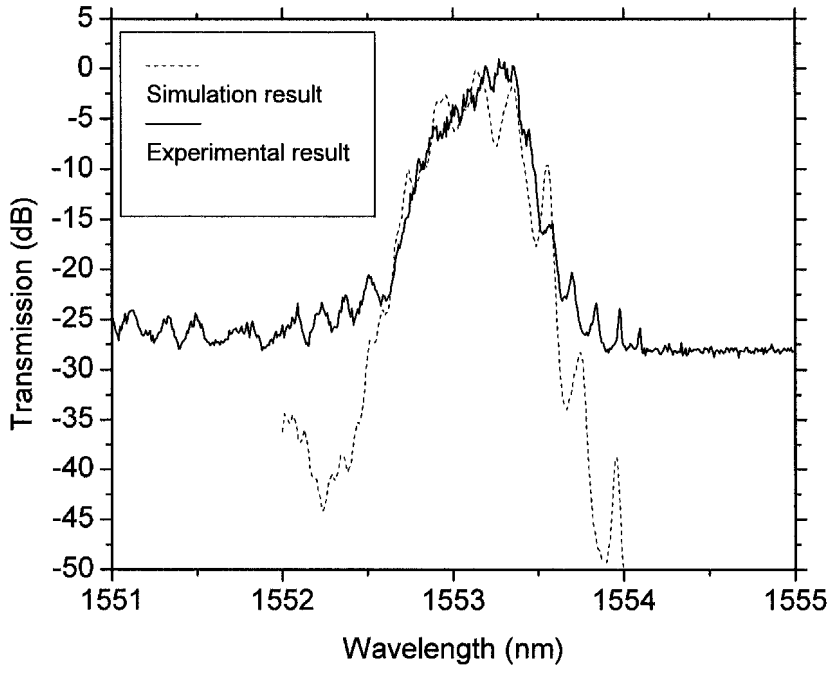

Figure 5.10 Comparison of the simulation result (dotted line) and experimental result (solid line) of the passband peak created by the two resistance wires in the LCFBG.

In the LCFBG, the local Bragg wavelength linearly changes with the position along the LCFBG. As a result, the center wavelength of the passband peak of the TOBF also linearly changes with the position of the resistance wires. When the resistance wires together with the heat sinks are scanned along the LCFBG, the center wavelength of the passband peak will shift within the fixed

stopband of the LCFBG. A TOBF can therefore be developed based on this principle.

5.2.5 Design of Optical Bandpass Filter with Adjustable Bandwidth

DWDM systems are widely deployed to increase the transmission capacity and provide a wealth of applications for optical filters. The filter requirements for the bandpass filters become more demanding as the number of channels, the bandwidth utilization and the system wavelength range increase. Furthermore, different transmission formats are used in WDM systems, for example, non-return-to-zero (NRZ) and frequency shift keying (FSK). The transmission format used will have an effect on the allowable channel spacing, and will hence affect the filter requirements. As such, for WDM systems with different transmission speeds, different channel spacing and/or different modulation formats, optical filters with different filtering characteristics are required to optimize the system performance [19]. As a result, an optical bandpass filter with adjustable bandwidth is highly desirable to support different types of transmission systems and to enable the upgrade of the systems.

In this section, the design of an optical bandpass filter with adjustable bandwidth using phase-shifted LCFBG (PS-LCFBG) is presented. Figure 5.11 shows the schematic diagram of the structure used to broaden and adjust the

transmission bandwidth of the PS-LCFBG. The PS-LCFBG can be simply divided into six sections for analysis. Sections 1 and 6 are the parts of the PS-LCFBG that are not thermally affected by the thermal head. Section 2 is the part of LCFBG with a permanent phase shift, which can be obtained by inscribing the phase-shifted LCFBG with thermal post-processing technique. Section 4 is the part of LCFBG that is in contact with the thermal head. The temperature of section 4 increases significantly with that of the thermal head. Sections 3 and 5 are the parts of LCFBG next to section 4, and the temperatures of sections 3 and 5 also increase with the temperature of the thermal head due to thermal conduction. Here, to simplify the analysis, it is assumed that the temperature in each section is uniform.

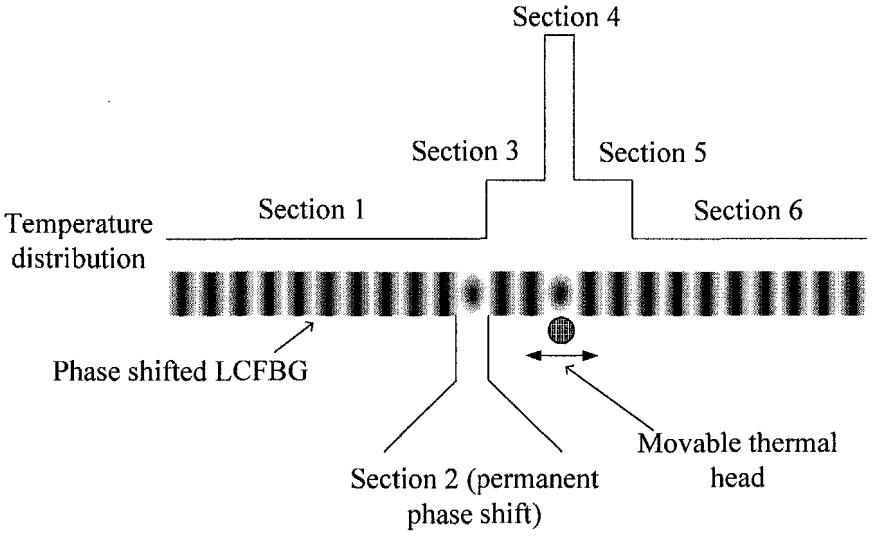

Figure 5.11 Schematic diagram of the structure used to broaden and adjust the transmission bandwidth of the PS-LCFBG.

When section 4 is heated by the thermal head, the refractive index in section 4 increases with the temperature due to the thermo-optical effect, and hence a

temporary phase shift will be introduced into section 4. When the temperature in section 4 is lower than 570 K, no permanent phase shift will be inscribed into the LCFBG.

At the same time, the temperatures in sections 3 and 5 will also increase due to thermal conduction, which will cause the local Bragg wavelength to shift to the longer wavelength side. The relationship between the temperature increase and the local Bragg wavelength shift is given by Eq. (5.6). The local Bragg wavelength shift in sections 3 and 5 will result in a passband peak within a stopband of the transmission spectrum because of the absence of the Bragg wavelengths in the LCFBG that would otherwise be reflected in sections 3 and 5 [16].

The passband peak due to the temporary phase shift and the passband peak due to the thermally-induced local Bragg wavelength shift are introduced into the stopband of the PS-LCFBG beside the original passband peak. As a result, the original narrow passband peak is broadened when these two thermally-induced passbands are combined. The passband peaks due to the effects of both the permanent phase shift and the temporary phase shift will act as two shape edges in the newly obtained broadened passband. And the passband due to the local Bragg wavelength shift acts as the center body of the newly obtained passband.

Using the transfer matrix method (see Eq. (5.1)), the spectrum of the passband of the PS-LCFBG obtained using the thermal head has been simulated based on the model shown in Fig. 5.11.

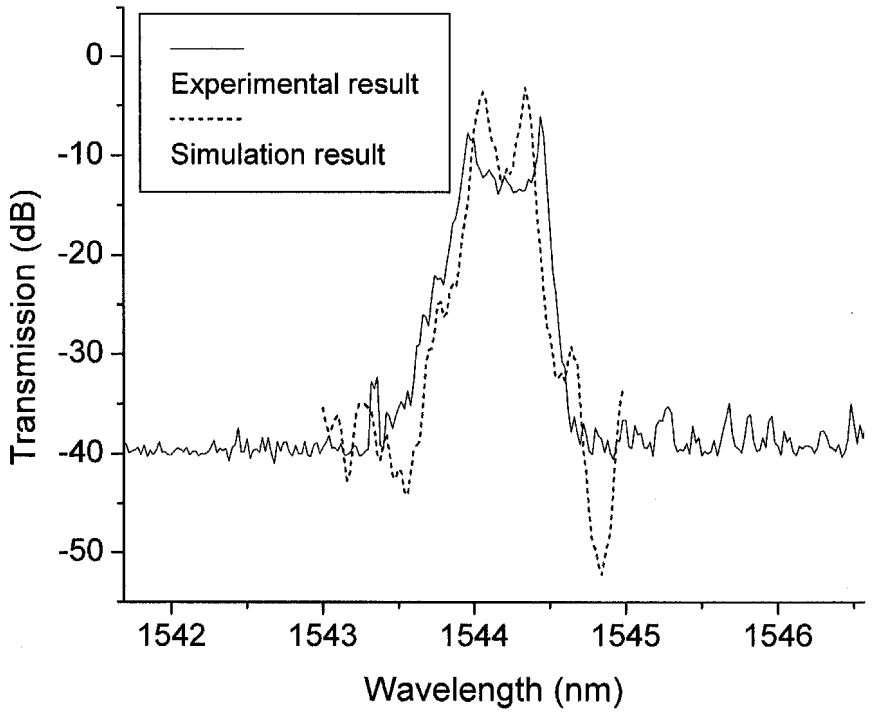

Figure 5.12 Comparison of the simulation result and experimental results of the broadened passband of the PS-LCFBG using a thermal head to provide a single heating point on the device.

Figure 5.12 shows the simulation result and the experimental result of a 6-cm long PS-LCFBG which was heated using a thermal head with 0.2 mm heating size, and the distance between the resistance wire and the permanent phase shift was 1 mm. The simulation result and the experimental result match

reasonably well with each other. From Fig. 5.12, the main differences between the experimental result and the simulation result are the bandwidth difference and the transmission power difference, and these discrepancies are probably due to the difference between the temperature used in the simulation and the actual temperature in the experiment.

When the thermal head is moved along the PS-LCFBG, the edge of the passband with a temporary phase shift introduced will change, while the other edge is unchanged. As a result, the bandwidth of the passband can be changed with the position of the thermal head. Thus the passband of the PS-LCFBG can be broadened and adjusted with a movable external thermal head within the passband.

5.3 Devices Development and Testing

This section presents the development and testing of several types of optical filters, and they are TOBF with ultra-narrow bandwidth, TOBF with broad bandwidth, and a bandpass filter with adjustable bandwidth.

5.3.1 Narrowband Tunable Optical Bandpass Filter

Figure 5.13 shows the schematic diagram of the proposed TOBF. A NiCr resistance wire heater is used to introduce a temporary phase shift into the LCFBG. The diameter of the resistance wire is 0.2 mm. The wire is attached to a linear travel stage. The phase-shifted position can be changed by adjusting

the travel stage. A 6-cm long LCFBG was inscribed in a heavy hydrogen-loaded cladding mode suppressed fiber (soaked in hydrogen under 100 bar pressure for more than 30 days) using a linearly chirped phase mask with a chirp rate of ~2.25 nm/cm. The rejection ratio of this TOBF was designed to be as large as possible, a deep stopband of LCFBG is thus necessary. As a result, heavy hydrogen loading is an important process in the experiment. After annealing in a chamber at 80 °C for 12 hours, the rejection ratio of this LCFBG is larger than 30 dB and the rejection band ranges from 1536.5 nm to 1557 nm. The LCFBG is fixed on a linear travel stage with two fiber holders. The wire heater is good contact with the bare fiber with LCFBG, and it can be smoothly scanned along the LCFBG as controlled by the travel stage.

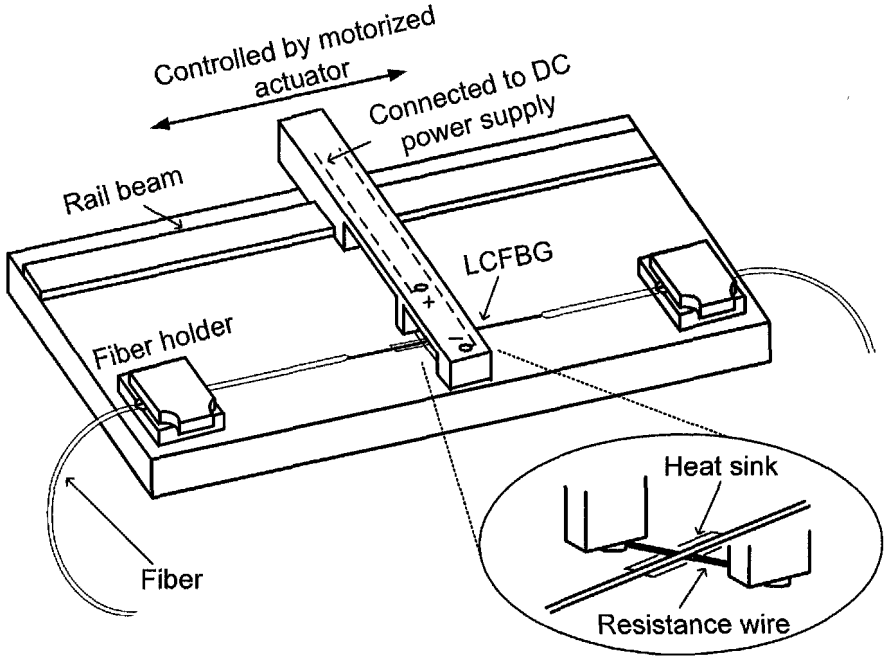

Figure 5.13 Schematic diagram of the proposed narrowband TOBF.

With a DC voltage of 0.7 V applied to the resistance wire heater, the LCFBG was heated at the contact point with the wire. A particular phase change was introduced into the LCFBG and a bandpass window was opened up in the stopband of the LCFBG. As given in Eq. (5.4), the amount of phase shift will depend on the length of the heated section L and the temperature increase ΔT. The temperature of the resistance wire can be controlled to introduce a $\pi/2$ phase shift into the LCFBG.

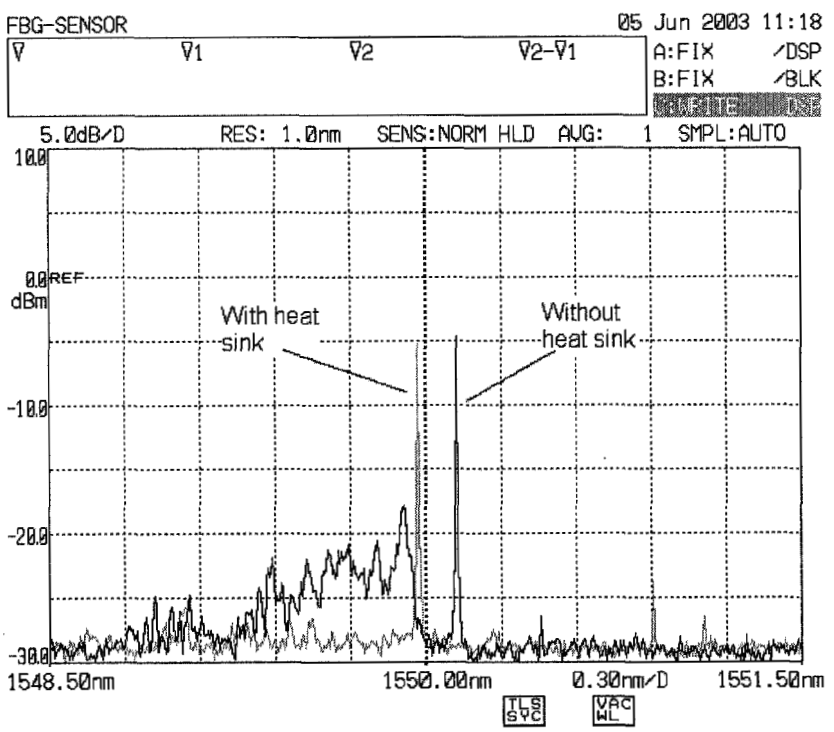

Figure 5.14 Detailed spectra of the narrowband TOBF without heat sink (black), and with heat sink (gray).

A broad spectral perturbation was observed in the experiment due to thermal conduction. Using a heat sink, this spectral perturbation can be easily eliminated (see Fig 5.14). Figure 5.15 shows the shift of the passband from

1539.2 nm to 1555.6 nm when the position of the resistance wire was varied over the 5 cm length. The 3-dB bandwidth of the TOBF is as small as ~7 pm, the tuning range is 16.5 nm, and the rejection ratio is more than 25 dB. The minimum insertion loss of this narrowband TOBF is ~ 2dB. The central wavelength of the passband peak varies linearly according to the position of the heating point. Figure 5.16 shows a linear relationship between the heating position and the center wavelength of the passband peak. The tuning slope is about 0.32 nm/mm.

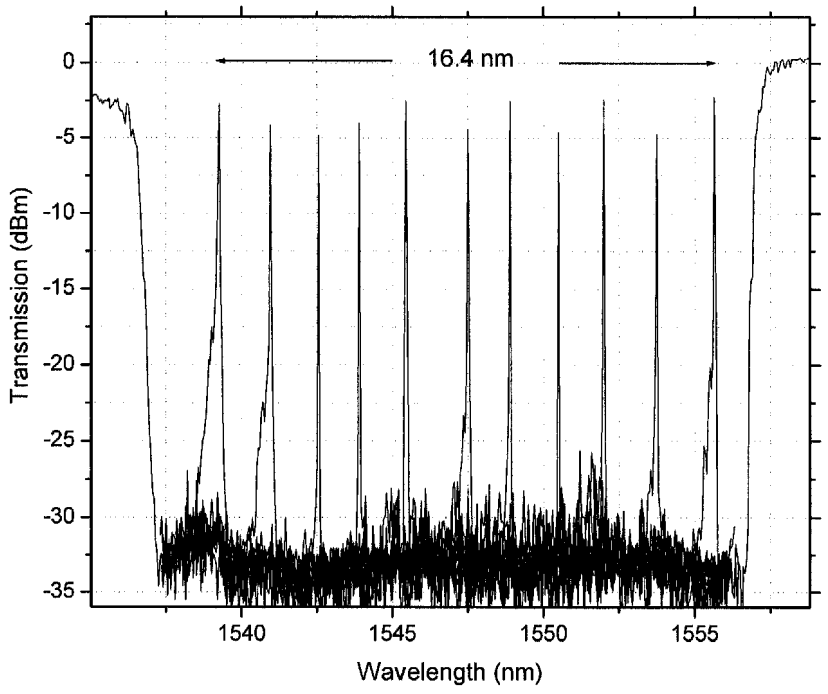

Figure 5.15 The central wavelength of the passband peak of the narrowband TOBF was tuned from 1539.25 nm to 1555.65 nm.

A new narrowband TOBF with switchable passband has been developed. This TOBF has a very small bandwidth of ~7 pm, tuning range of 16.4 nm and 25 dB rejection ratio. As mentioned in Section 5.2.1, the tuning range of this narrowband TOBF can be increased to 100 nm or more by using the LCFBG with a larger chirp rate and/or longer length.

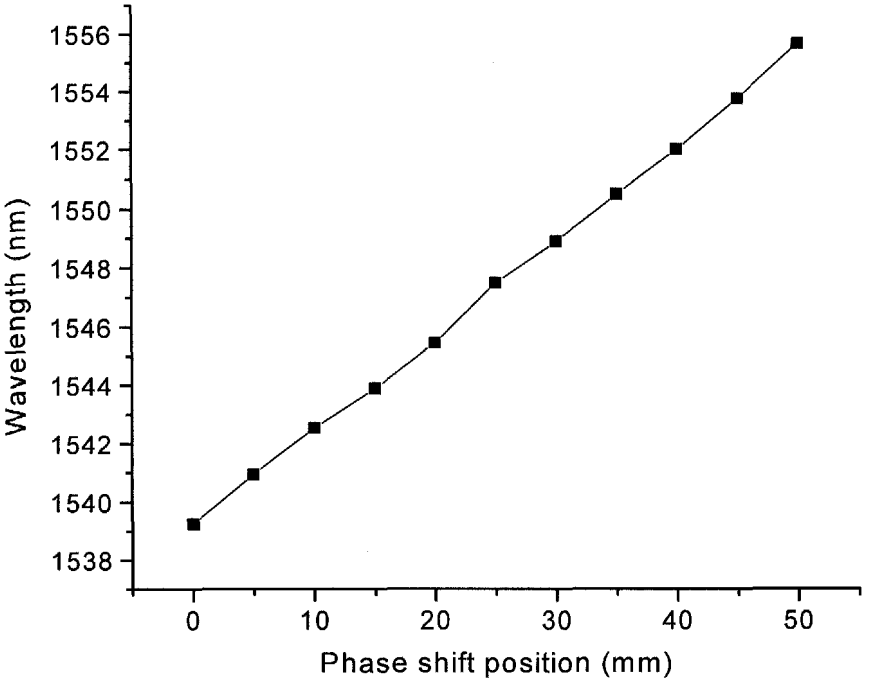

Figure 5.16 Linear variation of the central wavelength of the narrowband TOBF with the heating position, which corresponds to the phase shift position.

5.3.2 Broadband Tunable Optical Bandpass Filter

This section presents the development of a broadband TOBF. The fabrication process of the LCFBG has already been discussed in Section 5.3.1. However,

the fiber used in this broadband TOBF was a normal fiber instead of a cladding mode suppressed fiber. The stopband of the LCFBG was measured to be from 1535 nm to 1555 nm and the maximum rejection ratio was larger than 30 dB. Two NiCr wires with a diameter of 0.1 mm were used as thermal heads to introduce a passband within the stopband of the LCFBG, and two heat sinks were used to avoid unwanted heating in sections 1 and 5 (see Fig. 5.9). The resistance wires together with the heat sinks can be scanned along the whole length of the LCFBG using a linear travel stage. To obtain a ~0.2 nm transmission bandwidth, the distance between the two wires was fixed at 3.5 mm.

It is noted that, by heating the LCFBG with a single resistance wire without heat sink, both the passband peak induced by the local Bragg wavelength shift and the passband peak induced by the thermally-induced phase shift can be identified in the transmission spectrum of the LCFBG (see the black line in Fig. 5.17). The gray line in Fig. 5.17 shows the broad passband in the stopband of the LCFBG obtained using two resistance wires and two heat sinks. This observation can be explained as follows. When applying a DC voltage to a single resistance wire without heat sink, the local Bragg wavelength in the region besides the wire shifts to the longer wavelength side resulting in a passband due to the absence of the Bragg wavelengths in the LCFBG that would otherwise be reflected from the heated region. At the same time, a temporary phase shift due to the large temperature increase of LCFBG at the contact point with the wire results in a narrow and sharp bandpass peak.

(a)

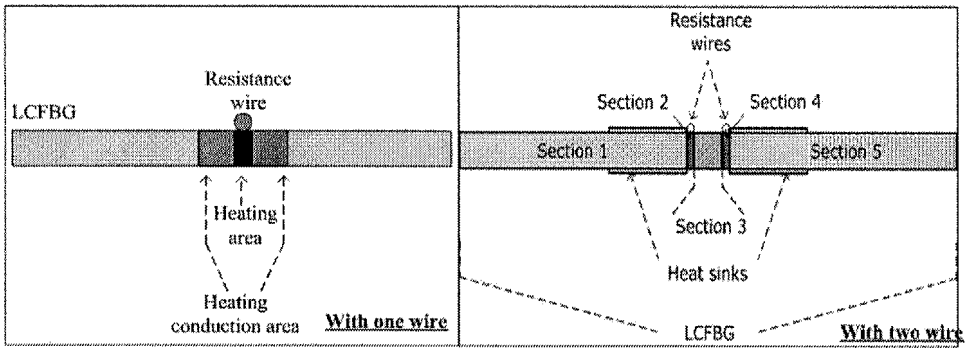

(b)

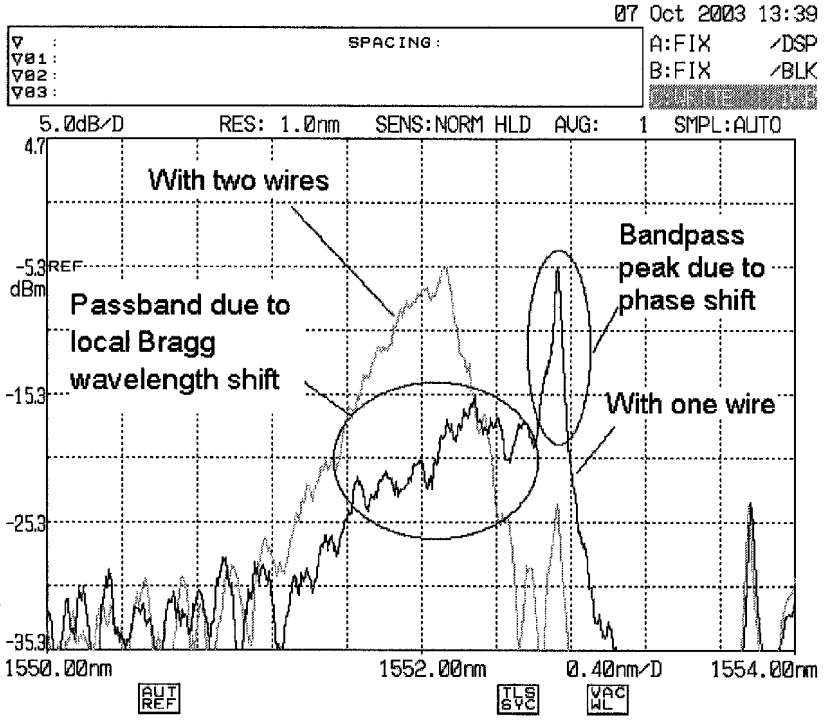

Figure 5.17 (a) The schematic diagram of the two experimental setups; (b) Transmission spectra of the passband peak obtained using a single resistance wire (black line) and of the passband peak obtained using two resistance wires (gray line).

However, using the two resistance wires and two heat sinks, the local Bragg wavelength shift in section 3 results in a broad passband, while the two thermally-induced phase shifts in sections 2 and 4 (see Fig. 5.17 (a)) result in two steep slopes on the broad passband induced by local Bragg wavelength shift. As a result, a broad passband with steep slopes can be obtained using two resistance wires and two heat sinks. Although this device requires a relatively high temperature to operate, the total power consumed was less than 1.5 W, which is relatively small.

When the two resistance wires together with the two heat sinks were scanned along the 60-mm long LCFBG over a distance of 45 mm, the center wavelength of the passband peak shifted from 1538.2 nm to 1553.3 nm with a tuning range of ~15 nm (see Fig. 5.18). The tuning slope is about 0.33 nm/mm. On the longer wavelength side, it can be seen that the maximum rejection ratio is ~25 dB and the minimum insertion loss is ~4 dB. On the shorter wavelength side, the transmission drops by ~8 dB due to the undesirable cladding-mode losses in the standard single-mode fiber, and this results in a smaller rejection ratio of ~15 dB and a larger insertion loss of ~13 dB. These problems caused by the cladding-mode losses in the standard single-mode fiber can be easily overcome using a cladding-mode suppressed fiber in the fabrication of the LCFBG. Thus, it is anticipated that the insertion loss variation could be reduced to less than 2 dB by using a LCFBG based on a cladding-mode suppressed fiber. Figure 5.19 shows a linear relationship between the heating position and the center wavelength of the passband.

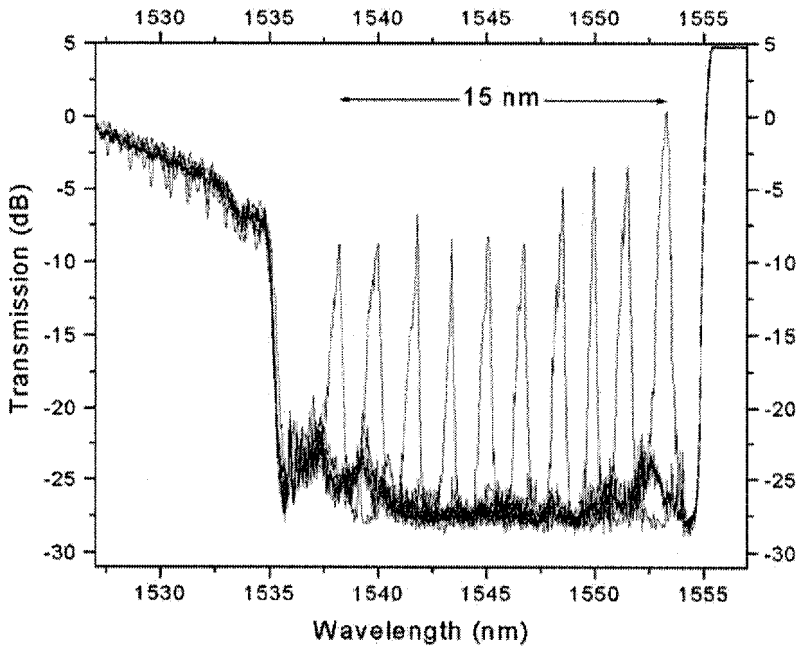

Figure 5.18 Transmission spectrum of the broadband TOBF showing a 15-nm tuning of the passband peak when the resistance wires were scanned over a distance of 45 mm along the LCFBG.

A new broadband TOBF has been developed using a single LCFBG. The TOBF has a bandwidth of ~0.2 nm, an out-of-band rejection range of ~20 nm, a tuning range of ~15 nm, a minimum insertion loss of ~4 dB and a maximum rejection ratio of ~25 dB. As mentioned in Section 5.2.1, the tuning range of this broadband TOBF can be increase to 100 nm or more by using the LCFBG with larger chirp rate and/or longer length.

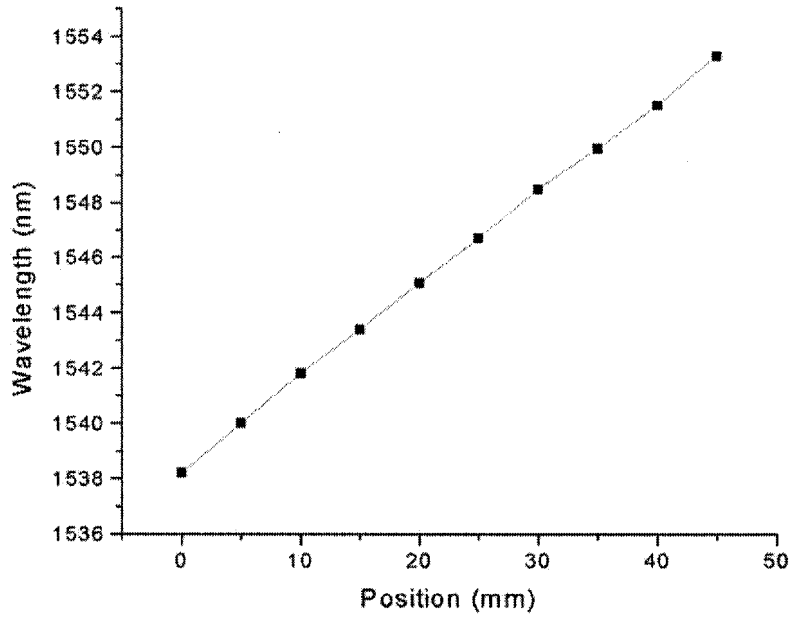

Figure 5.19 Linear variation of the central wavelength of the broadband TOBF with the heating position.

5.3.3 Optical Bandpass Filter with Adjustable Bandwidth

A 6-cm long LCFBG was inscribed into a hydrogen-loaded cladding-mode-suppressed fiber with UV scanning beam technique using a linearly chirped phase mask with a chirp rate of 2.25 nm/cm. The rejection ratio of the LCFBG was measured to be larger than 30 dB, and its stopband is from 1536.5 nm to 1558 nm. A PS-LCFBG was fabricated with thermal post-processing technique. A NiCr resistance wire with a diameter of 0.2 mm was placed across the LCFBG to thermally introduce a permanent phase shift into the LCFBG [13].

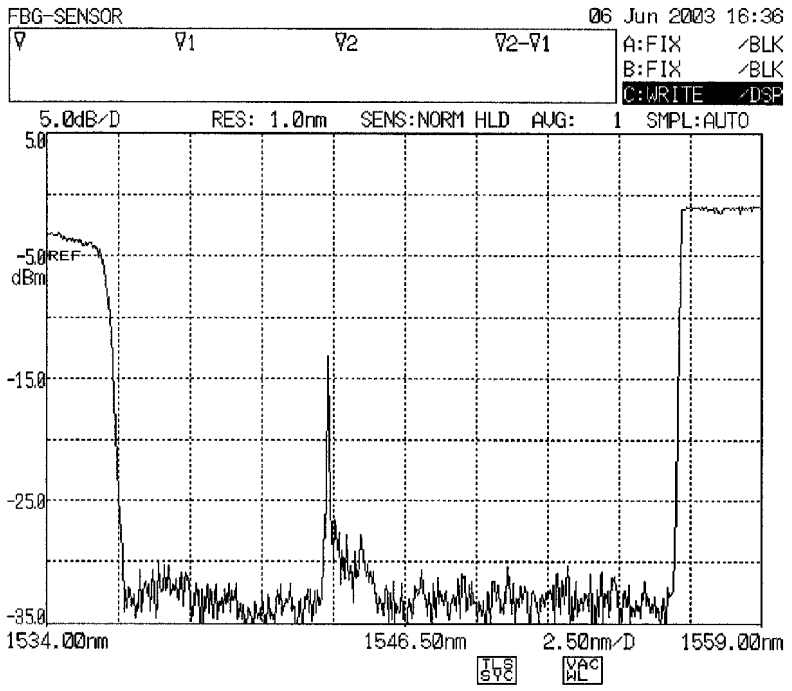

Figure 5.20 The spectrum of the fabricated phase-shifted LCFBG with thermal post-processing technique. (The bandwidth of the spectral peak was measured to be smaller than 10 pm).

When applying a DC voltage of 3 V to the resistance wire, the high temperature of the resistance wire will induce a permanent refractive index change at the contact point of the LCFBG, and hence introduces a permanent phase shift into the LCFBG. Figure 5.20 shows the transmission spectrum of the PS-LCFBG. The narrow passband was measured using an optical spectrum analyzer (OSA) with a resolution of 10 pm. The bandwidth of the spectral peak was measured to be ~7 pm, which is smaller than the OSA resolution of 10 pm.

Another identical NiCr resistance wire with an applied low voltage of 0.4 V was placed across the PS-LCFBG on the longer wavelength side of the permanent phase shift (see Fig. 5.11). It was used as a thermal head to introduce the temporary phase shift and the local Bragg wavelength shift into the PS-LCFBG. This resistance wire was attached to a travel stage. By controlling the travel stage, the thermal head can be smoothly scanned along the LCFBG, which will tune the distance between the permanent phase shift and the temporary phase shift, resulting in the adjustment of the bandwidth of the passband.

When applying a DC voltage to the NiCr resistance wire, a passband peak will be introduced into the stopband of the PS-LCFBG due to the temporary phase shift. This passband peak due to the temporary phase shift will be introduced to the longer wavelength side of the original passband peak of the PS-LCFBG. The spectral separation between the two passband peaks is determined by the distance between the permanent phase shift and the resistance wire. The local Bragg wavelength shift in sections 3 and 5 (see Fig. 5.11) will contribute to another passband between the two passband peaks, which will combine the two passband peaks to obtain a broader passband. The bandwidth of the new passband is determined by the distance between the permanent phase shift and the resistance wire, and hence can be adjusted by changing the position of the resistance wire with the travel stage.

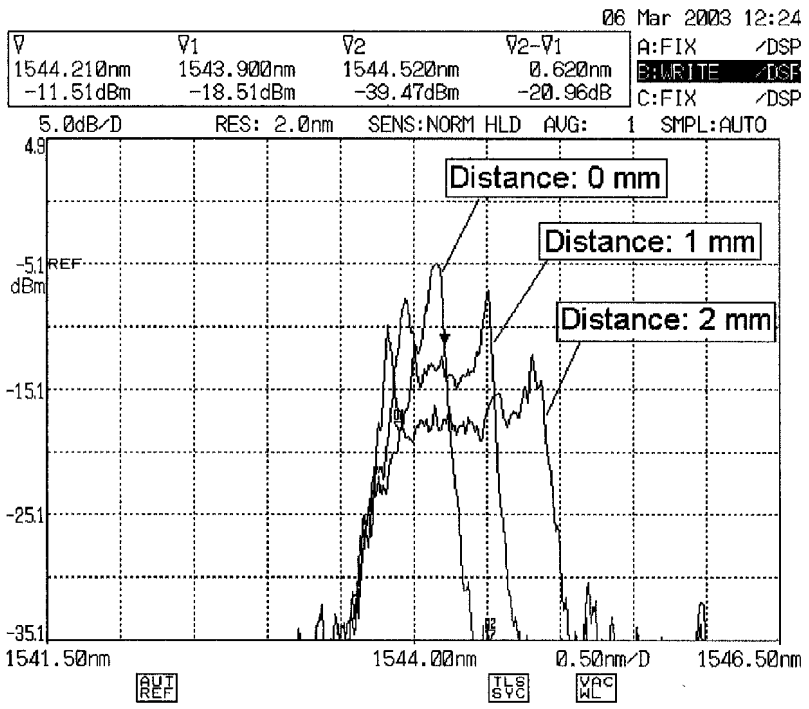

Figure 5.21 The bandwidth of the passband is broadened when changing the distance between the permanent phase shift and the temporary phase shift from 0 mm to 2 mm.

Figure 5.21 shows the experimental results. When applying a DC voltage of 0.4 V to the resistance wire with a distance of 0 mm from the position of the permanent phase shift, the bandwidth of the passband peak of the PS-LCFBG becomes broadened from < 10 pm to ~0.16 nm. And when adjusting the gap between the position of the permanent phase shift and the resistance wire from 0 to 2 mm, the bandwidth can be tuned from ~0.16 nm to ~1.05 nm. This device is robust against the environmental temperature change. Because the temperature of the heating point is much higher than that of the environment, the fluctuation of the environmental temperature can be neglected compared to the high temperature of the heated position.

A novel optical bandpass filter with adjustable bandwidth has been developed. This filter has many potential applications in WDM systems. To the author's knowledge, this is the first proposal to improve and adjust the bandwidth of a phase-shifted fiber Bragg grating after fabrication.

5.4 Summary

Several types of tunable filters with different characteristics and applications have been developed based on the insertion of a temporary phase shift into the LCFBG. The TOBF has several advantages, which includes continuous tuning, simple construction, easy control technique, low cost, narrow bandwidth, low polarization sensitivity and large tuning range. Using the LCFBG with a larger rejection bandwidth, a TOBF with larger tuning range can be easily developed. The narrow bandwidth TOBF can be potentially used for laser mode locking when placed inside the laser cavity. The broadband TOBF can be used in the WDM systems to manipulate a particular wavelength channel. Both the narrowband and broadband TOBFs have several unique features. First, the proposed tuning technique can overcome the limited tuning range of conventional FBGs (e.g. using strain) due to the physical failure feature of the silica fiber. It should be noted that the tuning range of the TOBF, which depends on the stopband window, could be easily extended to 100 nm or more by using a LCFBG with a larger chirp rate and longer length. Second, the passband peak could also be switched off by removing the DC power from the resistance wires. Finally, attenuation of the bandpass peaks of these filters can

be adjusted by changing the applied voltage (see Section 7.2.2). Table 5.1 summarizes the important parameters of the devices presented in this chapter.

Type	Narrowband TOBF	Broadband TOBF	Bandwidth adjustable TOBF
Insertion loss	~2 dB	~4 dB (min)	<6 dB
Bandwidth	~7 pm	~0.2 nm	0.16 nm (initial bandwidth)
Tuning range	~16.4 nm	~ 15 nm	0.16 – 1.05 nm
Rejection ratio	>25 dB	~ 25 dB	>25 dB
Tuning speed	< 1 sec	< 1 sec	< 1 sec
Switchable	Yes	Yes	Not applicable

Table 5.2 Performance comparison of the developed bandpass filters presented in this chapter.

To the author's knowledge, the developed bandpass filter with adjustable bandwidth is the first of its kind. It has many potential applications in the next generation of reconfigurable optical networks.

5.5 References

[1] G. P. Agrawal and S. Radic, "Phase-shifted fiber Bragg gratings and their application for wavelength demultiplexing," *IEEE Photon. Technol. Lett.*, vol. 6, pp. 995–997, 1994.

[2] L. Zhang, K. Sugden, I. Bennion and A. Molony, "Wide-stopband chirped fibre moiré grating transmission filters," *Electron. Lett.*, vol. 31, pp. 477–479, 1995.

[3] L. Wei and J. W. Y. Lit, "Phase-shifted Bragg grating filters with symmetrical structures," *IEEE J. Lightwave Technol.*, vol. 15, pp. 1405–1410, 1997.

[4] K. Sugden, L. Zhang, J. A. R. Williams, R. W. Fallon, L. A. Everall, K. E. Chisholm and I. Bennion, "Fabrication and characterization of bandpass filters based on concatenated chirped fiber gratings," *IEEE J. Lightwave Technol.*, vol. 15, pp. 1424–1432, 1997.

[5] Z. Wei, L. Qin, Q. Wang, H. Li, W. Zheng and Y. Zhang, "Fabrication of all-fiber bandpass filter using single fiber Bragg grating," *Opt. Commun.*, vol. 177, pp. 201–205, 2000.

[6] M. G. Xu, A. T. Alavie, R. Maaskant and M. M. Ohn, "Tunable fibre bandpass filter based on a linearly chirped fibre Bragg grating for wavelength demultiplexing," *Electron. Lett.*, vol. 32, pp. 1918–1919, 1996.

[7] K. Utaka, S. Akiba and Y. Matsushima, "1/4-shifted GaAsP/InP DFB lasers by simultaneous holographic exposure of negative and positive photoresists," *Electron. Lett.* vol. 20, pp. 1008–1010, 1984.

[8] R. C. Alferness, C. H. Joyner, M. D. Divino, M. J. R. Martyak and L. L. Buhl, "Narrowband grating resonator filters in InGaAsP/InP waveguides," *Appl. Phy. Lett.*, vol. 49, pp. 125–127, 1986.

[9] R. Kashyap, *Fiber Bragg gratings,* Academic Press, 1999.

[10] R. Kashyap, P. F. McKee and D. Armes, "UV written reflection grating structures in photosensitive optical fibres using phase-shifted phase masks," *Electron. Lett.*, vol. 30, pp. 1977–1978, 1994.

[11] J. Canning and M. G. Sceats, "π-phase shifted periodic distributed structures in optical fibers by UV post-processing," *Electron. Lett.*, vol. 30, pp. 1244–1245, 1994.

[12] R. Kashyap, G. D. Maxwell and B. J. Ainslie, "Laser trimmed four-port bandpass filter fabricated in singlemode planar waveguides," *IEEE Photon. Technol. Lett.*, vol. 5, pp. 191–193, 1993.

[13] M. Janos and J. Canning, "Permanent and transient resonances thermally induced in optical fibre Bragg gratings," *Electron. Lett.*, vol. 31, pp. 1007–1009, 1995.

[14] D. Uttamchandani and A. Othonos, "Phase-shifted Bragg grating formed in optical fibres by post-fabrication thermal processing," *Opt. Comm.*, vol. 127, pp. 200–204, 1996.

[15] C. J. S. de Matos, P. Torres, L.C. G. Valente, W. Margulis and R. Stubbe, "Fiber Bragg grating (FBG) characterization and shaping by local pressure," *IEEE J. Lightwave Technol.*, vol. 19, pp. 1206–1211, 2001.

[16] S. Y. Li, N. Q. Ngo, S. C. Tjin, P. Shum and J. Zhang, " Thermally tunable narrow-bandpass filter based on a linearly chirped fiber Bragg grating," *Opt. Lett.*, vol. 29, pp. 29 31, 2004.

[17] A. Othonos and K. Kalli, *Fiber Bragg gratings: fundamentals and applications in telecommunications and sensing,* Artech House, 1999.

[18] L. Wei and J. W. Y. Lit, "Phase-shifted Bragg grating filters with symmetrical structures," *IEEE J. Lightwave Technol.*, vol. 15, pp. 1405–1410, 1997.

[19] J. D. Downie and A. B. Ruffin, "Analysis of signal distortion and crosstalk penalties induced by optical filters in optical networks," *IEEE J. Lightwave Technol.*, vol. 21, pp. 1876–1886, 2003.

6 Tunable Fiber Lasers

6.1 Introduction

In recent years, tunable fiber lasers have generated great interests due to such promising applications as wavelength division multiplexing (WDM) systems, optical sensing systems, testing of optical components and laser machining. A section of a rare earth doped fiber is usually used as a gain medium in the fiber laser configuration.

Erbium-doped fiber laser (EDFL) can operate in several wavelength regions, ranging from the visible to the far infrared. The radiation in the 1.55 μm region is most attractive because it coincides with the low-loss region of silica fibers used for optical communications. The EDFLs have several advantages as described below.

- *High output power*. EDFLs have output power higher than that of semiconductor lasers.
- *Low noise*. Fiber lasers inherently have very low levels of relative intensity noise (RIN).

- *Tunability*. The tuning range of the EDFLs can be much higher than that of the semiconductor lasers.
- *Very narrow linewidth*. A linewidth of as narrow as 750 Hz has been demonstrated [1].
- *Good soliton generation*. Fiber lasers can generate good mode-locked solitons.

The lasing wavelength of a fiber ring laser can be tuned by adjusting the intra-cavity optical filter.

This chapter presents the development and testing of a tunable erbium-doped fiber ring laser (EDFRL) with ultra-narrow linewidth using a tunable phase-shifted chirped fiber Bragg grating (FBG) as a tunable intra-cavity bandpass filter. The tunable phase-shifted chirped FBG has an ultra-narrow bandwidth of < 10 pm and it can be tuned using a newly developed thermal head scanning method, which has been presented in Chapter 5. The developed laser has good stability with < 0.2 dB variation of the output power and < 0.01 nm variation of the central wavelength. The laser has an ultra-narrow linewidth of < 1.52 kHz, a tuning range of as large as ~15.5 nm, and an output power of ~10 dBm.

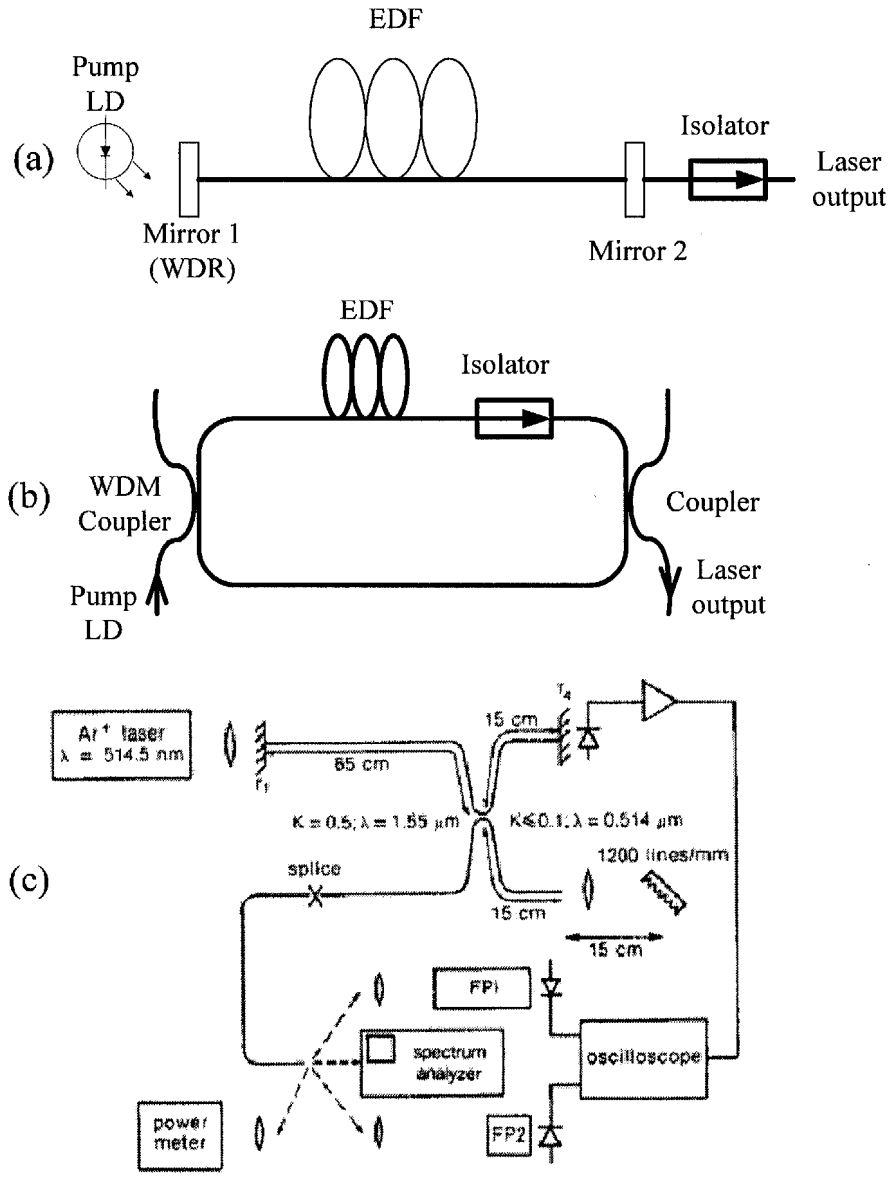

Figure 6.1 Different configurations of EDFLs, (a) A linear cavity EDFL. (b) A ring cavity EDFL. (c) A coupled cavity EDFL [7]. EDF is erbium doped fiber.

6.1.1 Summary of Fiber Lasers

Figure 6.1 shows several configurations of EDFLs, which are a linear cavity EDFL [2], a ring cavity EDFL [3], and a coupled cavity EDFL [4].

- *Linear cavity EDFL*: A linear (or Fabry-Perot) cavity is the first EDFL cavity studied by Mears *et al.* [5]. Its main advantages are its simplicity and the possibility to make short cavities. It is thus suitable for robust single-longitudinal mode operation. The schematic configuration of a linear cavity EDFL is shown in Fig. 6.1(a). In a forward-pumped linear cavity EDFL, the pump light is injected through a wavelength-dependent reflector (WDR), and the output light exits from the output mirror (mirror 2). It is preferable that the output mirror be highly reflective at the pump wavelength to recycle the unused pump power for providing optimized pumping and to prevent residual pump light from appearing at the output port.
- *Ring cavity EDFL*: The ring cavity EDFL (see Fig. 6.1(b)) has advantages, which include simplicity, high stability, and high gain efficiency. Unlike the standing-wave operation in the linear cavity EDFL, it is based on traveling-wave operation in the ring cavity, which can prevent spatial hole burning [6]. When a standing-wave pattern is established in a laser cavity, it will form a gain grating in the erbium-doped fiber. For the wave that forms this gain grating, the round-trip gain is reduced because the gain is locally saturated on the standing-wave pattern. Frequency hopping to other longitudinal modes is possible because neighboring modes may have a higher (unsaturated) gain.
- *Coupled cavity EDFL*: A typical coupled cavity EDFL is a Fox-Smith resonator laser [7] as shown in Fig. 6.1(c). A Fox-Smith resonator

consists of two coupled cavities with different cavity lengths. Strong mode selection is obtained through the Vernier effect; the only modes which oscillate are those which have the same resonance frequency in both cavities. Thus, Fox-Smith resonators are sensitive to the length ratio of the cavities, allowing long resonator and narrow linewidth.

Among these configurations, the ring cavity design is most commonly used because of its advantages over other structures as described above.

Recently, some tunable EDFRLs have been reported using, for example, tunable Fabry-Perot (F-P) filters [8], acousto-optical filters [9], Mach-Zehnder interferometers [10], coupled fiber-ring-cavity filters [11], and tunable fiber Bragg gratings (FBGs) [12]. FBGs are desirable for use as a tunable filter in the tunable EDFRLs due to their unique advantages, which include fiber compatibility, low cost, low loss and compact size.

6.1.2 Motivation

Although FBGs can be used as tunable optical filters in the development of EDFRLs, some of their inherent disadvantages will limit their application in the fiber lasers. First, the tuning range of an EDFRL using an FBG is limited by the small tuning range of FBG due to the failure feature of the silica fiber. Second, FBG, as a band reflective filter, will need to be combined with a circulator to operate as a bandpass filter in the ring cavity, and this will introduce additional loss and cost. Furthermore, the typical bandwidth of an

intra-cavity FBG is around 0.2 nm, which may not be narrow enough to achieve the ultra-narrow linewidth of EDFRLs. To obtain the ultra-narrow linewidth of the FBG-based tunable EDFRLs, an unpumped erbium-doped fiber (EDF) has been used as a saturable absorber in the cavity [1], and this will also raise the total cost of the laser.

This chapter present a new tunable EDFRL with ultra-narrow linewidth using a novel tunable phase-shifted chirped FBG as described in Chapter 5. Compared with the devices mentioned above, this tunable EDFRL has the advantages of large tuning range, ultra-narrow linewidth, low cost, and high stability.

6.1.3 Linewidth Measurement

In this section, the method used for measuring the linewidth of an unmodulated singlemode laser is discussed. Linewidth is defined in terms of the full-width half-maximum (FWHM) of the optical power spectrum. However, a normal grating-based optical spectrum analyzer (OSA) cannot offer the measurement resolution required for the measurement of small laser linewidth, which ranges from several kHz to several MHz or more. Hence, alternative methods must be used to measure the small laser linewidth.

The Fabry-Perot (F-P) interferometer technique can be used to measure the narrow linewidth, which typically ranges from 1.5 MHz to 3 GHz. By physically adjusting the cavity spacing, a bandpass peak of the F-P filter can

be scanned over a small wavelength region, which is the free spectral range (FSR) of the F-P filter, to allow precise spectral tuning [13]. An OSA based on this interferometer technique can be realized by scanning the measured spectrum range with the bandpass peak of the interferometer across the spectrum to be measured. Figure 6.2 illustrates the concept of the OSA based on the F-P interferometer technique.

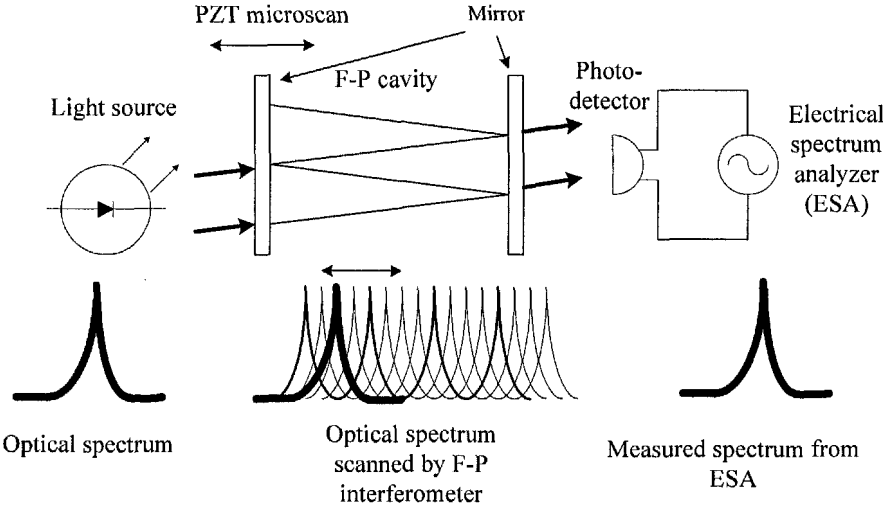

Figure 6.2 Optical spectrum analyzer based on the Fabry-Perot interferometer technique. PZT is piezoelectric actuator.

The OSA based on the F-P interferometer technique used to measure the laser linewidth was supplied by Melles Griot, and it has an FSR of 10 GHz and a finesse of 200. Hence, its measurement resolution is 50 MHz. Figure 6.3 shows the measured spectrum of an unmodulated laser using the F-P interferometer-based OSA. In Fig. 6.3, the black line is the tunable drive voltage, and the gray line is the laser spectrum with a period of 10 GHz FSR. However, the resolution of this equipment was not still adequate to allow high

accuracy measurement of the ultra-narrow characteristics of the proposed laser as presented here.

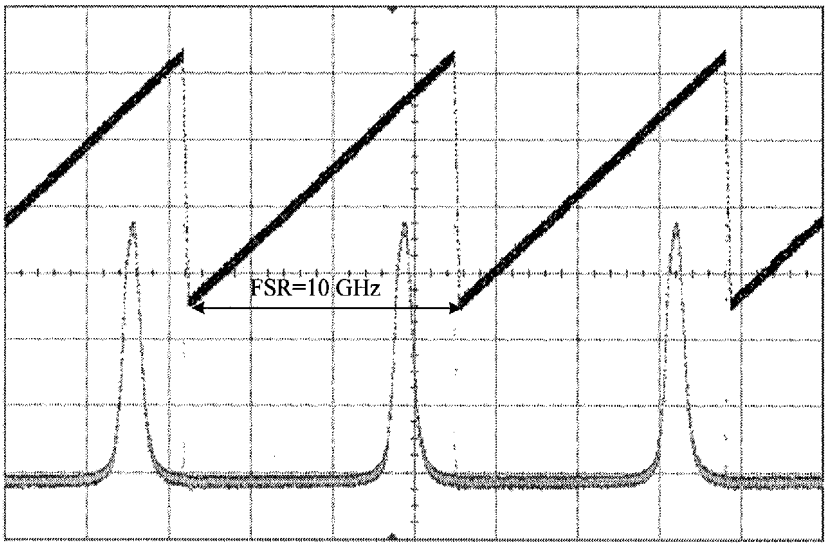

Figure 6.3 The measured spectrum using the F-P interferometer OSA based technique (gray line). The PZT drive voltage is shown as the black line.

The other methods that can be used to measure the laser linewidth include optical heterodyne method [14], delayed self-heterodyne method [15], and delayed self-homodyne method [16]. The delayed self-heterodyne method is widely used because of its simple experimental setup. Figure 6.4 shows the experimental setup used to measure the laser linewidth using the delayed self-heterodyne method. A 50:50 fiber coupler is used to equally split the incident light into two fiber arms, and the optical frequency of one arm is offset with respect to the other arm using an acousto-optic (AO) frequency shifter. If the delay of one arm exceeds the coherence time of the source, the two combining

beams interfere with each other. An electrical spectrum analyzer is used to display the beat tone, which is broadened by the laser linewidth.

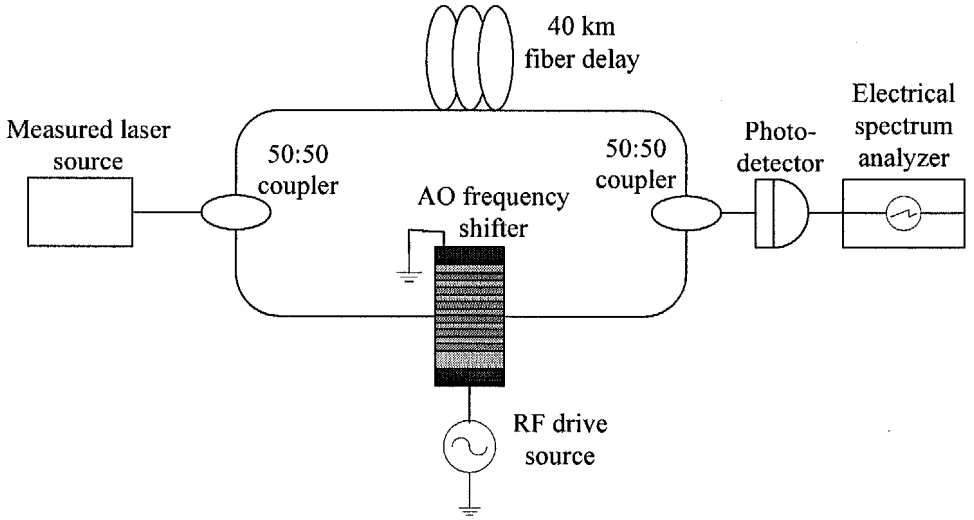

Figure 6.4 Experimental setup to measure the laser linewidth using the delayed self-heterodyne method.

6.2 Proposed Tunable Fiber Ring Laser

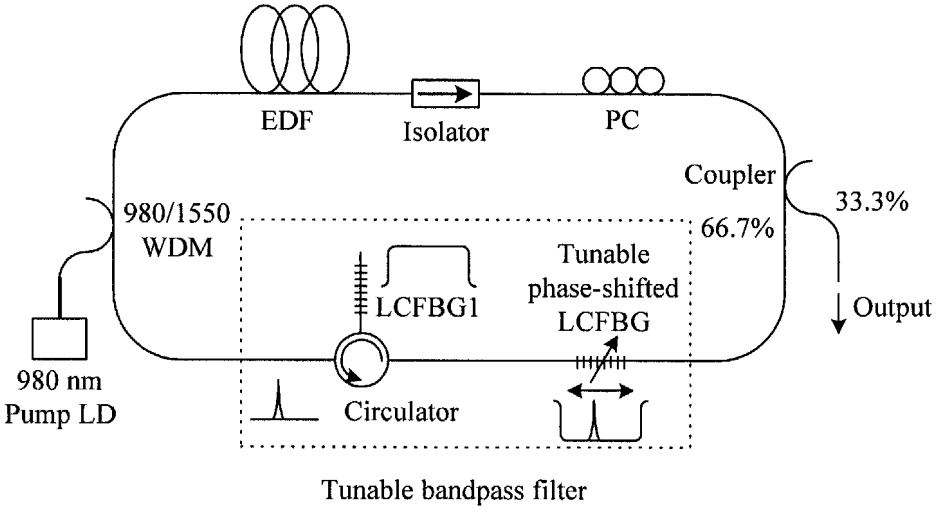

Figure 6.5 Experimental configuration of the proposed tunable fiber ring laser.

Figure 6.5 shows the schematic of a proposed tunable EDFRL. The laser consists of 25 m of erbium-doped fiber (EDF) pumped by a 980-nm laser diode (LD), a tunable phase-shifted linearly chirped FBG (LCFBG), an optical circulator, an identical LCFBG1, a 2:1 fiber coupler, a polarization controller (PC) and an isolator. The mode field diameter of the EDF is 6.6 μm and its cladding diameter is 80 μm. The identical LCFBG1 operating in the reflection mode together with the circulator is used to suppress the transmission outside the stopband of the phase-shifted LCFBG, and this will allow the suppression of the unwanted laser output outside the stopband of the phase-shifted LCFBG to achieve stable laser operation. It should be noted that the LCFBG1 and the optical circulator are needed as the stopband of the LCFBG covers the whole gain bandwidth of EDF, and this further simplifies the laser construction and reduces the cost.

The developed tunable phase-shifted LCFBG presented in Chapter 5 is used as a tunable optical bandpass filter (TOBF) in the laser cavity. The length of the LCFBG is 6 cm and the chirp rate is 2.25 nm/cm. The stopband of the LCFBG is ~21 nm (i.e. from 1544 to 1565 nm). The LCFBG was inscribed into a hydrogen-loaded germanium-doped cladding-mode suppression fiber using the UV scanning beam technique. The cladding-mode loss, which can introduce an undesirable loss on the short wavelength side of the LCFBG (see Section 5.3.2 in Chapter 5) can be eliminated by using this cladding-mode suppressed fiber.

A resistance wire is used as a thermal element to heat a small contact point of LCFBG. Two heat sinks are used to eliminate the unwanted heat distribution on both sides of the resistance wire. When DC current is applied to the resistance wire, a thermally-induced temporary phase shift is introduced into the LCFBG, and hence a narrow passband peak is created within the stopband of the LCFBG. When the wire heater is scanned along the LCFBG, which is controlled by a linear travel stage, the center wavelength of the narrow passband peak shifts according to the position of the resistance wire. As a result, an all-fiber tunable optical bandpass filter (TOBF) can be developed.

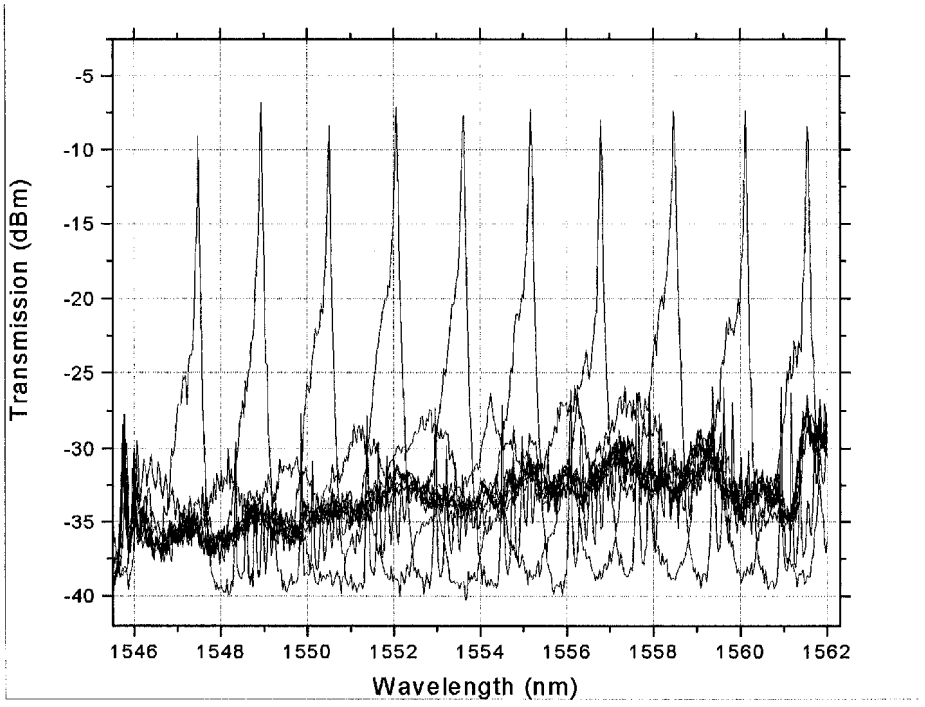

Figure 6.6 Measured transmission spectrum of TOBF (with LCFBG1 and the circulator) over the tuning range.

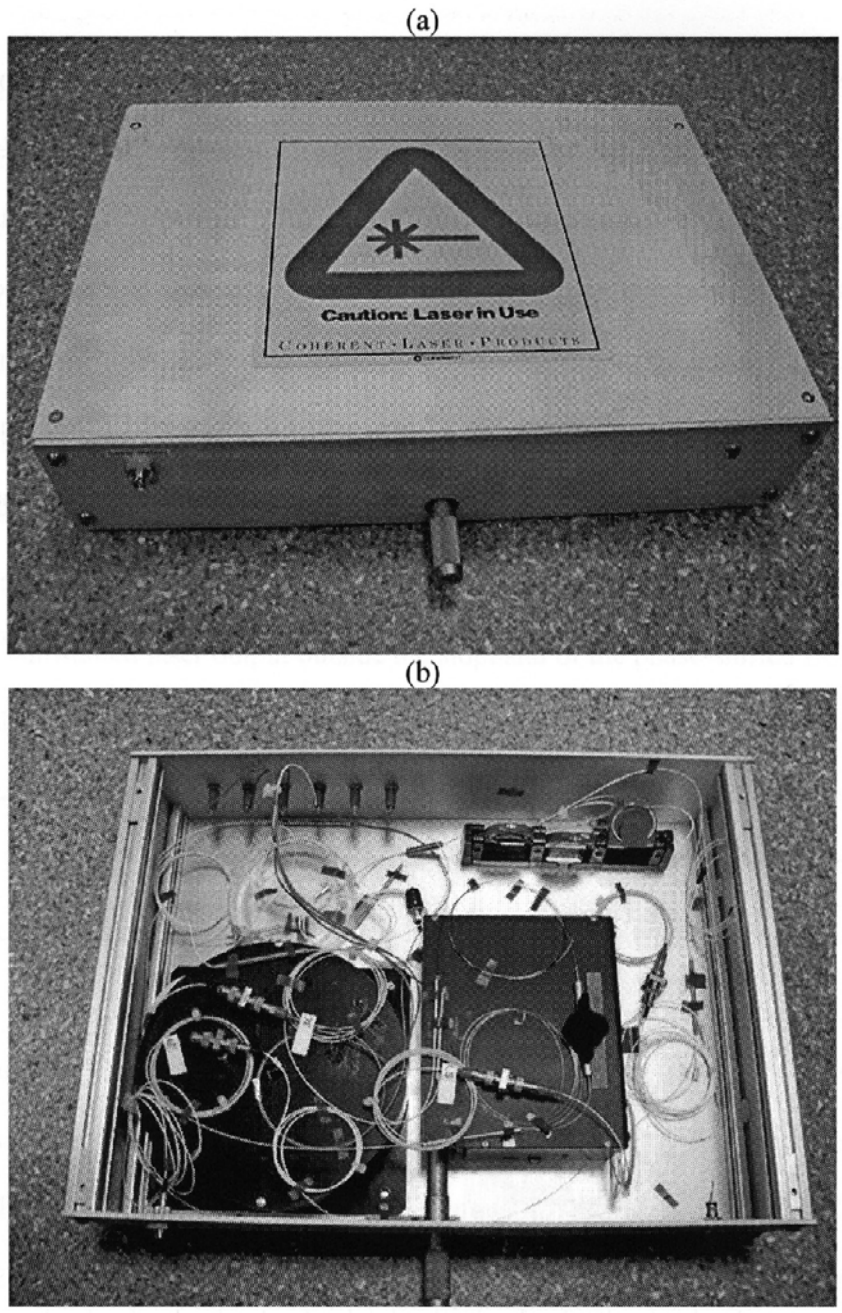

Figure 6.7 The outside (a) and inside (b) view of the packaged tunable laser.

The measured transmission spectrum of the TOBF (with LCFBG1 and the circulator) is shown in Fig. 6.6. The 3-dB bandwidth of the TOBF was measured to be smaller than 0.01 nm, which is only limited by the resolution

of the OSA used, and it is much smaller than the bandwidth of a typical FBG. Hence, this type of TOBF is very suitable for use in high-performance fiber lasers with narrow linewidth and single-mode operation. In this experiment, the total insertion loss of TOBF is ~8 dB, and which can be improved by optimizing the temperature and diameter of the heating wire used to achieve $\lambda/4$ phase shift. About 4 dB of the insertion loss is caused by the additional use of the LCFBG1 and the circulator. Figure 6.7 is a photograph of a packaged tunable laser source with ultra-narrow linewidth.

6.3 Laser Performance and Testing

When scanning the thermal head along the LCFBG of over 50 mm, the lasing wavelength can be tuned from 1546.8 nm to 1562.3 nm giving a tuning range of 15.5 nm. It was observed that there was no spectral distortion on the lasing output over the whole tuning range and that the output power was relatively constant with a power variation of < 1 dB over the full range. There was no additional gain flattening filter used in the laser cavity. Figure 6.8 shows the measured laser spectrum over the tuning range and Figure 6.9 shows the variation of the output power when the laser was tuned over the whole tuning range. The side-mode suppression ratio is greater than 30 dB. When the pump power was ~98 mW, the laser output was ~10 mW. Figure 6.10 shows the laser output power at 1556 nm versus the pump power. The slope efficiency is ~9.4 %.

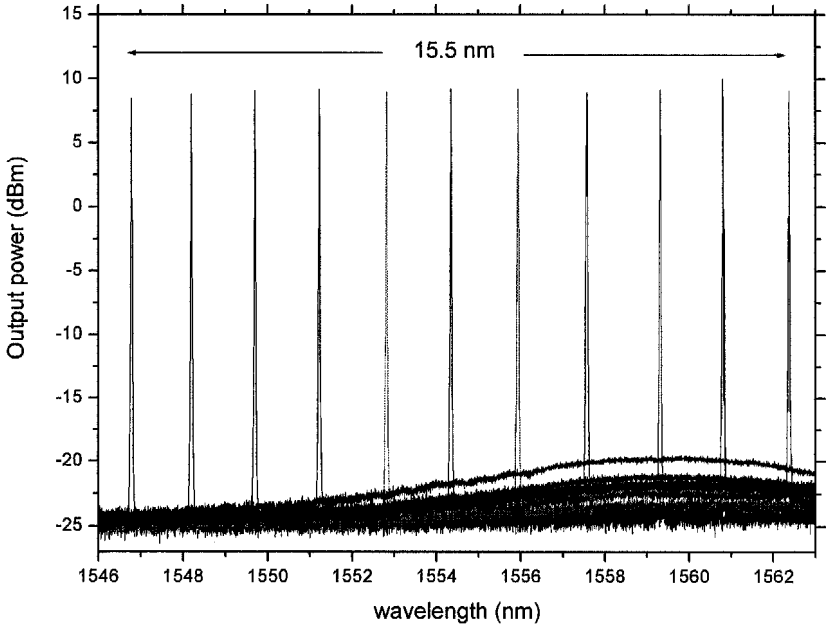

Figure 6.8 Measured laser output spectrum over the tuning range.

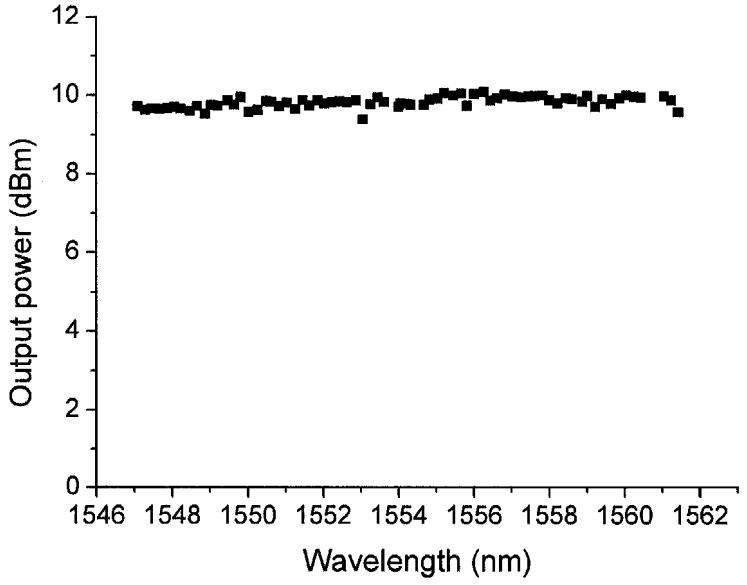

Figure 6.9 Variation of the laser output power when the laser was tuned over the whole tuning range.

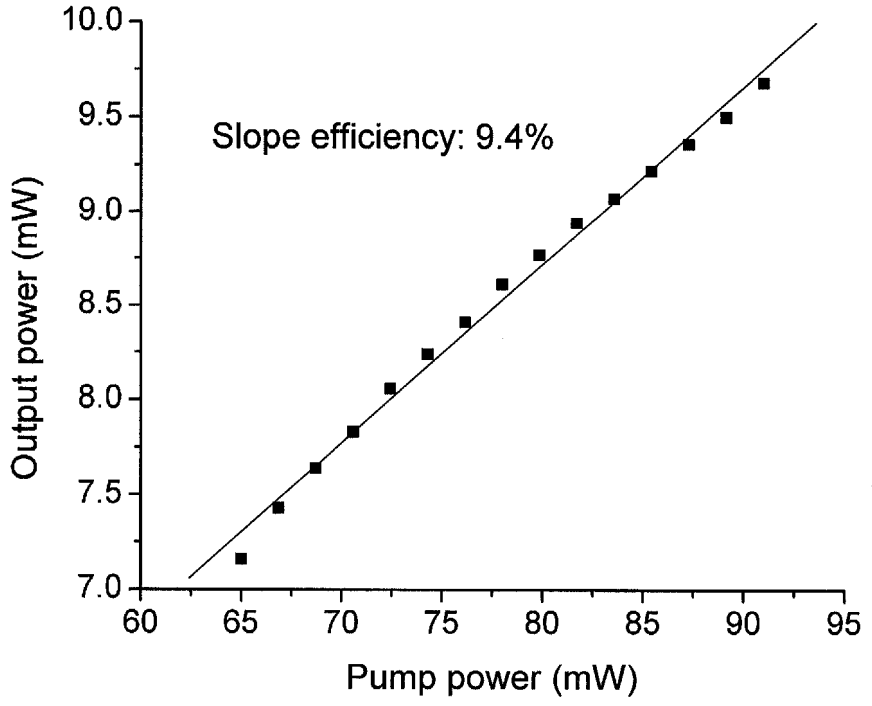

Figure 6.10 Laser output power versus the pump power at 1556 nm.

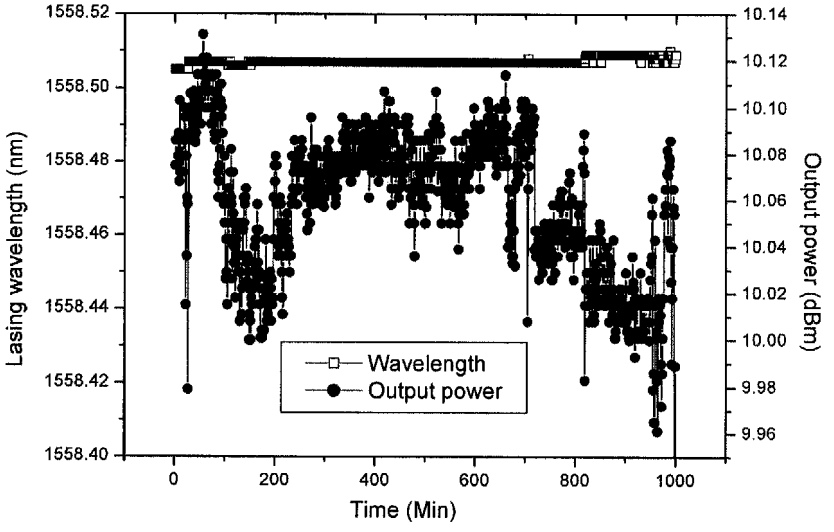

Figure 6.11 Stability of the laser output power and the lasing wavelength.

Figure 6.11 shows the stability of the output power and the lasing wavelength at 1556 nm. The laser stability was tested in the laboratory environment, and no further equipment was used to stabilize the temperature. Over a period of 1000 minutes, the laser output power only varies by about 0.2 dB and the lasing wavelength variation is smaller than 0.01 nm, which is the limitation caused by the resolution of the OSA. These findings show good power stability and good wavelength precision of the developed EDFRL. Furthermore, the laser spectral shape remains almost unchanged with time as shown in Fig. 6.12.

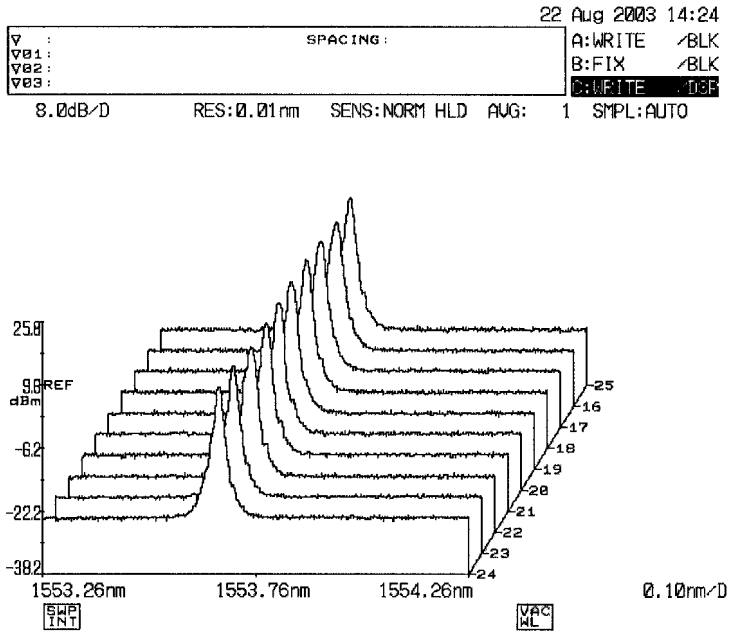

Figure 6.12 Laser spectral shape is almost constant with time. Each measurement was taken at a 2-minute interval.

The laser linewidth was measured using the delayed self-heterodyne interferometer technique with 40 km fiber delay and with a carrier frequency of the acousto-optic frequency shifter of 55 MHz [15]. Figure 6.13 shows the beat signal obtained from an electrical spectrum analyzer. Due to the slow integration time of the electronic spectrum analyzer, the effect of frequency jitter on the measured laser linewidth needs to be taken into account. Frequency jitter is the random change in the operating frequency of the laser with time, which is probably caused by environment temperature fluctuation. The measured linewidth could be ten times greater when the measurement averaging time takes several seconds. The effect of the frequency jitter on the linewidth measurement can be minimized by measuring the beat signal at the –20 dB point from its maximum. The relationship between the beat signal linewidth Δf_b measured at the –20 dB level and the laser linewidth $\Delta\upsilon$ is given by $\Delta f_b = 2\sqrt{99}\Delta\upsilon$ [17]. From Fig. 6.13, it can be estimated that the laser linewidth is less than 1.52 kHz.

The resolution of the travel stage used to control the resistance wire is 0.01 mm, which corresponds to a tuning step of 3 pm of the laser (see Fig. 5.13). The tuning step can be made smaller using a travel stage with higher resolution and/or LCFBG with longer length and smaller chirp rate. It should be noted that the tunable range of the fiber ring laser is only limited by the stopband width of the LCFBG. Using LCFBG with longer length and/or larger chirp rate, the laser tuning range can be increased to cover the whole C-band

and even C+L band. This fiber ring laser can also operate in the S-band and L-band using LCFBG with a prescribed stopband in the design.

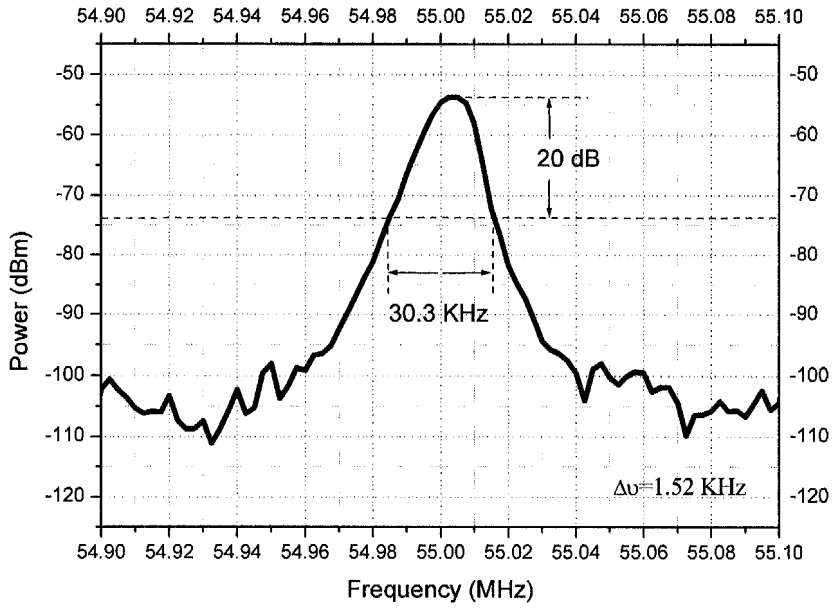

Figure 6.13 Measured output power spectrum with a linewidth of less than 1.52 KHz using a delayed self-heterodyne technique (with 40 km delay on one arm, see Fig. 6.4).

6.4 Summary

A novel tunable EDFRL has been presented. The tunability of the EDFRL is achieved by tuning a phase-shifted LCFBG with very narrow passband (< 10 pm). The measured linewidth of the laser is ~1.52 kHz. The output power of the laser is ~10 dBm with a pump power of 98 mW. The tuning step is 3 pm corresponding to the resolution of the travel stage used to control the tunable phase-shifted LCFBG. The laser tuning range is 15.5 nm. It should be noted

that the tuning range of the EDFRL could be easily extended to 100 nm using a tunable phase-shifted chirped FBG with larger chirp rate and longer length. The output power variation is smaller than 1 dB within the whole tuning range. The tuning range could be increased using LCFBG with wider rejection bandwidth. The circulator and the LCFBG1 in the lasing cavity would not be needed when the stopband of the LCFBG could cover the whole gain bandwidth of the EDF. The developed laser has good stability with variation of output power of < 0.2 dB and variation of lasing wavelength of < 0.01 nm over a continuous testing period of 1000 minutes. Using the proposed method, tunable fiber ring lasers for S-band or L-band operation can be developed using a similar laser architecture as that presented here.

6.5 References

[1] Y. W. Song, S. A. Havstad, D. Starodubov, Y. Xie, A. E. Willner and J. Feinberg, "40-nm-wide tunable fiber ring laser with single-mode operation using a highly stretchable FBG," *IEEE Photon. Technol. Lett.*, vol. 13, pp. 1167–1169, 2001.

[2] S. H. Chang, I. K. Hwang, B. Y. Kim and H. G. Park, "Widely tunable single-frequency Er-doped fiber laser with long linear cavity," *IEEE Photon. Technol. Lett.*, vol. 13, pp. 287–289, 2001.

[3] H. Chen, F. Babin, M. Leblanc, and G.W. Schinn, "Widely tunable single-frequency erbium-doped fiber lasers," *IEEE Photon. Technol. Lett.*, vol. 15, pp. 185–187, 2003.

[4] P. K. Cheo, L. Wang and M. Ding, "Low-threshold, self-tuned and passively mode-locked coupled-cavity all-fiber lasers," *IEEE Photon. Technol. Lett.*, vol. 8, pp. 66–68, 1996.

[5] R. J. Mears, L. Reekie, S. B. Poole and D. N. Payne, "Low-threshold, tunable cw and Q-switched fiber laser operating at 1.55 μm," *Electron. Lett.*, vol. 22,.no. 3, pp. 159–160, 1986.

[6] N. K. Park, J. W. Dawson and K. J. Vahala, "All fiber, low threshold, widely tunable single frequency, erbium-doped fiber ring laser with a tandem fiber Fabry-Perot filter," *Appl. Phys. Lett.*, vol. 59, pp. 2369–2371, 1991.

[7] P. Barnsley, P. Urquhart, C. Millar and M. Brierley, "Fiber Fox-Smith resonators: application to single-longitudinal-mode operation of fiber lasers," *Journal of the Optical Society of American A,* vol. 5, pp. 1339–1346. 1988.

[8] J. L. Zyskind, J. W. Sulhoff, J. Stone, D. J. Digiovanni, L. W. Stulz, H. M. Presby, A. Piccirilli and P. E. Pramayon, "Electrically tunable diode-pumped erbium-doped fiber ring laser with fiber Fabry–Perot etalon," *Electron. Lett.*, vol. 27, no. 21, pp. 1950–1951,1991.

[9] S. H. Yun, D. J. Richardson, D. O. Culverhouse and B. Y. Kim, "Wavelength-swept fiber laser with frequency shifted feedback and resonantly swept intra-cavity acoustooptic tunable filter," *IEEE Journal of Selected Topics in Quantum Electron.*, vol. 3 , pp. 1087–1096, 1997.

[10] Y. T. Chieng and R. A. Minasian, "Tunable erbium-doped fiber laser with a reflection Mach-Zehnder interferometer," *IEEE Photon. Technol. Lett.*, vol. 6, pp. 153 153, 1994.

[11] S. K. Kim. G. Stewart and B. Culshaw, "Mode-hop-free single-longitudinal-mode erbium-doped fiber laser frequency scanned with a fiber ring resonator," *Appl. Opt.*, vol. 38, pp. 5154 5157, 1999.

[12] S. Li and T. Chan, "Electrical wavelength-tunable actively mode-locked fiber ring laser with a linearly chirped fiber Bragg grating," *IEEE Photon. Technol. Lett.*, vol. 10, pp. 799 801, 1998.

[13] J. Stone and D. Marcuse, "Ultrahigh finesse fiber Fabry-Perot interferometers," *IEEE J. Lightwave Technol.*, vol. 4, pp. 382 385, 1986.

[14] G. R. Olbright, R. P. Bryan, W. S. Fu, R. Apte and D. M. Bloom, "Heterodyne measurement of linewidth, tunability, and frequency synthesis of vertical-cavity surface-emitting laser diode arrays," *IEEE Trans. Electron Devices*, vol. 38, pp. 2698 2699, 1991.

[15] L. E. Richter, H. I. Mandelberg, M. S. Kruger and P. A. McGrath, "Linewidth determination from self-heterodyne measurements with subcoherence delay times," *IEEE J. Quantum Electron.* vol. 22, pp. 2070 – 2074, 1986.

[16] K. Iiyama, K. Hayashi, Y. Ida, S. Tabata and Y. Sakai, "Delayed self-homodyne method using solitary monomode fibre for laser linewidth measurements," *Electron. Lett.*, vol. 25, pp. 1589 1590, 1989.

[17] Pramod K. Rastogi, *Optical Measurement Techniques and Applications*, Artech House, 1997.

7 Conclusions and Recommendations for Future Works

7.1 Conclusions

This thesis has presented the investigation of tunable optical filters (TOFs) based on different technologies, which are all-fiber acousto-optical technique, fiber Bragg gratings (FBGs), and phase-shifted FBGs. Several tuning methods and mechanisms of TOFs have been proposed. To demonstrate the effectiveness of the proposed tuning methods, several types of TOFs for various applications have been developed and tested and they are listed below.

- An electrically tunable dispersion compensating filter,
- A widely tunable narrow bandpass filter,
- A widely tunable broad bandpass filter,
- An optical bandpass filter with adjustable bandwidth,
- An all-fiber acousto-optical tunable filter.

Furthermore, the newly developed tunable narrow bandpass filter has been applied to the development of:

- A tunable erbium-doped fiber ring laser.

In Chapter 2, the basic theory and characteristics of FBGs have been presented, and the existing technologies of TOFs have been briefly discussed and compared.

In Chapter 3, a novel tunable dispersion-compensating filter based on a uniform FBG has been developed and implemented. This tunable dispersion compensator with almost-fixed center wavelength was based on the electrical adjustment of the chirp of a uniform FBG by applying and controlling the temperature gradient and strain gradient of the FBG. To the author's knowledge, this is the first method that combines the temperature gradient and strain gradient as a dispersion tuning technique. Applying an electrical power of less than 0.68 W, it has been shown that the dispersion of a linearly chirped FBG can be continuously adjusted from –178 ps/nm to –302 ps/nm with a central wavelength shift of as small as 0.173 nm. This integrated device has many advantages, which include compact size, electrical tunability, almost fixed central wavelength, low insertion loss, simple controllability, and power efficiency.

In Chapter 4, the successful development of an all-fiber acousto-optic tunable filter (AOTF) has been described. In a fiber with diameter (core and cladding) of 125 μm and interaction length of 60 cm, a notch filter with a maximum isolation ratio of ~22 dB and tuning range of 90 nm was developed. Generally, it was shown experimentally that the isolation ratio of an all-fiber acousto-optic notch filter increases with an increase in the interaction length and with a

reduction in the fiber diameter. The all-fiber AOTF has advantages, which include low insertion loss, large tuning range, high tuning speed, and all-fiber geometry.

In Chapter 5, several types of tunable optical bandpass filters (TOBFs) with different characteristics for various potential applications have been developed based on the concept of temporary phase shift in the linearly chirped FBG (LCFBG). The developed narrowband TOBF has a narrow bandwidth of < 10 pm, a tuning range of 16.5 nm, a minimum insertion loss of ~2 dB and a rejection ratio of > 25 dB. This narrowband TOBF has some advantages including continuous tuning, simple construction, easy control technique, low cost, narrow bandwidth, low polarization sensitivity and large tuning range. This narrowband TOBF has been applied to develop a tunable fiber ring laser as shown in Chapter 6. The developed broadband TOBF has a broad bandwidth of ~0.2 nm, a tuning range of ~15 nm, a minimum insertion loss of ~4 dB and a maximum rejection ratio of ~25 dB. This broadband TOBF can be potentially used in the WDM systems to select and manipulate a particular wavelength channel. Both the narrowband and broadband TOBFs have several unique features. First, the proposed tuning technique can overcome the limited tuning range of the conventional FBGs (e.g. using strain) due to the physical failure feature of the silica fiber. It should be noted that the tuning range of the TOBF, which depends on its stopband window, could be easily extended to 100 nm or more by using a LCFBG with a larger chirp rate and/or longer length. Second, unlike the normal FBGs that operate in reflection mode, these

TOBFs operate in transmission mode, which means that no circulator (resulting in lower loss and lower cost) is required in these TOBFs. Third, the passband peak could also be switched off by removing the DC power from the resistance wires. Finally, attenuation of the passband peaks of these filters can be adjusted by changing the voltage of the applied DC power. A novel optical bandpass filter with adjustable bandwidth has been developed, and its bandwidth can be tuned from ~0.16 nm to ~1.05 nm. To the author's knowledge, this is the first proposal to improve and adjust the bandwidth of a phase-shifted fiber Bragg grating after fabrication.

In Chapter 6, a novel tunable erbium-doped fiber ring laser (EDFRL) has been presented. The tunability of this EDFRL has been achieved by tuning a phase-shifted LCFBG with very narrow passband (< 10 pm). The output power of the laser is ~10 dBm with a pump power of 98 mW. The tuning step is 3 pm, which corresponds to the resolution of the stage used to control the tunable phase-shifted LCFBG. The laser tuning range is 15.5 nm. The output power variation is smaller than 1 dB within the whole tuning range. The tuning range could be increased using a LCFBG with wider rejection bandwidth (or stopband). The circulator and the LCFBG1 in the cavity would not be needed when the stopband of the LCFBG could cover the whole gain bandwidth of the erbium-doped fiber (EDF). Using the proposed method, tunable fiber ring lasers for S-band or L-band (i.e. using a suitable LCFBG with stopband covering the S-band or L-band) operations can be developed using a similar laser architecture as that proposed here.

7.2 Recommendations for Future Work

7.2.1 Tunable Dispersion Compensating Filter

In Chapter 3, a novel method to tune the dispersion while fixing the center wavelength of a uniform FBG has been proposed. The proposed tunable dispersion compensator can be used to compensate for the fiber chromatic dispersion experienced by a single wavelength channel.

However, the proposed technique could also be applied to multi-channel dispersion compensation by using a superstructure FBG. For multi-channel dispersion compensation, keeping the center wavelength fixed is much more important because the tolerance of the center wavelength shift must be much smaller than that for a single-channel dispersion compensation [1].

It should be noted that with a proper design of the diameter profile of the uniform FBG and the thickness profile of the thin-film coating, this device could also be applied to higher-order dispersion compensation (such as dispersion slope compensation), which is an important issue in high-bit rate transmission systems [2].

7.2.2 Tunable Bandpass Filter

A new method for the development of tunable optical bandpass filters (TOBFs) based on single linearly chirped FBG (LCFBG) has been presented in Chapter 5. For concern about the robustness of this kind of TOBF, a long term stability/aging test could be necessary in the future study. Using the currently available phase mask, a tuning range of only ~16 nm of the TOBF was achieved. However, using a phase mask with longer length and/or larger chirp rate, a TOBF with larger tuning range can be developed. The tuning range of the TOBF can be as large as 100 nm using an appropriate phase mask. Furthermore, by using multiple thermal heads in the configuration, a tunable comb filter could be achieved with tunable central wavelength and adjustable wavelength spacing. Moreover, using a pair of movable thermal heads with adjustable distance, the bandpass filter with independently tunable central wavelength and adjustable bandwidth could be achieved. Furthermore, by precisely controlling the DC voltage to the resistance wire, the attenuation of the bandpass peaks can be adjusted.

7.3 References

[18] J.-X. Cai, K.-M. Feng, A. E. Willner, V. Grubsky, D.S. Starodubov and J. Feinberg, "Simultaneous tunable dispersion compensation of many WDM channels using a sampled nonlinearly chirped fiber Bragg grating," *IEEE Photon. Technol. Lett.*, vol. 11, pp. 1455–1457, 1999.

[19] Y. W. Song, S. M. R. M. Nezam, D. Starodubov, J. E. Rothenberg, Z. Pan, H. Li, R. Wilcox, J. Popelek, R. Caldwell, V. Grubsky and A. E. Willner, "Tunable interchannel broad-band dispersion-slope compensation for 10-Gb/s WDM systems using a nonchannelized third-order chirped FBG," *IEEE Photon. Technol. Lett.*, vol. 15, pp. 144–146, 2003.

Appendix A

AUTHOR'S PUBLICATIONS

Patents

- ✓ N. Q. Ngo, **S. Y. Li**, "Ultra-narrow Linewidth Tunable Fiber Laser Using a Tunable Phase-shifted Chirped FBG". US patent under filing.
- ✓ S. C. Tjin, N. Q. Ngo, **S. Y. Li** and K. M. Tan, "Portable wavelength meter using acousto-optic tunable filter", patent application in progress.

Publications

These publications result from the work of this thesis.

Journal papers

- **S. Y. Li**, N. Q. Ngo, S. C. Tjin and Le Nguyen Binh, "Tunable and switchable optical bandpass filters using a single linearly chirped fiber Bragg grating," *Optics Communications*, vol. no. 239, pp. 339 344, 2004.
- **S. Y. Li**, N. Q. Ngo, S. C. Tjin, P. Shum and J. Zhang, "Thermally tunable narrow-bandpass filter based on a linearly chirped fiber Bragg grating," *Optics Letters*, vol. 29, no. 1, pp. 29 31, 2004.
- N. Q. Ngo, **S. Y. Li**, R. T. Zheng, S. C. Tjin, and P. Shum, "Electrically tunable dispersion compensator with fixed center wavelength using fiber Bragg grating," *IEEE Journal of Lightwave Technology*, vol. 21, no. 6, pp. 1568 1575, 2003.
- N. Q. Ngo, **S. Y. Li**, Le Nguyen Binh and S. C. Tjin, "A phase-shifted linearly chirped fiber Bragg grating with tunable bandwidth," *Optics Communications,* in press.
- **S. Y. Li** and N. Q. Ngo, "Tunable fiber laser with narrow-linewidth and single-mode operation using a tunable phase-shifted chirped FBG," *IEEE Photonics Technology Letters*, to be submitted.

- **S. Y. Li**, N. Q. Ngo and S. C. Tjin, "Adjustable transmission spectrum of chirped FBG based on thermal head scanning method," *IEEE Journal of Lightwave Technology*, to be submitted.

Conference papers

- **S. Y. Li**, N. Q. Ngo, S. C. Tjin, P. Shum and J. Zhang, "Tunable and switchable optical bandpass filters based on phase-shifted linear chirped fiber Bragg gratings," CLEO/Pacific Rim 2003, 15-19 Dec. 2003, Taipei, R. O. China, pp. 205.
- **S. Y. Li**, N. Q. Ngo, S. C Tjin, and P. Shum, "Phase-Shifted Linearly Chirped Fiber Bragg Gratings with Adjustable Transmission Characteristics," The 16th Annual Meeting of the IEEE Lasers and Electro-Optics Society (LEOS 2003), 26 30 Oct. 2003, Tucson, USA, pp. 975 976.
- **S. Y. Li**, N. Q. Ngo, S. C. Tjin, P. Shum, J. Zhang, and J. X. Huang, "Development of tunable optical filter with switchable passband using linearly chirped fiber Bragg grating," Conference on the Optical Internet/ Australian Conference on Optical Fiber Technology (COIN & ACOFT 2003), pp. 711 713, 2003.
- **S. Y. Li**, N. Q. Ngo, R. T. Zheng, S. R. Natarajan, S. C. Tjin, and P. Shum, "Electrically tunable dispersion compensator based on fiber Bragg grating without central wavelength shift," Proceedings of IEEE, 1st International Conference on Optical Communications and Networks (ICOCN 2002), 11-14 November, 2002, Singapore, pp. 38 41.

<u>These publications result from collaborative works with other members in NTU.</u>

Journal papers

- J. Zhang, P. Shum, X. P. Cheng, N. Q. Ngo and **S. Y. Li**, "Analysis of linearly tapered fiber Bragg grating for dispersion slope compensation,"

IEEE Photonics Technology Letters, vol. 15, no. 10, pp. 1389 1391, 2003.

- J. Zhang, P. Shum, **S. Y. Li**, N. Q. Ngo, X. P. Cheng and J. H. Ng "Design and fabrication of flat-band long period grating," *IEEE Photonics Technology Letters*, vol. 15, no. 11, pp. 1558 1560, 2003.
- N. Q. Ngo, D. Liu, X. Y. Dong, L. N. Binh, **S. Y. Li** and S. C. Tjin , "A spacing tunable multiwavelength fiber laser source using a Sagnac loop filter", *Optical Engineering*, in press.
- N. Q. Ngo , R. T. Zheng , S. C. Tjin , **S. Y. Li**, "Tabu Search synthesis of cascaded Fiber Bragg Gratings for linear phase filters", *Optics Communications*, in press.

Conference papers

- R. Zheng, N. Q. Ngo, P. Shum, **S. Y. Li**, and S. C. Tjin, "*Tabu search algorithm for the optimization of fiber Bragg gratings*," Asia-Pacific Optical and Wireless Communications (APOC), 14-18 October 2002, Shanghai, China.